Enhanced Direction of Arrival Estimation through Electromagnetic Modeling

By

Brian Cordill

Submitted to the Department of Electrical Engineering & Computer Science and the
Graduate Faculty of the University of Kansas
in partial fulfillment of the requirements for the degree of
Doctor of Philosophy in Electrical Engineering

Committee members

Sarah Seguin, Chairperson

Shannon Blunt

Christopher Allen

James Stiles

Mark Ewing

Eric Mokole

Date defended:

The Dissertation Committee for Brian Cordill certifies
that this is the approved version of the following dissertation :

Enhanced Direction of Arrival Estimation through Electromagnetic Modeling

Sarah Seguin, Chairperson

Date approved: _____

Abstract

Engineering is a high art that balances modeling the physical world and designing meaningful solutions based on those models. Array signal processing is no exception, and many innovative and creative solutions have come from the field of array processing. However, many of the innovative algorithms that permeate the field are based on a very simple signal model of an array. This simple, although powerful, model is at times a pale reflection of the complexities inherent in the physical world, and this model mismatch opens the door to the performance degradation of any solution for which the model underpins. This dissertation seeks to explore the impact of model mismatch upon common array processing algorithms. To that end, this dissertation brings together the disparate topics of electromagnetics and signal processing. Electromagnetics brings a singular focus on the physical interactions of electromagnetic waves and physical array structures, while signal processing brings modern computational power to solve difficult problems. We delve into model mismatch in two ways; first, by developing a blind array calibration routine that estimates model mismatch and incorporates that knowledge into the reiterative superresoluiton (RISR) direction of arrival estimation algorithm; second, by examining model mismatch between a transmitting and receiving array, and assessing the impact of this mismatch on prolific direction of arrival estimation algorithms. In both of these studies we show that engineers have traded algorithm performance for model simplicity, and that if we are willing to deal with the added complexity we can recapture that lost performance.

Acknowledgements

Although my name alone appears as author, works such as this are made possible only by the support of many. Throughout these pages you will find references to the works of many fellow engineers and scholars. And it is upon the foundation of these great works that I add my own meager contribution. To quote Sir Isaac Newton, "If I have seen further it is by standing on the shoulders of giants."

I would like to thank my advisor, Dr. Sarah Seguin, for her support and guidance. She has pushed me to be a better student, a better researcher and a better engineer than I though myself capable. She balanced directing my research to keep me on track, while giving me the freedom to explore my ideas and bring my perspective to the many projects we worked together.

I would also like to express my gratitude to my parents. I would not be the person I am today without your love and support.

And last to my wife Sarah, your love and support through this endeavor has been unwavering. You have put much of your life and career on hold to put up with my many long days and late nights. You may not of understood all that I did, but you understood that it was important to me, and that I needed to see it through.

Contents

List of Figures

Chapter 1

Introduction

Modern microwave systems are remarkably capable, and much of that capability comes from innovation in array processing. But this innovation is precariously underpinned by a simplified model of reality that at times poorly reflects the world in which a real system must operate. This body of work explores the models upon which many processing algorithms are built and seeks to quantify the impacts when these models fail to adequately describe the intricacies of the real world. This work develops a unique enhancement for the RISR algorithm that estimates model mismatch and reincorporates this knowledge into RISR to improve performance. It also brings fresh perspective to the area of array mutual coupling by considering the effect microwave hardware has on mutual coupling and explores how this can perturb the common array model. We will show that the impacts of model mismatch are wide ranging and the principals explored in this work are relevant to any application that involves an array of antennas. We start in Section 1.1 by surveying the impact of model mismatch in array processing before focusing in on Direction of Arrival (DoA) estimators, in Section 1.2. Section 1.3 brings together model mismatch and DoA estimation and presents a high level explanation of the methodology used in this dissertation. Finally, Section 1.4 outlines this body of work and provides a quick reference to each chapter.

1.1 Model Mismatch

An array processing algorithm is only as good as its underlying model. As we will see many array processing methods are based on idealized array models and are adversely impacted when this idealized model fails to materialize in real systems. Once a system is implemented it is subject to a number of forces that cause the true array response to deviate from the ideal array response. This includes, but is not limited to, factors such as channel gain/phase mismatch, mutual coupling and sensor placement uncertainty. Other effects such as manufacturing tolerances in producing the individual array elements and even environmental factors can also play a role in perturbing the true array manifold. In this section we examine common array processing algorithms and their response to model mismatch. We will specifically look at beamforming, direction of arrival estimation, as well as, take a closer look at some of these perturbing factors and the array calibration processes that attempt to quantify and remove these effects.

One of the most fundamental roles array processing plays is to produce a desired radiation pattern directed in a particular direction, commonly refereed to as beamforming. Beamforming can be accomplished by viewing an array as a sampling of a continuous aperture distribution either in a classical sense with a prescribed pattern[1, Chap. 3] or in an adaptive sense where the pattern is modified based on the signal environment [1, Chap. 6]. In either sense, the efficacy of beamforming is generally evaluated by the ability of the beamformer to produce a desired pattern, accurately place nulls, and cancel interference. The performance of a beamformer, either classical or adaptive, is going to be degraded if the model of the array's performance does not match its true performance. The impact of model mismatch has been studied in circular arrays [2], often within the context of cellular base stations [3, 4], as well as for linear arrays [5, 6]. In addition to studying the impact of model mismatch, a number of works have strived to compensate for mismatch. Many methods first seek to quantify the model mismatch before using this information to improve beamforming [7, 8]. Some have attempted to create model mismatch robust beamformers that leverage the

regular structure inherent to mutual coupling [9, 10], while others have worked on optimal beamforming once the mutual coupling is known[11]. As fundamental as beamforming is, it is not the only facet of array processing that is impacted by model mismatch.

Direction of arrival estimation is another predominant area within array processing. In general, direction of arrival estimation algorithms attempt to ascertain the number and angle of incidence of a set of spatially diverse signals. There are a number of existing DoA estimation techniques. Following directly from beamforming, a common method known as beamscanning uses beamforming techniques to scan a desired range of spatial angles [1, p. 1140–1155]. Eigen-methods such as MUSIC and ESPRIT leverage the eigen-structure of a Sample Covariance Matrix (SCM) to produce a DoA estimate [1, p.1155–1189]. More recent work makes use of a recursive minimum mean-squared error framework to estimate the DoA [12, 13]. Classic beamformers are susceptible to model mismatch [1, p.66–70] as are many adaptive beamformers [14]. While the options to mitigate model mismatch are limited for classic beamformers, adaptive beamformers such as the Minimum Variance Distortionless Response (MVDR) beamformer commonly search over a constrained array performance curve to minimize the received signal variance [15, 16, 17]. Eigen-methods that require explicit knowledge of the array model, such as MUSIC, are greatly impacted when the true array response deviates from the assumed model [18, 19]. To overcome this sensitivity to model mismatch some works attempt to estimate the model mismatch [20, 21]. Eigen-methods that do not require explicit knowledge of the array model, such as ESPRIT, are also impacted by model mismatch if the mismatch undermines their underlying assumptions [22]. Like the MUSIC-based methods, compensation for model mismatch for ESPRIT often involves modeling and quantifying the mismatch [23, 24]. The Reiterative Superresolution (RISR) algorithm was designed to be robust to model mismatch and explicitly attempts to leverage model uncertainty within the algorithm [13, p. 336]. Clearly, model mismatch can degrade the performance of many direction of arrival estimation algorithms, and much research has been devoted to designing algorithms that estimate, compensate or otherwise be made robust

to the effects of model mismatch.

The last array processing category we will examine is array calibration. Unlike beamforming and direction of arrival estimation for whom model mismatch is often a secondary consideration, calibration algorithms are principally focused on quantifying model mismatch. Much of the model mismatch in antenna arrays comes from sources such as device non-uniformities resulting channel gain/phase variations [1, p. 67], sensor placement tolerances [1, p.67–70] and mutual coupling between elements [25, p. 396–397]. Although some mismatch can be attributed to thermal effects [26, 27]. Almost ironically, many calibration methods attempt to model the model mismatch by making assumptions about the form of the solution and derive parameters from this model. Such techniques have been developed that focus on channel gain/phase variations [28, 29] as well as mutual coupling [30, 31] and sensor placement [32]. Some works have also focused on joint estimation of these effects [33] while others have developed methods that are model independent [34]. Model mismatch affects every aspect of array processing and care must be taken to understand the limits of our knowledge of an array or else we will often find the array is not performing up to our expectations.

1.2 Direction of Arrival Estimation

Direction of arrival estimation algorithms play an important role in many modern systems. The trend in communication systems is away from sector antennas that illuminate a large coverage swath, which results in a large percentage of the transmitted power being wasted, towards adaptive beamforming to individually illuminate users. This requires specific knowledge of the user's location or an estimation of the direction of arrival of each user's signal, which is typically not known. On the other hand, radars typically know the direction of arrival of its intended target, as they measure the range to a target by transmitting a signal in a specific direction and measure the return echo from that same angle. However, DoA

estimation algorithms play an important role in mitigating interference sources such as jammers and clutter who are not limited to the mainbeam and thus the DoA is unknown. In this section we take a high level look at several classes of DoA algorithms and highlight the different methodology of some well known algorithms.

The first, and probably most intuitive, class of DoA estimation algorithms we will examine can loosely be described as beamscanning methods. These methods essentially use beamforming techniques to sweep a beam over a desired set of angles and records the received signal variance as a function of angle. A decision is then made to pick the DoA of the incident signals, typically either by some detection threshold or by picking a number of peaks based on the expected number of incident signals. While any method can be used to do the beamforming step, the Capon beamforming method [35] is very widely used [36, 37]. While beamscan techniques are relatively intuitive and have a low computational cost, they generally do not perform as well other techniques.

The next group of DoA estimators we will examine leverage the eigen-structure of a sample covariance matrix. Eigen-method DoA estimators include both MUSIC [38] and ESPRIT [39]. MUSIC takes advantage of the orthogonality between a signal vector and a noise subspace eigenvector to estimate the direction of arrival. In contrast, ESPRIT leverages the phase shift between two identical subarrays to do the same. Both of these methods show performance improvement over beamscan methods[40, 41], but require the number of incident signals to be known to perform properly.

The last DoA estimator we examine is RISR [12, 13]. The RISR algorithm is a recursive minimum mean-squared error DoA estimator that does not use a sample covariance matrix in part by leveraging knowledge of the array response. This allows RISR to avoid the sample support issues in forming a sample covariance matrix that limits eigen-method algorithm's performance when sample support is low. RISR is much younger then the DoA methods mentioned thus far, but it is already seeing use in radar system applications [42]. Regardless of the method, direction of arrival estimators play an important role in modern systems and

their performance will be examined in detail as part of this dissertation.

1.3 Proposed Approach

This dissertation delves into the realm of array model mismatch within the context of direction of arrival estimation in an effort to show how traditional simplifying assumptions are limiting the performance of array processing algorithms. Engineers are virtually surrounded by models of the physical world and they use these models to develop useful and meaningful systems. For better, or for worse, the world is very complex and difficult to model. In the few cases that engineering models capture all, or even most, of the intricacies of the real world, working with these models can be difficult and intractable. Engineers therefore develop simplifying assumptions that remove complexity in exchange for tractability. However, when they make this trade-off, engineers are also giving up performance for tractability, as any design decisions based on the simplified model is no longer firmly rooted in the physical world, but rather a pale facsimile of the real world. This body of work seeks to illustrate this performance trade-off and to develop techniques to deal with the added complexity necessary to recapture some of that lost performance. This will be accomplished first by developing a blind array calibration technique paired with the RISR DoA estimation algorithm that is capable of estimating the individual channel gain/phase mismatch and the mutual coupling between elements. In estimating these model mismatch parameters the performance of RISR can be enhanced. Subsequently, model mismatch is examined in the context of transmit array performance verses receive array performance, and how substituting one for the other can degrade the performance of DoA estimators.

Blind array calibration sits firmly at the intersection of model mismatch and direction of arrival estimation. Array calibration, in general, attempts to quantify some of the physical realities that arise from implementing an array, and pairing this process with a direction of arrival estimator can be mutually beneficial. The calibration process requires accurate

knowledge of the location of the signals of incidence, while the DoA algorithm can be improved by incorporating the calibration estimates into a signal model that is aligned more closely with reality. The calibration method developed herein uniquely builds upon RISR's current model mismatch robustness and is unique in that other blind calibration methods require the use of a sample covariance matrix. By avoiding a SCM dependence our calibration method can operate in low sample support environments, making it relevant and a principal choice for such environments. We will also show that the new calibration enhancement has some robustness to coherent sources, and so is of interest to systems that frequency encounter multipath. After developing the method we will show that it is effective both at improving RISR's DoA estimates, as well as, estimating the channel gain/phase variations and array mutual coupling. We will also explore the convergence region of the calibration method using Monte Carlo trials and propose several methods to extend the convergence region by incorporating prior calibration data.

Model mismatch is not always caused by physical realities that calibration can measure. Sometimes model mismatch is caused by the misapplication of theory on the part of engineers. We study this type of mismatch by examining how the performance of a transmitting array can differ from the same array's receive performance. We will show that this mismatch is caused by interactions within front-end transceiver hardware that results in mode dependent loading on the array elements. This approach is unique in its consideration of hardware effects as existing literature simplifies the hardware down to Thévenin circuit approximations that masks this nuance. This new approach is interesting as it highlights this model oversimplification and is relevant anywhere that such an approximation has been made. In addition to identifying the cause of this type of model mismatch, this work shows that the mismatch can degrade the performance of some DoA estimation algorithms.

1.4 Document Overview

The rest of this body of work is divided into four main chapters. In Chapter 2 we delve into the theory and practice of direction of arrival estimation. Many of the estimation algorithms review Chapter 2 will reemerge throughout the rest of this work and they form the foundation of much of this dissertation. In Chapter 3 we review array calibration in depth before developing the RISR Array Calibration Enhancement (RACE) algorithm. RACE is a blind array calibration routine that pairs with RISR to simultaneously produce the direction of arrival of incident signals and an estimation of the mutual coupling and channel gain/phase variations. Chapter 4 investigates the impact of substituting the transmit array manifold in place of the receive array manifold on direction of arrival estimation algorithms. Finally Chapter 5 draws conclusions and maps out future work.

Chapter 2

Radar Array Processing

Array processing plays an ever growing role in modern radar systems, and in this chapter we examine some common direction of arrival estimators. While the topic of radar array processing is much more expansive than direction of arrival estimation, much of the work in the following chapters examines the impact of array model mismatch within the context of direction of arrival estimators. But before we can explore these intricacies it's important to have a grasp of these fundamental algorithms. To that end we will look at the MUSIC algorithm in Section 2.1.1, the ESPRIT algorithm in Section 2.1.2 and finally the RISR algorithm in Section 2.1.3. The first two algorithms are eigen-methods that leverage the eigen-structure of a sample covariance matrix, while the final algorithm is a recursive minimum mean-squared error. All three methods are based on an array signal model for Q signals incident upon an N element array

$$\mathbf{y} = \mathbf{A}\mathbf{x} + \mathbf{v}, \tag{2.1}$$

where $\mathbf{x}$ is a Q length vector of incident signals, $\mathbf{A}$ is an $N \times Q$ array manifold and $\mathbf{v}$ is additive noise. The array manifold composed of Q N-length steering vectors

$$\mathbf{A} = \begin{bmatrix} \mathbf{a}(\psi_1) & \mathbf{a}(\psi_2) & \cdots & \mathbf{a}(\psi_Q) \end{bmatrix} \tag{2.2}$$

that describe each element's response to the ith signal arriving from direction ψ_i. Each algorithm is then unique in how it derives ψ_i from the sampled array response $\mathbf{y}$.

2.1 Direction of Arrival Estimation

In this section we consider the basis of operation for three DoA estimation algorithms. In Sections 2.1.1 and 2.1.2 we examine some eigen-based DoA estimation methods by reviewing the MUSIC and ESPRIT algorithms. Section 2.1.3 then delves into the RISR recursive minimum mean-squared error DoA estimator. These algorithms form a foundation for much of this dissertation and this section servers as an introduction to the respective algorithms.

2.1.1 MUSIC

The first direction of arrival estimator we consider is the Multiple Signal Classification (MUSIC) algorithm. MUSIC is an eigen-based DoA estimator that leverages orthogonality of the signal and noise subspaces of the sample covariance matrix. We start by forming a covariance matrix for each term in (2.1) where

$$\mathbf{R_x} = \sum_{i=1}^{Q} \alpha_i \mathbf{a}(\psi_i)\mathbf{a}^H(\psi_i), \tag{2.3}$$

where α_i is the amplitude of the ith signal, $\mathbf{R_v}$ is then

$$\mathbf{R_v} = \sum \mathbf{v}\mathbf{v}^H. \tag{2.4}$$

Rewriting (2.1) in terms of the covariance matrix then defines the sample covariance matrix

$$\mathbf{R_y} = \mathbf{R_x} + \mathbf{R_v}. \tag{2.5}$$

Taking the eigendecomposition of the sample covariance matrix produces a set of eigenvalues and eigenvectors such that

$$\mathbf{R_y} = \sum_{i=1}^{Q} \lambda_i \mathbf{u}_i \mathbf{u}_i^H + \sum_{i=1}^{N} \sigma_i^2 \mathbf{u}_i \mathbf{u}_i^H, \tag{2.6}$$

where it has been assumed that $\mathbf{v}$ is additive white noise with noise variance σ^2. Rearranging the summation limits to be non-overlapping brings us to your final format

$$\mathbf{R_y} = \sum_{i=1}^{Q} (\lambda_i + \sigma_i^2) \mathbf{u}_i \mathbf{u}_i^H + \sum_{i=Q+1}^{N} \sigma_i^2 \mathbf{u}_i \mathbf{u}_i^H. \tag{2.7}$$

From (2.7) we can see the sample covariance matrix is spanned by two orthogonal subspaces, a signal subspace spanned by

$$\mathbf{U}_s = \begin{bmatrix} \mathbf{u}_1 & \mathbf{u}_2 & \cdots & \mathbf{u}_Q \end{bmatrix} \tag{2.8}$$

and a noise subspace spanned by

$$\mathbf{U}_n = \begin{bmatrix} \mathbf{u}_{Q+1} & \mathbf{u}_{Q+2} & \cdots & \mathbf{u}_N \end{bmatrix} \tag{2.9}$$

These orthogonal subspaces make up the crux of the MUSIC algorithm.

MUSIC leverages the orthogonality of the sample covariance matrix by recognizing that the projection of a signal vector into the noise subspace will be identically zero

$$\mathbf{a}^H(\psi_i)\mathbf{U}_n = \mathbf{0}_{1\times N-Q}. \tag{2.10}$$

where $\mathbf{0}_{1\times N-Q}$ is a vector of zeros. Since ψ_i is the unknown we seek to find, MUSIC forms a test signal vector $\mathbf{a}(\psi)$ defined over all ψ to project into the noise subspace

$$J(\psi)_{\text{MUSIC}} = \sum_{i=Q+1}^{N} |\mathbf{a}^H(\psi)\mathbf{u_i}|^2. \tag{2.11}$$

Q minima of (2.11) can then be found, or conversely a pseudo-spectrum of $1/J(\psi)_{\text{MUSIC}}$ can be plotted against ψ and Q maximums can be found.

2.1.2 ESPRIT

The Estimation of Signal Parameter Via Rotational Invariance Techniques (ESPRIT) is the second DoA estimation algorithm we consider. ESPRIT, like MUSIC, is an eigen-based method, but unlike MUSIC ESPRIT does not explicitly depend on knowledge of the array manifold. It does this in part by leveraging the fact that two arrays, separated by a small distance, incident upon by the same signal will see phase shift in the incident signal that is dependent on the arrival angle. ESPRIT fundamentally divides an array into two subarrays and looks for this phase shift between the signals received by each array. We start by examining this subarray geometry, before delving into the ESPRIT methodology.

While there are many ways to subdivde an array, for the sake of brevity we will consider the N element array in Figure 2.1 that has been subdivided into two $N_s = N - 1$ length subarrays that are offset by a single element spacing. We define a pair of selection matrices

$$\mathbf{J}_{s1} = \begin{bmatrix} \mathbf{I}_{N_s \times N_s} & | & \mathbf{0}_{N_s \times 1} \end{bmatrix} \tag{2.12}$$

and

$$\mathbf{J}_{s2} = \begin{bmatrix} \mathbf{0}_{N_s \times 1} & | & \mathbf{I}_{N_s \times N_s} \end{bmatrix} \tag{2.13}$$

that can be used to relate the array manifold of the full array to the array manifold of either subarray as

$$\mathbf{A}_{s1} = \mathbf{J}_{s1}\mathbf{A} \tag{2.14}$$

and

$$\mathbf{A}_{s2} = \mathbf{J}_{s2}\mathbf{A}. \tag{2.15}$$

We can now express the phase shift relationship between the two subarrays as

$$\mathbf{A}_{s1} = \mathbf{A}_{s2}\mathbf{\Phi}, \tag{2.16}$$

where $\mathbf{\Phi}$ is the phase shift at each angle such that

$$\mathbf{\Phi} = \text{diag}\left[e^{jd\psi_1} \quad e^{jd\psi_2} \quad \ldots \quad e^{jd\psi_Q},\right] \tag{2.17}$$

We pause here to note that this phase shift relationship is present not only for the array manifolds but also for the eigenvectors of the signal subspace. The signal subspace eigenvectors can be related as

$$\mathbf{U}_{s1}\mathbf{\Psi} = \mathbf{U}_{s2}, \tag{2.18}$$

where the elements of $\mathbf{\Phi}$ are the eigenvalues of $\mathbf{\Psi}$. It should also be noted that the signal subspace eigenvectors $\mathbf{U}_{s1}$ and $\mathbf{U}_{s2}$ are related to the array signal subspace eigenvectors by the same selection matrices $\mathbf{J}_{s_1}$ and $\mathbf{J}_{s_2}$ used earlier to relate the array manifolds.

With all the basic concepts in place we can now examine the ESPRIT algorithm. ESPRITS starts by forming a sample covariance matrix and performing an eigendecompostion, dividing the resulting eigenvectors into a signal and noise subspace as seen in (2.7). It then projects the signal subspace onto the subarrays using (2.12) and (2.13) to form (2.18). Matrix $\mathbf{\Psi}$ in Equation (2.18) can then be solved in a number of ways, although least-squares and total least-squares are predominant. Once $\mathbf{\Psi}$ is known, an eigendecompostion is performed to obtain the eigenvalues, which are the complex values seen in (2.17), and the DoA estimates are derived from the argument of each eigenvalue.

ESPRIT produces a direction of arrival estimate without explicit knowledge of the array manifold, by assuming the two subarrays have identical manifolds. Like MUSIC it is based on the eigen-structure of a sample covariance matrix. And in practice one must know the number of incident signals to correctly form the signal subspace.

2.1.3 RISR

The ReIterative Super Resolution (RISR) algorithm [12, 13] may be applied to a wide variety of antenna array geometries and unlike MUSIC and ESPRIT does not depend on the eigen-

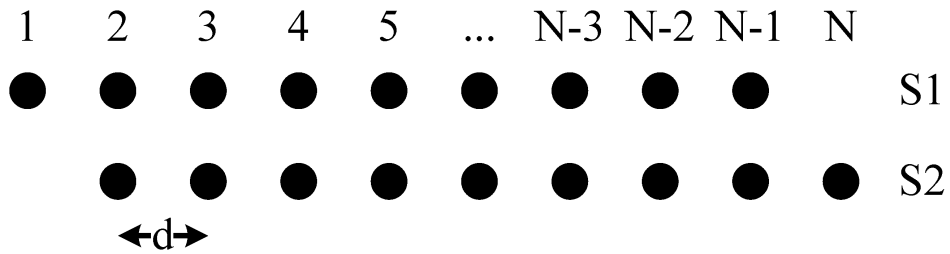

Figure 2.1: ESPRIT subarray geometry

structure of a sample covariance matrix. MUSIC and ESPRIT also need to know the number of incident signals Q, in practice Q is estimated prior to the beginning of MUSIC or ESPRIT. Rather than relay on knowledge of Q, RISR forms an $N \times M$ array manifold with M steering vectors

$$\mathbf{A} = [\mathbf{a}(0), \mathbf{a}(\psi_\Delta), \ldots, \mathbf{a}((M-1)\psi_\Delta)]. \tag{2.19}$$

The matrix $\mathbf{A}$ contains M steering vectors denoted by $\mathbf{a}(m\psi_\Delta)$ that are equally spaced over 2π at increments of $\psi_\Delta = 2\pi/M$. The vector $\mathbf{x}$ is $M \times 1$ and contains complex amplitudes representing the underlying source signals and the additive noise $\mathbf{v}$ is an $N \times 1$ vector. Using this method $M >> Q$ and $\mathbf{x}$ is typically sparse. The RISR algorithm calculates an $M \times N$ adaptive filter bank $\mathbf{W}$ by minimizing the cost function

$$J_{\text{RISR}} = E\{\|\mathbf{x} - \mathbf{W}^H \mathbf{y}\|^2\} \tag{2.20}$$

that has a well known Minimum Mean-Square Error (MMSE) solution

$$\mathbf{W} = (E\{\mathbf{y}\mathbf{y}^H\})^{-1} E\{\mathbf{y}\mathbf{x}^H\}. \tag{2.21}$$

By relying on an assumed model of the array response $\hat{\mathbf{A}}$, (2.21) can be simplified by substituting (2.1) into (2.21) resulting in

$$\mathbf{W} = (\hat{\mathbf{A}} E\{\mathbf{x}\mathbf{x}^H\} \hat{\mathbf{A}}^H + \mathbf{R})^{-1} \hat{\mathbf{A}} E\{\mathbf{x}\mathbf{x}^H\}, \tag{2.22}$$

where $\mathbf{R} = E\{\mathbf{v}\mathbf{v}^H\}$. The derivation of RISR [13] then assumes no temporal correlations between incident signals, subsequently enforcing this assumption by defining a spectral power distribution matrix

$$\mathbf{P} = E\{\mathbf{x}\mathbf{x}^H\} \odot \mathbf{I}_{M\times M}, \tag{2.23}$$

where $\mathbf{I}_{M\times M}$ is an $M \times M$ identity matrix and $\odot$ is the Hadamard product. The assumption of no temporal correlation was made in [13] to facilitate a mathematically tractable solution. However, it was also shown in [13] that RISR still performs well when temporal correlation between sources is present.

RISR can be extended to L time samples by letting

$$\mathbf{Y} = [\mathbf{y}(0), \mathbf{y}(1), ..., \mathbf{y}(L-1)] \tag{2.24}$$

with associated

$$\mathbf{X} = [\mathbf{x}(0), \mathbf{x}(1), ..., \mathbf{x}(L-1)], \tag{2.25}$$

and thus implementing (2.23) as

$$\mathbf{P} = \left[\frac{1}{L}\sum_{\tau=0}^{L-1} \mathbf{X}(\tau)\mathbf{X}^H(\tau)\right] \odot \mathbf{I}_{M\times M}. \tag{2.26}$$

Substituting (2.23) and (2.26) into (2.22) then yields

$$\mathbf{W} = (\hat{\mathbf{A}}\mathbf{P}\hat{\mathbf{A}}^H + \mathbf{R})^{-1}\hat{\mathbf{A}}\mathbf{P}. \tag{2.27}$$

RISR also has a build in tolerance for model uncertainty. This is accomplished by the addition of a model noise loading factor

$$\mathbf{R}_z = \sigma_z^2 \mathbf{I}_{M\times M} \odot \left(\mathbf{A}\mathbf{P}\mathbf{A}^H\right), \tag{2.28}$$

where σ_z is the model noise variance. It was shown by Blunt [13] that this additional signal dependent regularization term to the matrix inversion in (2.27) allows for $\mathbf{R}$ to be reduced, improving the sensitivity of the RISR algorithm. Including (2.28) in (2.27) yields

$$\mathbf{W} = (\hat{\mathbf{A}}\mathbf{P}\hat{\mathbf{A}}^H + \alpha\mathbf{R} + \mathbf{R}_z)^{-1}\hat{\mathbf{A}}\mathbf{P}. \tag{2.29}$$

Where $0 < \alpha < 1$ is the scaling factor on the noise covariance matrix. The spatial spectrum $\mathbf{x}$ and the MMSE filter bank $\mathbf{W}$ are thus estimated in an alternating manner [13]. RISR initially estimates the array input $\hat{\mathbf{x}}$ using a matched filter bank as $\hat{\mathbf{x}} = \hat{\mathbf{A}}^H\mathbf{y}$ then sequentially estimates the spectral power distribution $\hat{\mathbf{P}}$ by replacing $\mathbf{X}$ with $\hat{\mathbf{X}}$ in (2.26), and subsequently the MMSE filter bank $\mathbf{W}$ by using (2.27). This process is repeated until convergence is reached.

2.2 Summary

In this chapter we explored three different direction of arrival estimators. These estimators included MUSIC, ESPRIT and RISR. In each case it was assumed that the estimation algorithm was operating on a common idealized array signal model. Much of the following chapters involve the impacts of a non-ideal array manifold on these algorithms.

Chapter 3

RISR Array Calibration Estimation

Adaptive array processing is only as good as its underlying model, and inaccuracies in the array model can degrade the performance of almost any algorithm. In this chapter we develop the RISR Array Calibration Enhancement (RACE) to simultaneously estimate the direction of arrival of incident signals and the effects of mutual coupling and channel imbalances. In addition, we will show that RACE enhances RISR's built-in robustness to model mismatch, and improve RISR's DoA estimates in the presence of channel gain/phase mismatch and array mutual coupling. We will also show that RACE is effective for a wide range of channel gain mismatch, but a narrower range of channel phase mismatch. This limitation is overcome by developing two methods to integrate prior calibration data into RACE. This is unique as existing works consider either traditional calibration problem or the blind-calibration problem without considering how to incorporate knowledge from one to the other. Before we can derive the RACE algorithm we examine the physical realities inherent in building an array as well as methods to incorporate these realities into our array model in Section 3.1. We then present the RACE algorithm in Section 3.2 and evaluate its performance on simulated data in Section 3.3.

3.1 Background

Before developing the RACE blind array calibration routine it is beneficial to take a high level look at the adaptive array signal model and understand how array geometry and the physical realities of building a system can effect the model. Real arrays are subject to a number of confounding factors such as channel gain/phase mismatch, mutual coupling between array elements and sensor position uncertainty. If left unaccounted for these confounding factors can significantly degrade the performance of the array. Calibration at its core attempts to measure, and the degree possible, remove these confounding factors. Section 3.1.1 starts by developing an idealized array signal model for arbitrary array geometry, before giving specific examples using a uniform linear array and a uniform circular array. It then examines the effect of channel gain/phase fluctuations, mutual coupling and sensor placement uncertainty. Section 3.1.2 then surveys existing calibration methods and examines the difference between traditional calibration and blind calibration methods.

3.1.1 Array Model

The foundation of any array processing technique is the underlying signal model that is firmly rooted in a physical reality. Consider an array of N sensors with Q incident signals. The combined signal present at the nth sensor can be written

$$y_n(t) = \sum_{q=1}^{Q} x_q(t - \tau_{nq}) + \nu_n(t) \tag{3.1}$$

where x_q is the qth signal, τ_{nq} is the delay between signal q and sensor n, and ν_n is additive noise. Under the narrowband assumption (3.1) can be expressed in terms of its Fourier transform.

$$Y_n(f) = \sum_{q=1}^{Q} e^{-j\omega_0 \tau_{nq}} X_q + V_n \tag{3.2}$$

where Y, X, and V are the Fourier transforms of y, x, and ν, respectively. Generally, the absolute time delay between a distant source a each sensor is unknown and (3.2) recast using the relative positions of each sensor to a central origin

$$\tau_n = -\frac{1}{c}[b_x \cdot p_{xn} + b_y \cdot p_{yn} + b_z \cdot p_{zn}], \tag{3.3}$$

where

$$\mathbf{b} = \begin{bmatrix} b_x \\ b_y \\ b_z \end{bmatrix} \tag{3.4}$$

are orthogonal unit vectors in cartesian coordinate system, and

$$\mathbf{p}_n = \begin{bmatrix} p_{xn} \\ p_{yn} \\ p_{zn} \end{bmatrix} \tag{3.5}$$

describes the position of the nth sensor. Substituting (3.4) and (3.5) into (3.3) yields

$$\tau_n = -\frac{\mathbf{b}^T \mathbf{p}_n}{c} \tag{3.6}$$

Plane wave propagation is often described in terms of wavenumber $\mathbf{k}$ such that

$$\mathbf{k} = -\frac{\omega}{c}\mathbf{b} = -\frac{2\pi}{\lambda}\mathbf{b}. \tag{3.7}$$

By letting τ_n replace τ_{nq} and substituting (3.7) into (3.2) produces

$$Y_n(f) = \sum_{q=1}^{Q} e^{-j\mathbf{k}^T \mathbf{p}_n} X_q + V_n. \tag{3.8}$$

This formulation leads to the familiar array manifold [1, p. 23–32]

$$\mathbf{y} = \mathbf{A}\mathbf{x} + \mathbf{v}, \tag{3.9}$$

where $\mathbf{A}$ is an $N \times Q$ matrix referred to the array manifold such that

$$\mathbf{A} = \begin{bmatrix} e^{-j\mathbf{k}_1^T \mathbf{p}_0} & e^{-j\mathbf{k}_2^T \mathbf{p}_0} & \dots & e^{-j\mathbf{k}_Q^T \mathbf{p}_0} \\ e^{-j\mathbf{k}_1^T \mathbf{p}_1} & e^{-j\mathbf{k}_2^T \mathbf{p}_1} & \dots & e^{-j\mathbf{k}_Q^T \mathbf{p}_1} \\ \vdots & \vdots & \ddots & \vdots \\ e^{-j\mathbf{k}_1^T \mathbf{p}_{N-1}} & e^{-j\mathbf{k}_2^T \mathbf{p}_{N-1}} & \dots & e^{-j\mathbf{k}_Q^T \mathbf{p}_{N-1}} \end{bmatrix}, \tag{3.10}$$

where $\mathbf{k}_q$ refers to the wavenumber of the qth incident signal. Each column of $\mathbf{A}$ describes the induced response of each element in the array to a single incident signal and is referred to as a steering vector.

In general, the number of sources and their angles of arrival is not known and matrix $\mathbf{A}$ as presented in (3.10) cannot be formed. Instead, $\mathbf{A}$ is formed as an $N \times M$ matrix such that

$$\mathbf{A} = [\mathbf{a}_0(0), \mathbf{a}_1(\psi_\Delta), \dots, \mathbf{a}_{M-1}((M-1)\psi_\Delta)]. \tag{3.11}$$

contains M steering vectors denoted by $\mathbf{a}(m\psi_\Delta)$ that are equally spaced over 2π at increments of $\psi_\Delta = 2\pi/M$. The vector $\mathbf{x}$ is then expanded to an $M \times 1$ vector that contains complex amplitudes representing the underlying source signals and is referred to as the incident spatial spectrum. As $M >> Q$ $\mathbf{A}$, as defined in (3.11), subsumes the previous definition.

We now turn our attention to the steering vectors of some common array geometries by examining a uniform linear array and a uniform circular array. For the uniform linear array

in Figure 3.1 the position vector for the nth element can be written

$$\mathbf{p}_n = \begin{bmatrix} 0 \\ 0 \\ \left(n - \frac{N-1}{2}\right)d \end{bmatrix}. \tag{3.12}$$

Then by using the conventional definition for orthogonal unit vectors in a spherical coordinate systems

$$\mathbf{b} = \begin{bmatrix} \sin\theta\cos\phi \\ \sin\theta\sin\phi \\ \cos\theta \end{bmatrix} \tag{3.13}$$

the mth steering vector becomes

$$\mathbf{a}_m = \left[e^{-j\mathbf{k}_m^T\mathbf{p}_1}, e^{-j\mathbf{k}_m^T\mathbf{p}_2}, \ldots, e^{-j\mathbf{k}_m^T\mathbf{p}_N}\right]^T \tag{3.14}$$

$$= \left[e^{j\left(n-\frac{N-1}{2}\right)\mathbf{k}_m d\cos\theta}, e^{j\left(n-\frac{N-1}{2}-1\right)\mathbf{k}_m d\cos\theta}, \ldots, e^{-j\left(n-\frac{N-1}{2}\right)\mathbf{k}_m d\cos\theta}\right]. \tag{3.15}$$

Similarly, from the uniform circular array seen in Figure 3.2 the position vector of the ϕ_nth element becomes

$$\mathbf{p}_{\phi_n} = R\begin{bmatrix} \cos\phi_n \\ \sin\phi_n \\ 0 \end{bmatrix} \tag{3.16}$$

where ϕ_n is the angle to the nth element. Thus,

$$\mathbf{k}_m^T\mathbf{p}_{\phi_n} = -\frac{2\pi}{\lambda}R\sin\theta[\cos(\phi-\phi_n)] \tag{3.17}$$

and the mth steering vector becomes

$$\mathbf{a}_m = \left[e^{\left(j\frac{2\pi}{\lambda}R\sin\theta[\cos(\phi-\phi_1)]\right)}, e^{\left(j\frac{2\pi}{\lambda}R\sin\theta[\cos(\phi-\phi_2)]\right)}, \ldots, e^{\left(j\frac{2\pi}{\lambda}R\sin\theta[\cos(\phi-\phi_N)]\right)}\right]^T. \tag{3.18}$$

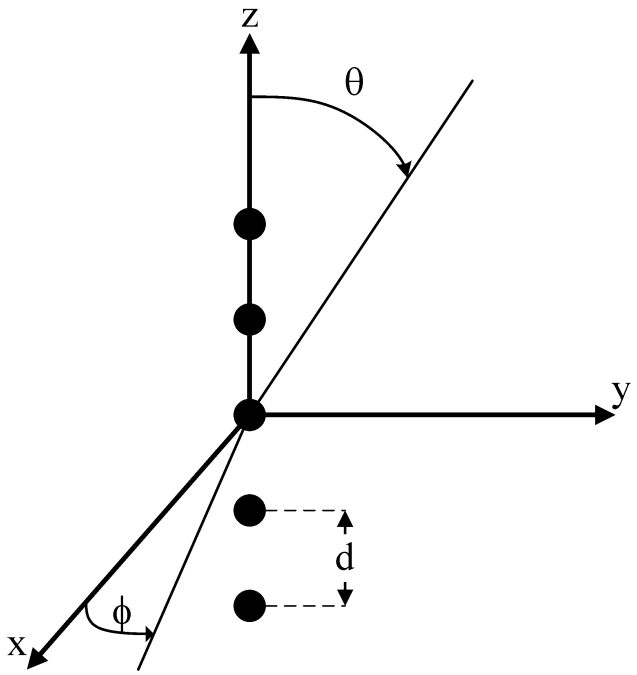

Figure 3.1: Z-directed uniform linear array

The array signal model thus far considered is an idealistic representation of the physical world, and a number of confounding factors such as gain or phase fluctuation, mutual coupling and sensor placement uncertainty can perturb the model. The rest of this section is devoted to modeling these perturbations, as well as, laying the groundwork for calibration.

3.1.1.1 Channel Gain/Phase Mismatch

The gain and phase of each receive element channel can vary due to passive components such as small variations in signal routing paths or active components due to differences between the channel amplifiers and phase shifters. Regardless of the cause, amplitude and phase imbalances can be imparted. These imbalances modify (3.8) by adding a complex exponential to represent the channel gain and phase offset

$$Y_n(f) = \sum_{q=1}^{Q} \alpha_n e^{-j\omega_0 \zeta_n} e^{-j\mathbf{k}^T \mathbf{p}_n} X_q + V_n. \tag{3.19}$$

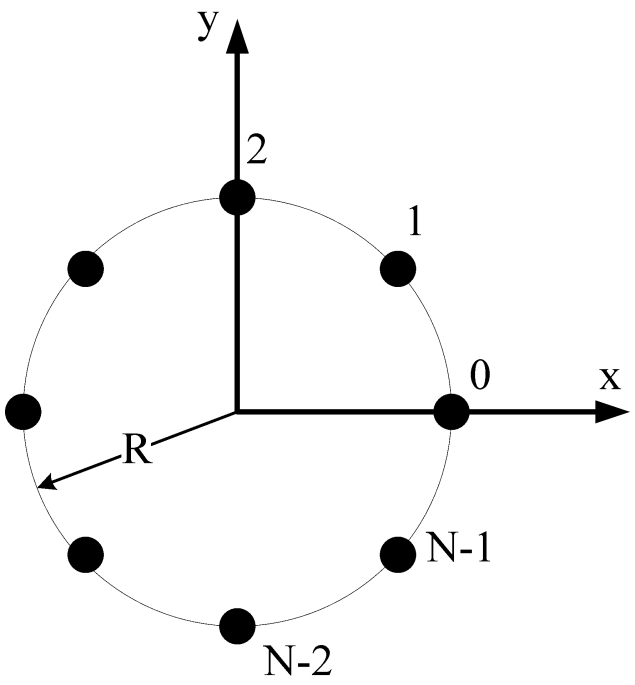

Figure 3.2: Uniform circular array geometry

where α_n and ζ_n are the nth channel gain and phase respectively. Examining (3.19) it is apparent that gain and phase perturbations are unique to each sensor and can be cast into an $N \times N$ diagonal matrix

$$\mathbf{S} = \mathbf{\Gamma A} \tag{3.20}$$

$$\mathbf{\Gamma} = \text{diag}[\alpha_1 e^{-j\omega_0\zeta_1}, \alpha_2 e^{-j\omega_0\zeta_2}, \ldots, \alpha_N e^{-j\omega_0\zeta_N}] \tag{3.21}$$

where $\mathbf{S}$ represents the true array manifold and $\mathbf{A}$ is the ideal manifold from (3.10).

Substituting (3.20) into (3.9) produces a signal model that includes the effects of gain/phase fluctuations

$$\mathbf{y} = \mathbf{\Gamma A x} + \mathbf{v}. \tag{3.22}$$

It is possible to estimate $\mathbf{\Gamma}$ from $\mathbf{y}$ provide the spatial spectrum vector $\mathbf{x}$ is know. Friedlander

estimated the N unknowns in $\mathbf{\Gamma}$ by extracting them an placing them in a $N \times 1$ vector as [20]

$$\begin{aligned} \mathbf{y} &= \mathbf{\Gamma}(\mathbf{Ax}) + \mathbf{v} \\ &= Q_1[\mathbf{Ax}]\boldsymbol{\gamma} + \mathbf{v} \end{aligned} \tag{3.23}$$

where $\boldsymbol{\gamma}$ is an $N \times 1$ vector of complex gain/phase unknowns

$$\boldsymbol{\gamma}_i = \mathbf{\Gamma}_{ii} \quad \text{for i = 1, 2,..., N} \tag{3.24}$$

and transformation function $Q_1[\mathbf{z}]$ is defined as

$$(Q_1[\mathbf{z}])_{ij} = \mathbf{z}_i \bullet \delta_{ij} \quad \text{i,j= 1, 2,..., N.} \tag{3.25}$$

This allows the channel gain and phase terms to be estimated using a least squares methodology

$$\boldsymbol{\gamma} = (Q_1[\mathbf{Ax}])^{-1}\mathbf{y}. \tag{3.26}$$

3.1.1.2 Mutual Coupling

Signal energy incident on an element of an antenna array is not always completely absorbed by that element. Some of this energy can be reflected and reradiated only to be received by the other elements in the array. The reception of this reradiated energy mutually couples elements in the array together. Thus, mutual coupling causes the signal received at each array element to no longer simply be the direct incident signal, but the sum of the direct incident signal and the signals reradiated by the other elements in the array. This phenomena modifies the discrete idealized array manifold $\mathbf{A}$ by adding a $N \times N$ Mutual Coupling Matrix (MCM) as

$$\mathbf{S} = \mathbf{CA}. \tag{3.27}$$

Under ideal conditions $\mathbf{C}$ reduces to an identity matrix and the true array manifold is equal to the ideal array manifold.

The structure of the mutual coupling matrix $\mathbf{C}$ is highly dependent on the physical structure of the array. Noting that mutual coupling tends to be reciprocal and dependent on the distance between elements allows the loose characterization of some common array geometries. For example, uniform linear arrays have a regular fixed separation between elements. Due to the mutual coupling's dependence on element separation, the ith and $(i+1)$th elements will have the same mutual coupling for any value of i, resulting in a banded Toeplitz mutual coupling matrix [20]. In addition to linear arrays, this regular element spacing also holds true for circular arrays and likewise results in a banded structure for the MCM. However, unlike linear arrays, circular arrays wrap back around to the starting element giving the MCM additional bands in the upper-right and lower left corners.

In general the mutual coupling matrix $\mathbf{C}$ contains $\frac{N!}{2(N-2)!}$ unknowns as each element has a unique, but reciprocal mutual coupling term to each of the other $N-1$ elements. However, most arrays have a regular structure that reduces the number of unknowns. This work considers Uniform Linear Arrays (ULA) and Uniform Circular Arrays (UCA), both of which have a regular structure that reduces the number of unique terms. A ULA has a banded complex symmetric Toeplitz structure for $\mathbf{C}$ while the MCM for a UCA is a complex symmetric circulant matrix [20]. In both cases the number of unknowns is reduced to $N-1$.

Similar to estimating the gain/phase matrix, the estimation process for the mutual coupling matrix leverages the structure of $\mathbf{C}$ and a matrix transformation to extract the unknown values from $\mathbf{C}$ and places them into an $N \times 1$ vector. Both the mutual coupling model and the transformation methods were developed in [20] for a MUSIC based blind calibration algorithm, and are used here with RISR. For a ULA and the accompanying banded complex

symmetric Toepliz matrix $\mathbf{C}$ this transformation takes the form

$$\begin{aligned} \mathbf{y} &= \mathbf{C}(\mathbf{Ax}) + \mathbf{v} \\ &= Q_2[\mathbf{Ax}]\mathbf{c} + \mathbf{v} \\ &= (\mathbf{B_1} + \mathbf{B_2})\mathbf{c} + \mathbf{v} \end{aligned} \tag{3.28}$$

where $\mathbf{c}$ is the $N \times 1$ vector containing the unknown mutual coupling terms and the function $\mathrm{Q}_2[\mathbf{z}]$ is defined [20] as the sum of two $N \times N$ matrices $\mathbf{B}_1$ and $\mathbf{B}_2$

$$[\mathbf{B}_1]_{pq} = \begin{cases} \mathbf{z}_{p+q-1} & \text{for } p+q+1 \leq N+1 \\ 0 & \text{otherwise} \end{cases} \tag{3.29}$$

$$[\mathbf{B}_2]_{pq} = \begin{cases} \mathbf{z}_{p-q+1} & p \geq q \geq 2 \\ 0 & \text{otherwise.} \end{cases} \tag{3.30}$$

The indices p and q index the rows and columns of B_1 and B_2 as well as the complex vector $\mathbf{z} = \mathbf{Ax}$. This form allows the mutual coupling matrix to be decomposed from a matrix of N^2 redundant values into a vector of $N-1$ unique values.

Similarly, the mutual coupling matrix for a circular array has structured redundancy that can be leveraged. Now instead of being banded Toeplitz, the mutual coupling matrix is a banded circulant matrix [20], but still only has N unique values. Again these $N-1$ unique values can be extracted as

$$\begin{aligned} \mathbf{y} &= \mathbf{C}(\mathbf{Ax}) + \mathbf{v} \\ &= Q_3[\mathbf{Ax}]\mathbf{c} + \mathbf{v} \\ &= (\mathbf{B}_1 + \mathbf{B}_2 + \mathbf{B}_3 + \mathbf{B}_4)\mathbf{c} + \mathbf{v} \end{aligned} \tag{3.31}$$

where the function $Q_3[\mathbf{z}]$ is defined [20] as the sum of four $N \times N$ matrices

$$[\mathbf{B}_1]_{pq} = \begin{cases} \mathbf{z}_{p+q-1} & \text{for } p+q+1 \leq N+1 \\ 0 & \text{otherwise} \end{cases} \tag{3.32}$$

$$[\mathbf{B}_2]_{pq} = \begin{cases} \mathbf{z}_{p-q+1} & p \geq q \geq 2 \\ 0 & \text{otherwise} \end{cases} \tag{3.33}$$

$$[\mathbf{B}_3]_{pq} = \begin{cases} \mathbf{z}_{M+1+p-q} & p < q \leq l \\ 0 & \text{otherwise} \end{cases} \tag{3.34}$$

$$[\mathbf{B}_4]_{pq} = \begin{cases} \mathbf{z}_{p+q-M-1} & 2 \leq q \leq l, p+q \leq N+2 \\ 0 & \text{otherwise.} \end{cases} \tag{3.35}$$

Equations (3.28) and (3.31) can now be solved using a least squares method to estimate the mutual coupling terms in $\mathbf{c}$.

3.1.1.3 Sensor Placement

Mechanical tolerances limit the ability to accurately place antenna elements in their desired location and can perturb the array manifold. This uncertainty in sensor placement is best described with a perturbation in the delay from radiator m to element n as

$$Y_n(f) = \sum_{q=1}^{Q} e^{-j\omega_0 \Delta_n} e^{-j\mathbf{k}^T \mathbf{p}_n} X_q + V_n. \tag{3.36}$$

where Δ_n represents the location perturbation for the nth sensor from the ideal position. Unlike gain/phase mismatch, sensor position uncertainty is unique for each mn combination and cannot be represented by a diagonal matrix. Rather a delta position matrix will have

the same dimensionality as $\mathbf{A}$ and can be integrated using a Hadamard product

$$\mathbf{S} = (\mathbf{\Delta} \odot \mathbf{A}) \tag{3.37}$$

where $\mathbf{\Delta}$ is the sensor position uncertainty matrix.

3.1.1.4 Array Manifold Perturbation Model

Taking into account the effects of gain/phase mismatch, sensor position uncertainty, and mutual coupling, the full array manifold perturbation model [20] can be written as

$$\mathbf{S} = \mathbf{C\Gamma}(\mathbf{\Delta} \odot \mathbf{A}). \tag{3.38}$$

Examining (3.38) under ideal conditions, one sees that both $\mathbf{C}$ and $\mathbf{\Gamma}$ reduce to $N \times N$ identity matrices, $\mathbf{\Delta}$ becomes an $N \times M$ matrix with every entry equal to unity, and the true array manifold, $\mathbf{S}$ simplifies to the ideal array manifold, $\mathbf{A}$. It is also worth noting that if the sensor position tolerances can be controlled adequately and $\mathbf{\Delta}$ neglected, then the $N \times N$ matrix combination of $\mathbf{C}$ and $\mathbf{\Gamma}$ represents a calibration matrix that relates the true and ideal array manifolds as

$$\mathbf{D} = \mathbf{C\Gamma} \tag{3.39}$$

so

$$\mathbf{S} = \mathbf{DA}. \tag{3.40}$$

3.1.2 Array Calibration

Many modern radar and communication systems rely on an array of elements to radiate and collect electromagnetic energy. Often these systems include some "down stream" signal processing that depends on accurate knowledge of the array's structure which is captured in a set of steering vectors known as the array manifold. These steering vectors can be directly

measured but are often derived from a presumed array model. However, if the true array manifold deviates from the assumed model the performance of any subsequent signal processing can be degraded. This deviation can be due to the affects of mutual coupling, channel gain/phase mismatch, and array element placement uncertainty. Array calibration attempts to measure these effects and bring the array's true and assumed responses into alignment. In a broad sense calibration processes can be broken into two categories, traditional methods that use a set of known sources in known locations and blind calibration methods that use sources in unknown locations. Traditional methods were typically developed for use in benign environments where the number, strength and location of the calibration sources can be controlled. On the other hand, blind calibration methods were generally developed to be used in the field making use of "sources of opportunity". Before we introduce the RACE calibration methods we will take a look at some common calibration techniques from each categories to better appreciate RACE's unique features.

3.1.2.1 Off-line Calibration

Traditional methods of calibration generally determine the array's response by applying a known signal to the array and measuring the response of each array element. This can be done by individually illuminating the elements [43, 44, 45] or by illuminating the entire array simultaneously [46, 47, 48]. There is also a diverse set of methods for measuring element placement tolerances. Classic examples include leveraging the narrow-band assumption and examining the phase at each sensor location [49], taking advantage of the signal subspace structure of a sample covariance matrix [50, 51] and statistically estimating locations from near [52] and far-field sources [53]. Attempts have been made to derive mutual coupling from direct measurements of S-parameters [54] with limited success, while signal processing methods have also been applied that leverage the structure of a sample covariance matrix [51, 20, 30, 31] and searching over a constrained array manifold uncertainty bound [15, 17]. In many cases array calibration is performed once at the beginning of a system's lifetime,

though as a system ages the need arises to recalibrate the array periodically.

3.1.2.2 Blind-Calibration

Calibrating an array with known sources is practical for the initial calibration at the beginning of a system's lifetime, but is impractical once a system is deployed. This limitation led to the development of calibration methods using unknown or blind sources. Most blind calibration methods start by estimating the Direction of Arrival (DoA) of a set of unknown sources, then assume the estimated source location is the true source location, and perform a calibration process, updating the estimated array manifold. The process is then repeated until subsequent DoA estimations deviate from each other by only a small value. This iterative blind calibration process intimately links DoA estimation and array calibration.

A search of the literature reveals blind calibration for many of the classic DoA estimators. For the MUSIC estimator, calibration methods leverage the fact that its cost function is minimized only when the true array manifold is projected into the noise subspace [20, 30, 31]. Likewise, calibration methods have also been developed for the ESPRIT algorithm [55, 56, 57] and the Capon beamformer [17, 16].

3.2 RACE Algorithm

At its most basic level, the blind calibration problem is a joint estimation of the array manifold $\mathbf{S}$ and DoA of an unknown number of incident signals. However, to separately estimate all NM values of $\mathbf{S}$ is a very challenging problem. For the sake of tractability, this work leverages the array manifold perturbation model developed in [20] to estimate the structured gain/phase matrix, $\mathbf{\Gamma}$, and mutual coupling matrix, $\mathbf{C}$. This approach greatly reduces the number of unknowns and simplifies the problem considerably. The RACE algorithm proceeds in two steps. First the DoA of the incident signals is estimated by the RISR algorithm using the most current model of $\mathbf{S}$. Then the gain/phase matrix $\mathbf{\Gamma}$ and the mutual

coupling matrix $\mathbf{C}$ are estimated to subsequently update $\mathbf{S}$. The process then repeats until a convergence criteria is met.

While the array perturbation model and the transformation methods developed by Friedlander were intended for a MUSIC based blind calibration routine they can leveraged here for the RISR based method. Friedlander's core assertion was that the MUSIC cost function

$$J(\psi)_{\text{MUSIC}} = \sum_{i=Q+1}^{N} |\mathbf{u}_i^H \mathbf{s}(\psi)|^2 \tag{3.41}$$

is minimized only when $\mathbf{s}(\theta)$ is a true steering vector for the array. Here $\mathbf{u}_k$ represents the eigenvectors of the noise subspace. Substituting (3.39) and (3.40) into (3.41) produces

$$J(\psi)_{\text{MUSIC}} = \sum_{i=Q+1}^{N} |\mathbf{u_i}^H \mathbf{C\Gamma a}(\psi)|^2 \tag{3.42}$$

with unknowns $\mathbf{\Gamma}$ and $\mathbf{C}$ that Friedlander estimated by minimizing the overall cost function. In contrast, the RACE algorithm will estimate the values of $\mathbf{\Gamma}$ and $\mathbf{C}$ from the array observation vector $\mathbf{y}$ and the estimate of the spatial spectrum $\mathbf{x}$ produced by RISR. This estimation will use the manifold perturbation model and transformations in (3.25) and (3.29)–(3.35) developed by Friedlande, but in a slightly different context. With the basic method to estimate both $\mathbf{\Gamma}$ and $\mathbf{C}$ established a full calibration routine can be developed.

A high level system block diagram of the RACE algorithm can be seen in Figure 3.3. $\mathbf{y}$ and an initial array manifold, $\mathbf{S}_0$ serve as inputs to the RISR algorithm, which produces an estimate of $\hat{\mathbf{x}}$. This estimation along with the current estimate of the array manifold act as inputs to the calibration process which produces an updated estimate of the array manifold $\hat{\mathbf{S}}$ that is fed back to the RISR algorithm and the process repeated.

The RISR algorithm has a built in tolerance for model mismatch that is leveraged for the RACE algorithm. The model noise term

$$\mathbf{R}_z = \sigma_z^2 \mathbf{I}_{M\times M} \odot \left(\mathbf{SPS}^H\right), \tag{3.43}$$

along with the noise loading term, help regularize the matrix inversion when calculating the adaptive filter bank $\mathbf{W}$ and suppress spurious peaks. At the start of a calibration cycle, when uncertainty about the array manifold is high, this model noise loading term can be set to large value, to help suppress model mismatched induced spurious signals. Then as the calibration cycle progresses, and the uncertainty about the array manifold decreases, this loading term can be tapered to increase the sensitivity of the DoA estimation. This model noise loading profile effect is accomplished with addition of a model mismatch scaling term $\beta\mathbf{R_z}$ where $0 < \beta < 1$, and (2.29) becomes

$$\mathbf{W} = (\hat{\mathbf{S}}\mathbf{P}\hat{\mathbf{S}}^H + \alpha\mathbf{R} + \beta\mathbf{R}_z)^{-1}\hat{\mathbf{S}}\mathbf{P}. \tag{3.44}$$

A number of model noise loading profiles for β are possible,both in starting/final value of β, and the taper rate as function of the number of calibration cycles. It was however noted by Blunt that values of σ_z^2 less than -30 dB tended to induce false peaks in RISR, so care should be taken in selecting the final value of β [58, p. 336].

The estimation processes for $\mathbf{\Gamma}$ and $\mathbf{C}$ previously outlined estimated each perturbation matrix in isolation. This can be seen by the lack of a mutual coupling matrix in (3.23) and the absence of $\mathbf{\Gamma}$ from (3.28) and (3.31). Real systems however will likely have both perturbations and the RACE algorithm estimates each matrix sequentially while using the most recent estimate of the other perturbation. Thus (3.23) becomes

$$\begin{aligned} \mathbf{y} &= \mathbf{C}\mathbf{\Gamma}(\mathbf{A}\mathbf{x}) + \mathbf{v} \\ &= \mathbf{C}Q_1[\mathbf{A}\mathbf{x}]\boldsymbol{\gamma} + \mathbf{v} \end{aligned} \tag{3.45}$$

while (3.28) and (3.31) become

$$\begin{aligned} \mathbf{y} &= \mathbf{C}(\mathbf{\Gamma A x}) + \mathbf{v} \\ &= Q_{2|3}[\mathbf{\Gamma A x}]\mathbf{c} + \mathbf{v}. \end{aligned} \tag{3.46}$$

In each calibration cycle, RACE estimates $\mathbf{c}$ and $\boldsymbol{\gamma}$ using a least squares methodology, and can then either recombine them with the ideal array manifold $\mathbf{A}$ to produce an estimation of $\mathbf{S}$ or output them separably. For the first iteration of the calibration cycle ideal values of $\mathbf{\Gamma}$ and $\mathbf{C}$ can be used to bootstrap the process. While this is necessary for the efficacy of the RACE calibration process, it also provides an opportunity to incorporate prior estimates of $\mathbf{\Gamma}$ and $\mathbf{C}$ from an independent calibration process.

System architects have more flexibility if prior estimates of the array manifold can be incorporated into the calibration process. For example a system may be calibrated using traditional, non-blind method prior to deployment, but once in the field be unable to tolerate downtime for periodic recalibration. Being able to leverage this prior calibration can potentially improve RACE and help system architects to avoid downtime. There are two distinct ways that prior calibration information can be incorporated into the RACE algorithm, 1) by seeding the calibration process with an estimate of the mutual coupling matrix and gain/phase matrix rather then initializing the algorithm with idealized values or 2) by replacing the ideal array manifold with the prior estimate of the array manifold.

If prior calibration data is available the initial values of $\mathbf{\Gamma}$ and $\mathbf{C}$ can be seeded from the earlier calibration. This starts the routine with a good estimate of both $\mathbf{\Gamma}$ and $\mathbf{C}$ but otherwise does not restrict the final solution. In contrast, prior calibration can be incorporated into RACE by replacing the ideal array manifold $\mathbf{A}$ with the calibrated array manifold. Since the value of $\mathbf{A}$ is not updated by the calibration process this method keeps the calibration process rooted in the solution neighborhood near the prior calibration. This manifold replacement method also transforms $\mathbf{\Gamma}$ and $\mathbf{C}$ into channel gain/phase and mutual

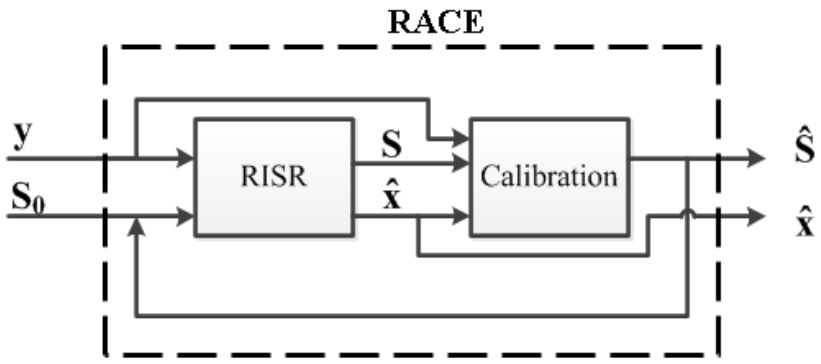

Figure 3.3: RACE Blind Calibration Process Model

coupling perturbation matrices relative to the measured array manifold rather then full estimates of their respective confounding effects.

3.3 RACE Performance

In this section we will evaluate the performance of the RACE algorithm. We will start by showing the performance of the RACE algorithm for a typical scenario before exploring the convergence region of this iterative method. The RACE algorithm is first shown to be robust over a wide range of channel gain variation, and over a smaller range of channel phase variation. We then find that RACE is effective for low SNR if the number of sources is limited, and requires a greater SNR as the number of sources increases. However, there are diminishing returns as RACE struggles when the number of sources is greater than 8 even for very high SNR scenarios. We will also show that the performance of RACE for low SNR can be improved by correctly scaling the RISR model mismatch loading term. Several model noise loading profiles are considered for the model mismatch loading term. Next, we find that RACE's performance is suppressed for coherent sources as the probability of convergence is reduced significantly. Finally, we evaluate the ability of RACE to integrate prior calibration data by implementing manifold replacement and show that this method can significantly extend RACE's convergence region.

To evaluate the performance of the RACE algorithm an array was constructed in simulation. The array was simulated as a 25 element ULA of half-wavelength dipoles with half-wavelength spacing. Spatial sampling was set to 161 samples, making the array manifold a 25x161 matrix. Mutual coupling between elements was modeled using a dipole mutual coupling model [59, p. 472] while channel gain/phase errors were modeled as normal distributions with independent gain and phase variances.

With the simulated array in place the RISR algorithm was implemented as described in Section 2.1.3 using non-coherent integration. The calibration process was implemented using (3.45) and (3.46). The RISR algorithm was configured to run for 10 iterations while the calibration loop seen in Figure 3.3 was set for 10 cycles. Over the course of those 10 cycles the value of β was decreased from 1 to 0.1 using a linear progression, while α was set to constant value of 1/8. Unless otherwise specified these settings were used to produce the simulation results presented in this section. A testing regimen was then undertaken to quantify the performance of the RACE algorithm. First, typical pre and post calibration spectrums are presented, along with RMS error in $\mathbf{\Gamma}$ and $\mathbf{C}$ as a function of calibration cycles, to show the effect of array perturbations and the improvement that can be made through calibration. Next, the conveyance region of RACE is explored by examining the probability of converging to the correct solution over various ranges of SNR, number of sources and amount of channel gain/phase mismatch. Then, the effect of different tapper profiles is explored as the effect of coherent incident sources. Finally, RACE's ability to integrate prior calibration data will be explored by modifying the array model and partially calibrating the array prior to starting RACE.

A typical example of the output spatial spectrum can be seen in Figure 3.4. In the first iteration the array is uncalibrated and three incident signals plus several spurious signals are visible. As the RACE calibration cycle progresses the spurious signals are suppressed and eventually removed entirely. This spurious signal suppression can be seen in Figure 3.5 as the RMS error of the spatial spectrum decreases over the 10 calibration cycles. Where RMS

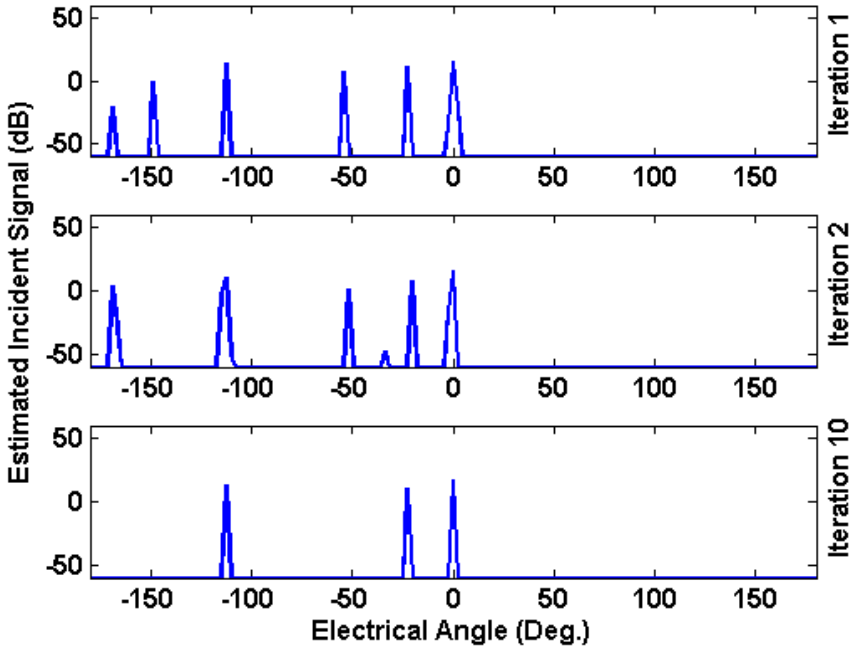

Figure 3.4: RISR spatial spectrum before, during, and after calibration. True signals at $-115.5°$, $-22.5°$ and $0°$

error is defined as

$$\text{RMS Error in } \hat{\mathbf{P}} = \sqrt{\frac{1}{M}\sum_{m=1}^{M}(\hat{\mathbf{P}}-\mathbf{P})^2}. \tag{3.47}$$

A similar reduction in the RMS error of the mutual coupling and channel gain/phase can be seen in Figures 3.6 and 3.7, where the RMS error is calculated using

$$\text{RMS Error in } \hat{\mathbf{c}} = \sqrt{\frac{1}{N}\sum_{n=1}^{N}(\hat{\mathbf{c}}-\mathbf{c})^2}, \tag{3.48}$$

and

$$\text{RMS Error in } \hat{\boldsymbol{\gamma}} = \sqrt{\frac{1}{N}\sum_{n=1}^{N}(\hat{\boldsymbol{\gamma}}-\boldsymbol{\gamma})^2}, \tag{3.49}$$

respectively. While this set of results shows the RACE algorithm converging to a correct solution, it is possible for the algorithm to diverge, and we now turn our attention to the convergence region of RACE.

Since RACE is dependent on the starting DoA estimate of RISR being "close enough"

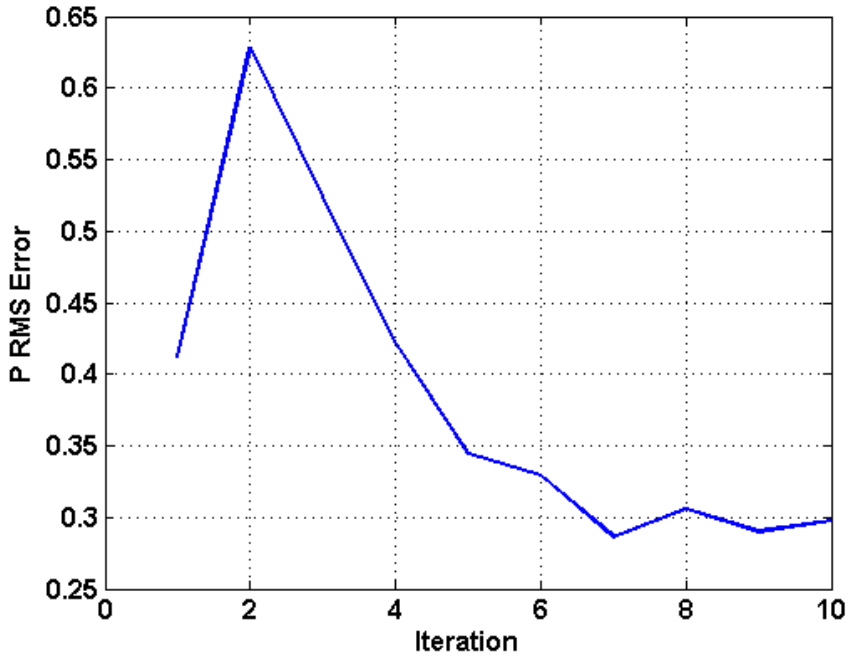

Figure 3.5: RISR spatial spectrum RMS error over calibration cycle

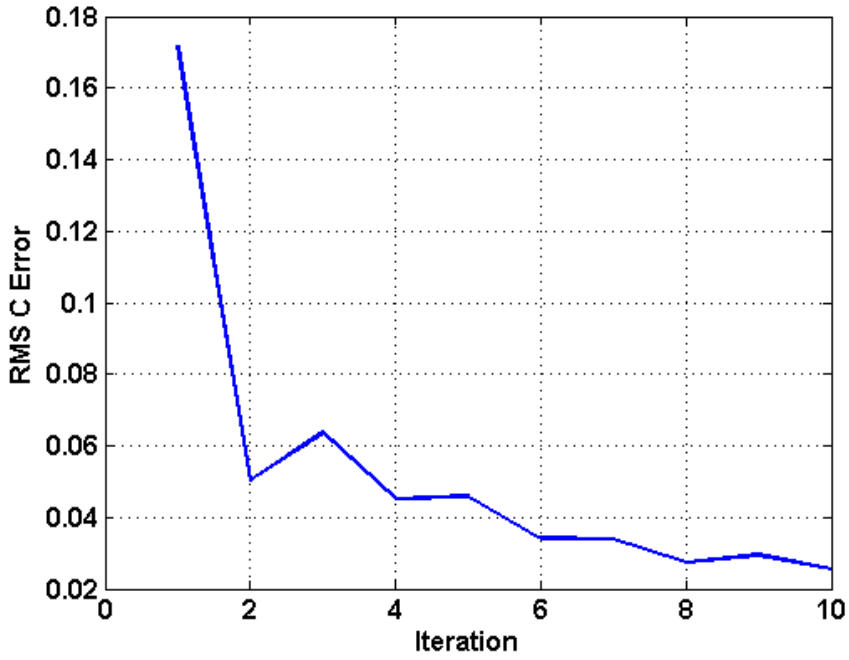

Figure 3.6: Mutual coupling RMS error over calibration cycle

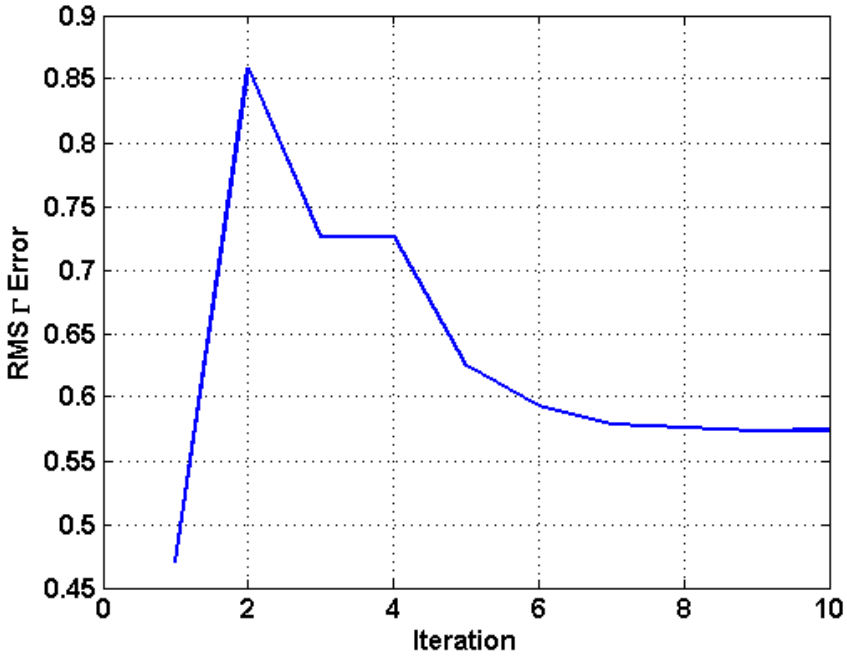

Figure 3.7: Channel gain/phase RMS error over calibration cycle

it is possible for RACE to diverge. To help quantify this convergence region a set of Monte Carlo simulations were undertaken. From these Monte Carlo simulations the probability of convergence could be examined as a function of different variables. It should be noted that convergence is used here in a loose sense, as a simulation is said to be converged if the RMS error in the spatial spectrum estimation is less then 1/3. This value was selected as it was found that below this level spurious signals were almost always suppressed, above it the spurious signals grew rapidly obscuring the true signals. This is in contrast to convergence in the sense that an iterative process has reached a solution and does not deviate from it with additional iterations. This convergence method was used so that the probability of convergence would relate to the probability that RACE reached the correct solution, rather than reaching a fixed, but not necessarily correct solution.

Figures 3.8 and 3.9 examine the probability of convergence as functions of channel gain and phase standard deviations. As the variations in channel gain and phase directly degrades RISR's ability to estimate the DoA of incident signals excessive variation can push the

calibration routine out of the convergence region. In both plots, three signals are incident upon the array, with a Signal to Noise Ratio (SNR) of 20 dB. The signals are uncorrelated and placed at an independent random incident angle for each of the 1000 Monte Carlo trials. Figure 3.8 plots the of probability of convergence as the standard deviation of channel gain increases, and includes example curves for various channel phase deviations. Predictably as the channel gain mismatch increases, the probability of convergence rolls off. This roll off appears linear on this scale with all traces converging to zero near a value of 1.6 dB with the amount of phase variation determining the slope and y-axis intercept points. Figure 3.9 presents a different cut of the data where the probability of convergence is plotted against increasing channel phase deviation. It appears that the probability of convergence slowly declines until around 15° after which it rapidly declines to less then a one in five chance of convergence above 20°. Taking the plots together it appears that RACE is more sensitive to channel phase variation as we see a rapid drop off in convergence once the phase standard deviations exceeds 15°. In practice it is much more challenging to construct systems with small channel phase deviation than small channel gain variations. This is an area where integrating prior calibration data into RACE is beneficial and will be explored in depth later in this section.

The signal to noise ratio of signals incident upon the array will have a strong effect on RISR's DoA estimation performance and Figure 3.10 examines the probability of convergence as a function of SNR. For three or more sources there is a sharp rise in the probability of convergence from -5 dB to 5 dB before the slope of the convergence rate begins to level off and rise much slower. This likely corresponds with SNR region in which RISR's DoA estimates become reliable. The probability of convergence for a single source and for two sources are outliers. There is nearly a unity convergence rate for a single source over the entire SNR range, and this is likely due to the trivial nature of the single source problem. In contrast, the convergence rate for two sources is significantly suppressed compared to the other test cases. It is not evident why the convergence rate for the two source test case rises such

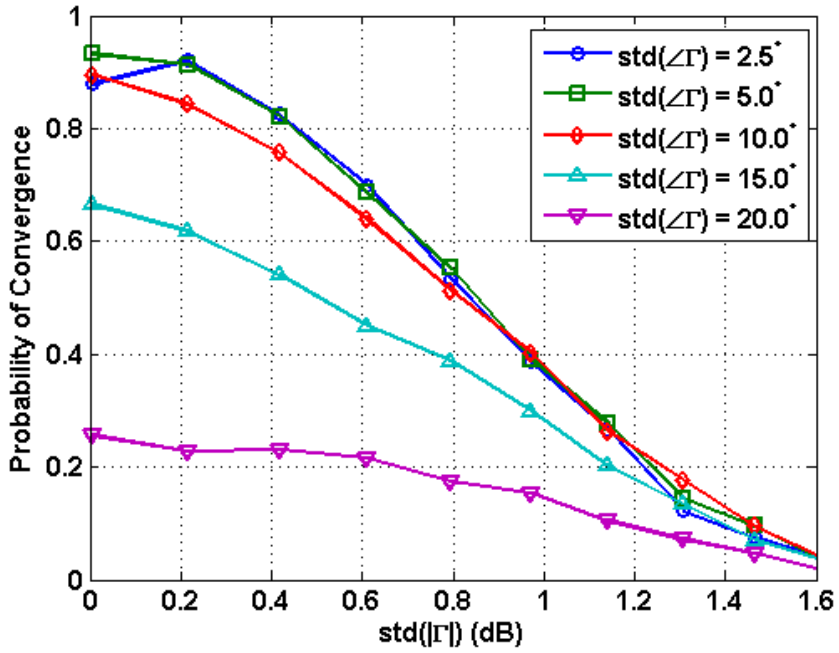

Figure 3.8: RACE convergence vs Γ amplitude variation, $\circ$: std$(\angle\Gamma) = 2.5°$, $\square$: std$(\angle\Gamma) = 5.0°$, $\diamond$: std$(\angle\Gamma) = 10°$, $\triangle$: std$(\angle\Gamma) = 15.0°$, $\triangledown$: std$(\angle\Gamma) = 20.0°$

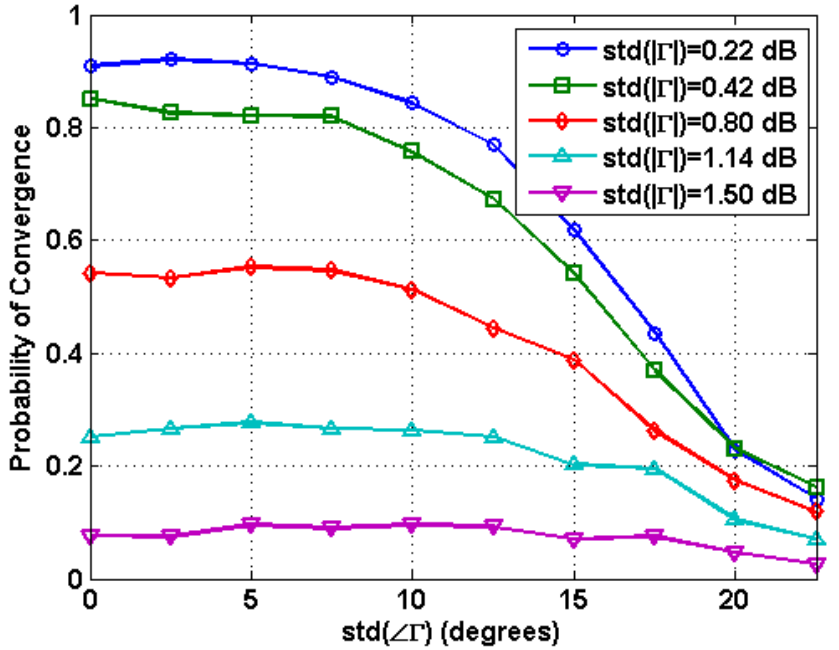

Figure 3.9: RACE convergence vs Γ phase variation, $\circ$: std$(|\Gamma|) = 0.22$dB, $\square$: std$(|\Gamma|) = 0.42$dB, $\diamond$: std$(|\Gamma|) = 0.80$dB, $\triangle$: std$(|\Gamma|) = 1.14$dB, $\triangledown$: std$(|\Gamma|) = 1.50$dB

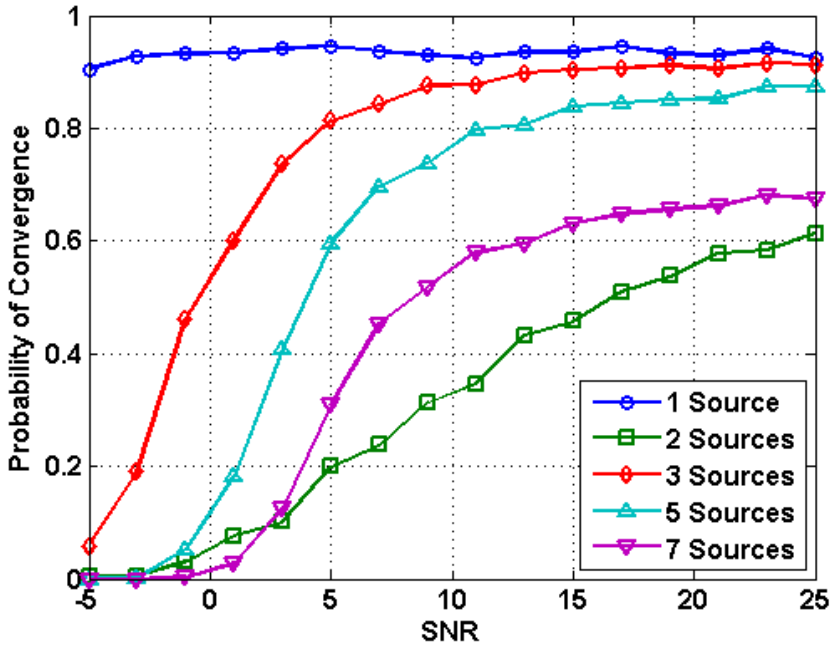

Figure 3.10: RACE convergence vs SNR, ∘ : 1 Source, □ : 2 Sources, ⋄ : 3 Sources, △ : 5 Sources, ▽ : 7 Sources

much slower the then other test cases, but it does appear to be on a trajectory to eventually have a comparable convergence rate as the other test case, just at a significantly higher SNR. This trend can also be seen in Figure 3.11 which plots the probability of convergence verse the number of incident signals. The anomaly for two sources is evident in a large dip in the convergence probability for all SNR traces. Beyond two sources it appears the RACE algorithm degrades gracefully with a slow roll off in the convergence probability as the number of sources grow large.

The role of β profiles on convergence rates was also investigated. Six different profiles were created and can be seen in Figure 3.12. Three profiles are constant value around the top, middle and bottom of the possible values. The remaining three taper in value using a linear, logarithmic and sinusoidal progression. The affect of the different loading profiles can be seen in Figure 3.13 where the probability of convergence is plotted verse SNR for all six profiles. This plot was created from the results of a 500 trial Monte Carlo simulation that used three randomly located, non-coherent sources. The constant $\beta = 0.1$ profile has

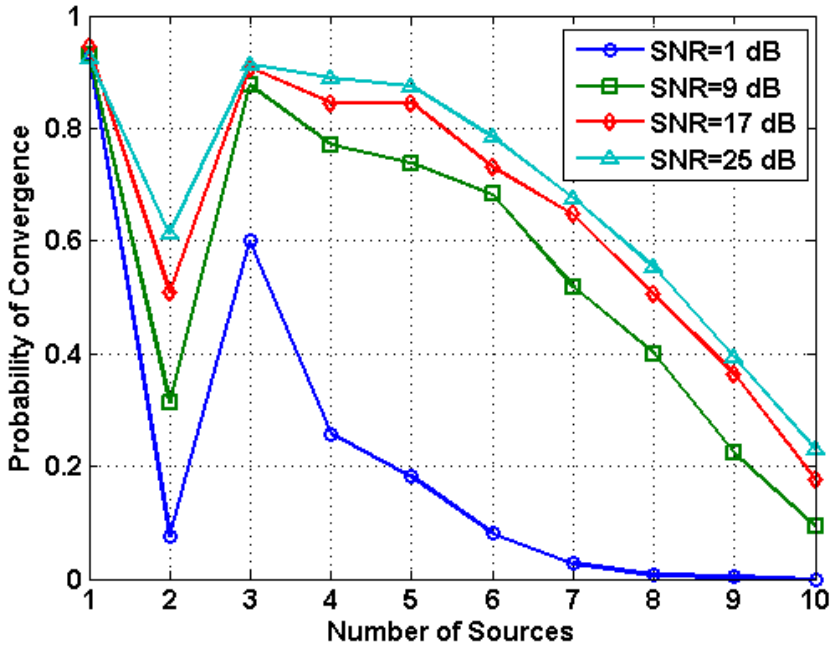

Figure 3.11: RACE convergence vs number of sources,$\circ$: 1 dB SNR, $\square$: 9 dB SNR, $\diamond$: 17 dB SNR, $\triangle$: 25 dB SNR

the poorest performance, presumable because RISR is over estimating its knowledge of the array manifold. Interestingly though all three of the dynamic β profiles only perform slightly better, with around a 10% improvement in convergence probability. Surprisingly, the best performing profiles were the constant $\beta = 0.5$ and $\beta = 1$, with drastically higher convergence rates for low SNR regimens and equal convergence rates at high SNR. This is counter intuitive and suggests that perhaps the regularization that $\mathbf{R}$ and $\mathbf{R_z}$ are providing is too small late in the calibration cycle. We may see better loading performance if the final value of β was increased to around 0.5.

Thus far we have only considered non-coherent sources, but RACE's performance in the face of coherent sources was also evaluated. Figure 3.14 plots the probability of convergence verse channel gain variation while Figure 3.15 depicts the convergence rate vs phase variation. These plots uses the same Monte Carlo set up as Figure 3.8 and 3.9 with the coherent sources replacing the three non-coherent sources. Comparing the figures it evident that the convergence rate is significantly suppressed even for small values of channel gain and

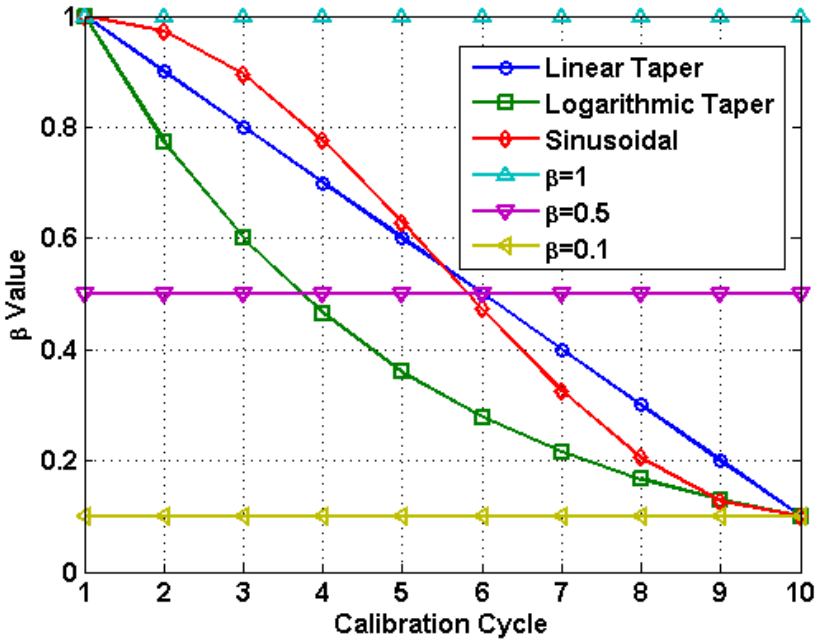

Figure 3.12: Model noise loading profiles, $\circ$: Linear, $\square$: Logarithmic, $\diamond$: Sinusoid, $\triangle$: Constant $\beta = 1$, $\triangledown$: Constant $\beta = 0.5$, $\triangleleft$: Constant $\beta = 0.1$

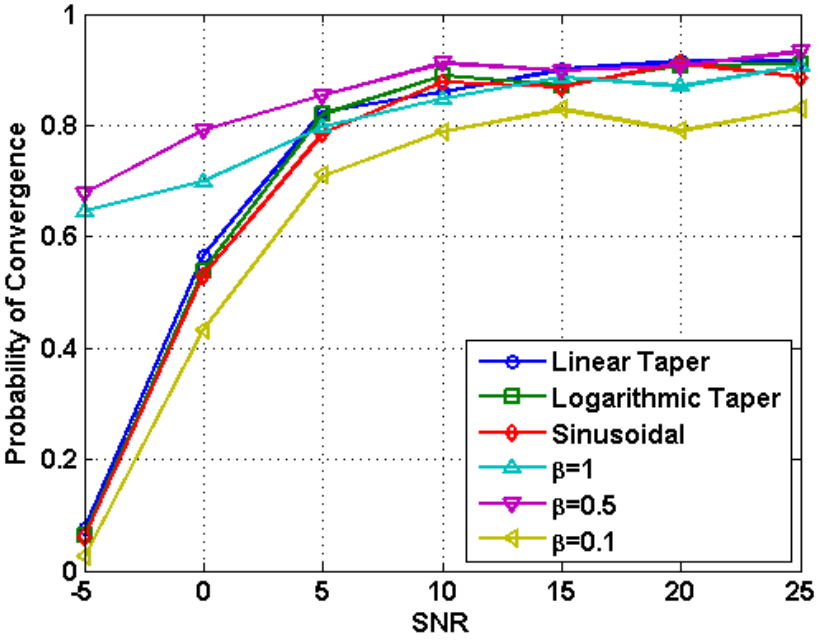

Figure 3.13: RACE convergence vs SNR for three sources, $\circ$: Linear, $\square$: Logarithmic, $\diamond$: Sinusoid, $\triangle$: Constant $\beta = 1$, $\triangledown$: Constant $\beta = 0.5$, $\triangleleft$: Constant $\beta = 0.1$

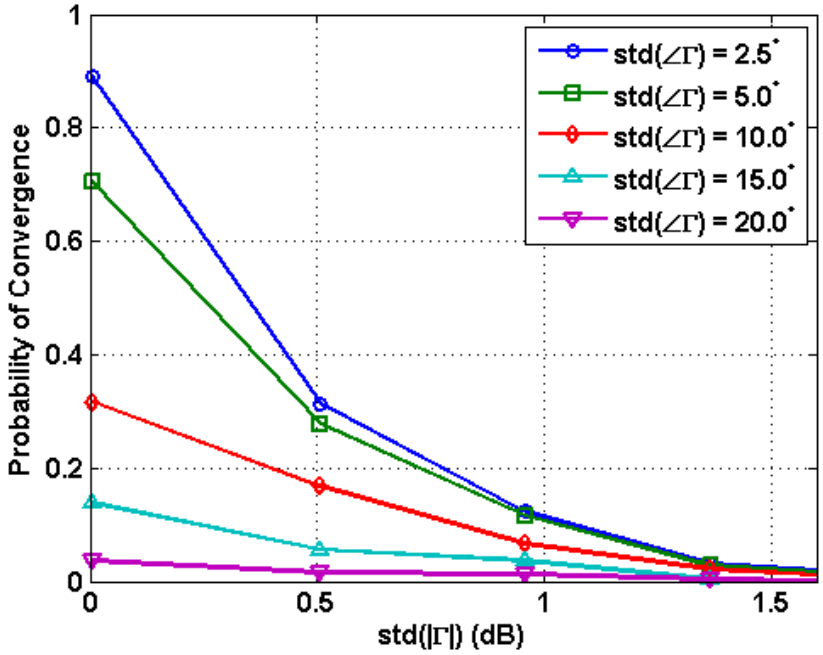

Figure 3.14: RACE convergence vs Γ amplitude variation for coherent sources, ∘ : std$(\angle\Gamma) = 2.5°$, □ : std$(\angle\Gamma) = 5.0°$, ◇ : std$(\angle\Gamma) = 10°$, △ : std$(\angle\Gamma) = 15.0°$, ▽ : std$(\angle\Gamma) = 20.0°$

phase variation. The affect of coherent sources was also examined for various SNR and number of sources. Figure 3.16 plots the convergence rate verse SNR for up to 5 coherent sources and Figure 3.17 shows the corresponding convergences as a function of the number of sources. Overall these plots show a much lower convergence probability that does not appear to approach the non-coherent rate even for high SNR. Since RISR is somewhat robust to coherent sources this reduction in the convergence rate is likely only partially attributable to DoA estimation degradation.

To evaluate the ability of RACE to integrate prior calibration data, $\mathbf{\Gamma}$ and $\mathbf{C}$ were each split into two matrices. One matrix acts as the channel variation and mutual coupling measured as part of a prior calibration, and the other matrix acts as a random perturbation from this prior calibration. In this way the total channel variation and mutual coupling can be controlled independently from the information gleaned from a prior calibration. The prior calibration data was incorporated into RACE using the manifold replacement methods

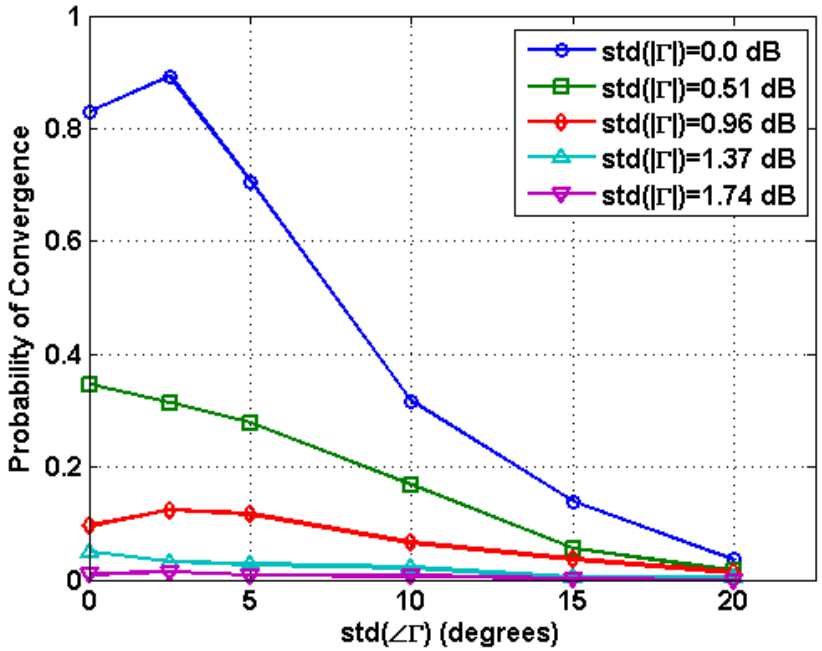

Figure 3.15: RACE convergence vs Γ phase variation for coherent sources, ∘ : std(|Γ|) = 0.0dB, □ : std(|Γ|) = 0.51dB, ⋄ : std(|Γ|) = 0.96dB, △ : std(|Γ|) = 1.37dB, ▽ : std(|Γ|) = 1.74dB

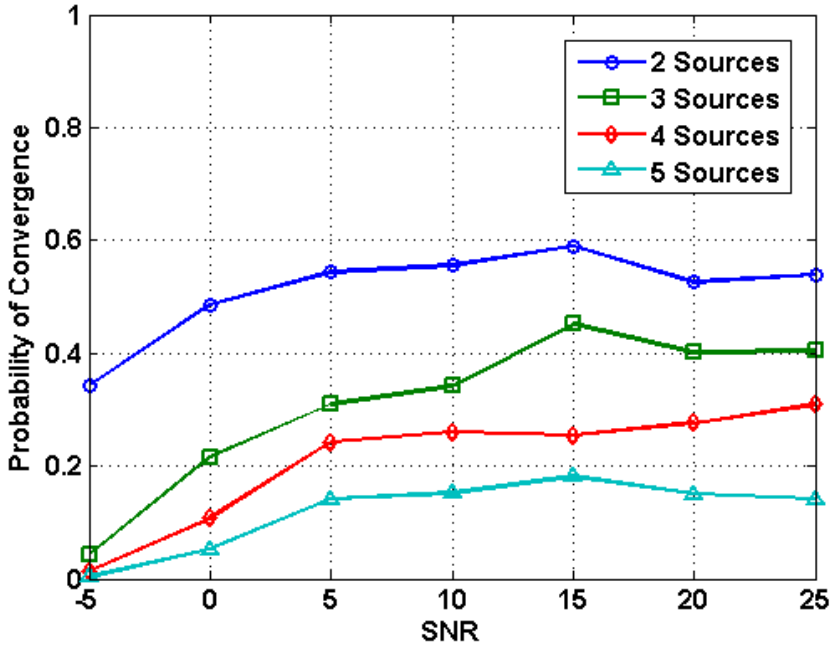

Figure 3.16: RACE convergence vs SNR for coherent sources, ∘ : 2 Sources, □ : 3 Sources, ⋄ : 4 Sources, △ : 5 Sources

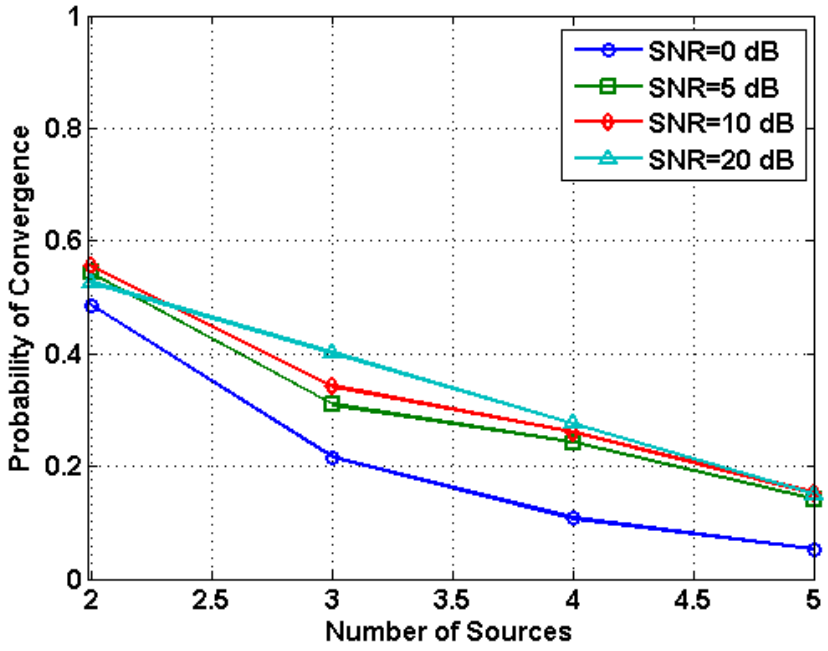

Figure 3.17: RACE convergence vs SNR for coherent sources, ∘ : 0 dB, □ : 5 dB, ⋄ : 10 dB, △ : 20 dB

transforming the array signal model seen in (3.45) into

$$\mathbf{y} = \mathbf{C}\boldsymbol{\Gamma}[\mathbf{C}_p\boldsymbol{\Gamma}_p\mathbf{A}]\mathbf{x} + \mathbf{v}, \tag{3.50}$$

where $\mathbf{C}_p$ and $\boldsymbol{\Gamma}_p$ are the prior estimates of the mutual coupling and channel gain/phase variations respectively. The RACE algorithm now estimates $\mathbf{C}$ and $\boldsymbol{\Gamma}$ as perturbations from these starting values. For these trials the value of $\mathbf{C}_p$ was set to the ideal mutual coupling, $\boldsymbol{\Gamma}_p$ was set to have an amplitude standard deviation of 0.4 dB and a phase standard deviation of 25°, which according to Figures 3.8 and 3.9 would put the probability of convergence around 10%. The values in $\mathbf{C}$ were then set to unity to simulate channel gain/phase drift only. The convergence rate was then evaluated as a function of channel gain and phase variation. Figures 3.18 and 3.19 plot the convergence rate over channel gain and phase fluctuations respectively. We can see that for no additional fluctuation in $\boldsymbol{\Gamma}$ the probability of convergence is around 70%. This implies that while the prior calibration improves RACE's performance,

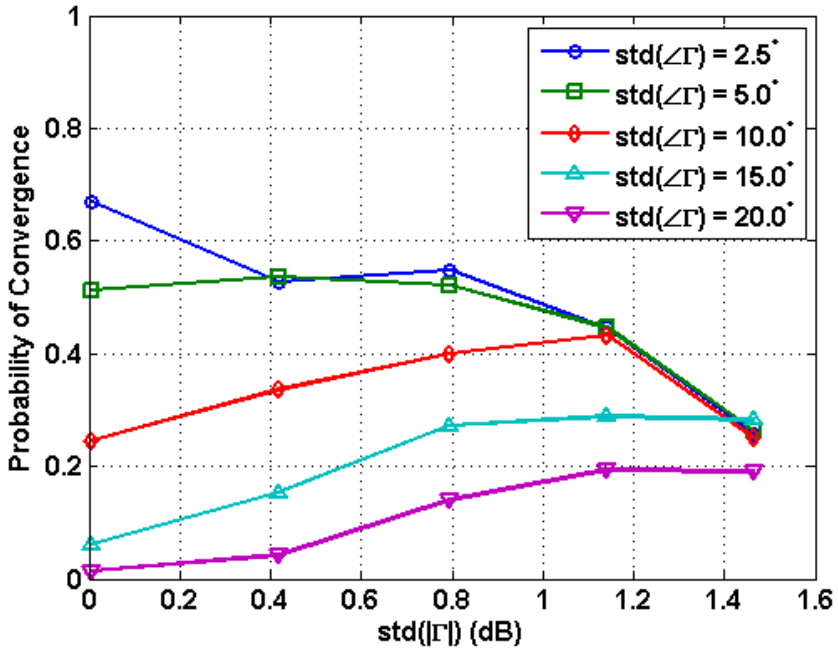

Figure 3.18: RACE convergence vs Γ amplitude variation with prior calibration, ∘ : std$(\angle\Gamma) = 2.5°$, □ : std$(\angle\Gamma) = 5.0°$, ◇ : std$(\angle\Gamma) = 10°$, △ : std$(\angle\Gamma) = 15.0°$, ▽ : std$(\angle\Gamma) = 20.0°$

large fluctuations in channel gain/phase still represent a significant challenge. As the amount of channel fluctuation increase the probability of convergence slowly decrease. The roll off in convergence probability is decidedly faster then in Figure 3.8 and 3.9 underscoring inherent difficulty in calibrating an array with such large channel variations.

3.4 Summary

In this chapter we developed the RISR Array Calibration Enhancement (RACE) algorithm to simultaneously estimate the mutual coupling, channel gain/phase variations and DoA of incident signals. This was accomplished by leveraging the array perturbation model developed by [20] and adapting the estimation techniques presented therein to be used with the RISR algorithm. We showed that RACE is effective at improving the performance of RISR in the presence of model mismatch. The performance of RACE was then evaluated by examining convergence rates as a function of channel gain/phase variation, SNR, and

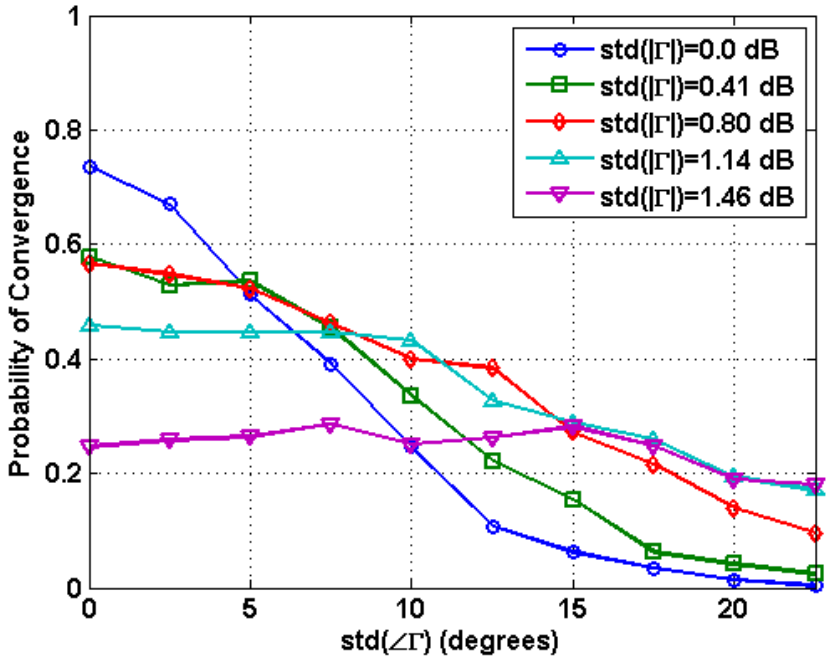

Figure 3.19: RACE convergence vs Γ phase variation with prior calibration, ∘ : std$(|\Gamma|)$ = 0.0dB, □ : std$(|\Gamma|)$ = 0.41dB, ◇ : std$(|\Gamma|)$ = 0.80dB, △ : std$(|\Gamma|)$ = 1.14dB, ▽ : std$(|\Gamma|)$ = 1.46dB

the number of signals. It was shown that RACE is relatively insensitive to channel gain variations, but somewhat sensitive to channel phase variations. We also found that RACE is most effective for three to seven sources, with a greater SNR required as the number of sources increases. In addition different model noise loading profiles were evaluated and it was found that low SNR performance can be improved through model noise loading limit selection. In addition, it was found that convergence rates were significantly suppressed for coherent sources. Finally, the ability for RACE to integrate prior calibration data was demonstrated using the manifold replacement method, and it was shown that integrating prior calibration data in this manner could extend the convergence region of the RACE algorithm.

Chapter 4

Transmit-Receive Model Mismatch

Antenna pattern reciprocity is a fundamental concept that underpins much of antenna theory and design practice. While antenna reciprocity is indisputable for a single antenna in isolation, it is less than definitive when it comes to an array of antenna elements. In this chapter we explore antenna reciprocity first for an antenna in isolation, before expanding to antenna arrays and the effect of mutual coupling. We then examine the design of microwave front-ends to see how the matching characteristics of RF amplifiers propagate through the front-end to load the antenna. We are then able to appreciate how non-reciprocal elements in the microwave front-end place different loads on the antenna depending on the operating mode of the system. This mode dependent loading in effect changes the electrical configuration of the array and produces different mutual coupling for a transmitting array than for a receive array, which in turn produces a nonreciprocal radiation pattern. This analysis approach is unique in that takes into account the hardware in the front-end of a transceiver. This is in contrast to existing literature that simplifies this hardware down to a single Thévenin model, which masks this mode dependent loading, and ultimately the non-reciprocity.

The concept of pattern reciprocity is instilled in many young antenna engineers so vehemently that it is never challenged. This can be detrimental when implementing adaptive

array processing algorithms that depend on accurate knowledge of the array's characteristics. In the following sections of this chapter we explore the performance degradation of direction of arrival estimators when the transmit array manifold is mistakingly substituted for the receive array manifold. The impact of this manifold mismatch is measured in terms of RMS error in DoA estimates and a reduction of the probability of resolving two closely spaced targets. We find that the MUSIC algorithm is adversely impacted by transmit-for-receive array substitution in both of these metrics. On the other hand, RISR shows little to no performance degradation due to its build in tolerance for model mismatch. We will present results for both a uniform linear array of dipoles and a conformal array of dipoles suspended above a PEC cylinder. We start in Section 4.1 by surveying existing literature on mutual impedance, mutual coupling models, as well as, the role front-end hardware plays in modeling mutual coupling. Section 4.2 then develops a mutual coupling model that integrates the effects of mode dependent antenna loading. We then present the impact of transmit-for-receive manifold on MUSIC and RISR for a ULA and a conformal array of dipoles in Section 4.3. This is then followed by a discussion of the results in Section 4.4 and a summary of our findings in Section 4.5.

4.1 Background

Before the impact of transmit-receive manifold model mismatch can be examined, we need to understand the underlying cause of the mismatch. In Section 4.1.1 we formally define antenna reciprocity and note some special exceptions. Section 4.1.2 explores antenna arrays and delves into competing mutual coupling models. The mutual impedance for ULA and conformal array of dipoles are developed in Section 4.1.3. Finally Section 4.1.4 considers the effect microwave front-end hardware have on array mutual coupling, and brings together an explanation for model mismatch.

4.1.1 Antenna Reciprocity

The reciprocity between a transmitting antenna's pattern and the same antenna's receive pattern is a fundamental assumption in antenna theory. Many texts introduce the concept of reciprocity in antennas by analogy to circuit theory by including a statement to the effect of, "in linear, bilateral networks the location of a voltage source and a voltage meter can be interchanged without changing the meter's reading," [59, p. 144–150][60, p. 8, 405–409][61, p. 666–668]. This analogy is acceptable at face value as most antennas are constructed out of simple materials and the propagation media between them is composed of linear, bilateral materials. A few exceptions are highlighted though, Ramo points out that ionosphere propagation is not strictly bilateral and Stutzman notes the presence of non-reciprocal components such as ferrite isolators in the antenna system will cause reciprocity to not hold. The reciprocal circuit analogy also lends itself to describing the interaction of two antennas using impedance parameters [62, p.1701–174] and leads to the equivalent impedance network seen in Figure 4.1. The impedance parameters Z_{11} and Z_{22} represent the self impedance of two antennas and $Z_{21} = Z_{12}$ is the mutual impedance between the two antennas. The mutual impedance is a function of the relative position of the two antennas, the intervening media, as well as, the antennas' radiation characteristics. This definition of antenna pattern reciprocity is established for a single antenna in isolation. It is so fundamental that it is almost universally applied even when an antenna is not in isolation, such as when an antenna is part of a larger array of antennas and subject to mutual coupling.

4.1.2 Mutual Coupling

In the most general sense, mutual coupling is a description of the interactions between two or more closely spaced antennas. These antenna elements are typically working in unison to radiate a signal to a distant target, and mutual coupling perturbs the antenna elements from the performance they would exhibit in isolation. A more precise definition of mutual coupling is a little more elusive as divergent definitions of mutual coupling have evolved

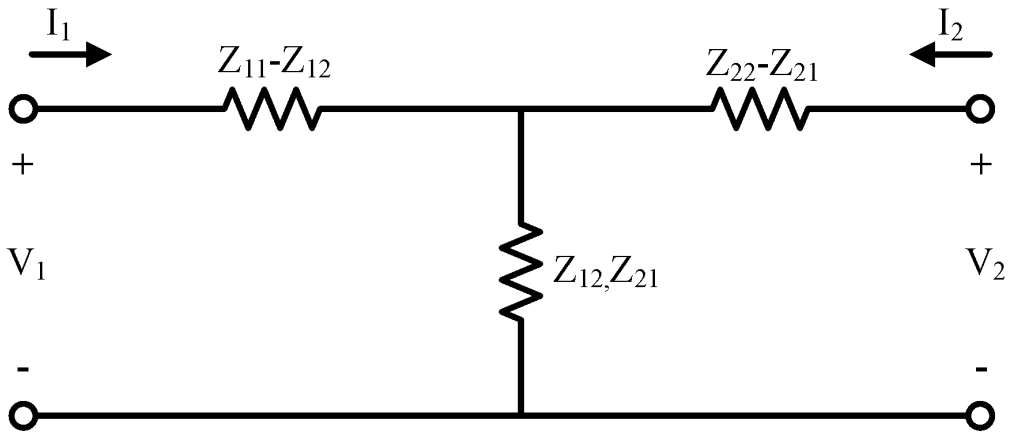

Figure 4.1: Two-port antenna impedance circuit model

and established significant bodies of work [63]. There are two major subject areas that are driving this divergence, the first is the definition of mutual impedance and the second is how to define mutual coupling once a definition of mutual impedance is selected. There are other nuanced differences but mutual impedance and the mutual coupling definition are strong driving factors. The predominate model, often referred to as the open-circuit model, relates the open-circuit voltage that would have been present in an antenna in isolation to the voltage that appears when the antenna is in proximity to other array elements [64]. This first order approximation accounts for the voltage induced across an antenna's terminals as a result of the direct coupling of nearby elements. It only accounts for the primary fields induced by each element and not any scattering effects. Many of the the competing mutual couping models attempt to address this deficit by examining arrays in different modes or by considering secondary scattered fields. But there is not much consensus on either mutual impedance definitions or array models. For example, within works that consider arrays where every element is being driving by an identical source, [65] defines mutual impedance using open-circuit voltages and supplied current, while [66] uses voltage across the generators source impedance, and further breaks down mutual impedance into direct and indirect effects. In contrast [67] defines mutual impedance for an array in receive mode as the ratio of voltage across one element's load to the induced current from a second element, making mutual

impedance dependent on the load impedance. Newer MIMO works break mutual impedance down into array structure impedance and near-field scattering [4].

There is also little consonance on mutual coupling models, as many works have competing mutual coupling matrices that attempt to quantify the effect of mutual coupling on an array signal model. Works that leverage the open-circuit mutual impedance often uses a mutual coupling matrix that makes use of only the mutual impedance and load impedance of the antenna elements. Svantesson, in contrast, forms a mutual coupling matrix using, mutual impedance, antenna impedance, and test equipment impedances [68]. Many authors, particularly in the adaptive array algorithm community, forgo a physical definition of mutual impedance entirely when forming a mutual coupling matrix and assume the final matrix must be Toeplitz [9, 20, 69, 70]. Both the open-circuit mutual coupling model as well as some of the competing models are examined in detail before a model is selected for this work.

4.1.2.1 Open-Circuit Mutual Coupling Model

The open-circuit model of mutual coupling leverages the self and mutual impedances of closely spaced array elements to relate the open circuit voltage across each element in isolation to the voltage across each element as a member of the array [64]. The self and mutual impedances between two antennas is defined using the circuit model in Figure 4.1, from which the voltage at each port can be written as

$$\begin{aligned} V_1 &= Z_{11} I_1 + Z_{12} I_2 \\ V_2 &= Z_{21} I_1 + Z_{22} I_2. \end{aligned} \tag{4.1}$$

The impedance terms are then defined as the ratio between the open-circuit voltage at terminal 2 divided by the current supplied by terminal 1

$$Z_{21} = \left. \frac{V_2}{I_1} \right|_{I_2=0} \tag{4.2}$$

The open-circuit mutual coupling model considers an N element array excited by a distant source, as seen in Figure 4.2, and assumes that the voltage at each antenna terminal is the sum of contributions from each array element and the distant source,

$$\begin{aligned} V_1 &= Z_{11}I_1 + Z_{12}I_2 + \cdots + Z_{1N}I_N + Z_{1s}I_s \\ V_2 &= Z_{21}I_1 + Z_{22}I_2 + \cdots + Z_{2N}I_N + Z_{2s}I_s \\ &\vdots \\ V_N &= Z_{N1}I_1 + Z_{N2}I_2 + \cdots + Z_{NN}I_N + Z_{Ns}I_s \end{aligned} \tag{4.3}$$

where V_i and I_i, $i = 1, 2, \ldots, N$ are the voltage and current at the ith terminal, Z_{is} is the mutual impedance between the ith array element and the distance source, and I_s is the source current. Noting that the terminal voltage is

$$V_i = -Z_L I_i \qquad \text{for } i = 1, 2, \ldots, N \tag{4.4}$$

and the open circuit voltage

$$V_i^o = Z_{is} I_s \qquad \text{for } i = 1, 2, \ldots, N \tag{4.5}$$

can be used to recast 4.3 as

$$\begin{bmatrix} V_1^o \\ V_2^o \\ \vdots \\ V_N^o \end{bmatrix} = \begin{bmatrix} 1 + \frac{Z_{11}}{Z_L} & \frac{Z_{12}}{Z_L} & \cdots & \frac{Z_{1N}}{Z_L} \\ \frac{Z_{21}}{Z_L} & 1 + \frac{Z_{22}}{Z_L} & \cdots & \frac{Z_{2N}}{Z_L} \\ \vdots & \vdots & \ddots & \vdots \\ \frac{Z_{N1}}{Z_L} & \frac{Z_{N2}}{Z_L} & \cdots & 1 + \frac{Z_{NN}}{Z_L} \end{bmatrix} \begin{bmatrix} V_1 \\ V_2 \\ \vdots \\ V_N \end{bmatrix}. \tag{4.6}$$

Or more simply

$$\mathbf{V}_o = \mathbf{Z}_0 \mathbf{V}. \tag{4.7}$$

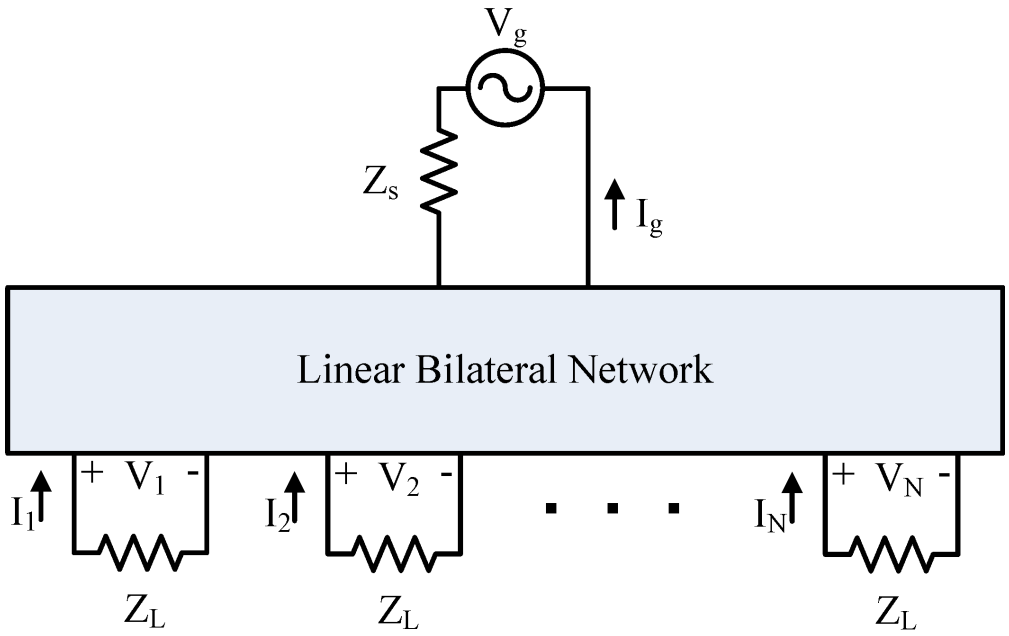

Figure 4.2: Open-circuit mutual coupling model

where $\mathbf{V_o}$ is a vector of the open circuit voltages, $\mathbf{V}$ is a vector of terminal voltages and $\mathbf{Z}_0$ is the impedance matrix relating them. This formulation allows one to take the measured terminal voltages and transform them into the mutual coupling free open-circuit voltages.

4.1.2.2 Alternative Models

The open-circuit mutual coupling model is an improvement over a model that neglects mutual coupling entirely, but it is not a perfect model and some alternative definitions of mutual coupling have been developed. One common critique of the open-circuit mutual coupling model is the manner in which the mutual impedance terms are derived. The impedance terms Z_{ij} are commonly derived assuming either idealized current distributions or current distributions from transmitting antennas [59, p. 471]. These current distribution assumptions are contradictory to the array receive model seen in Figure 4.2. Alternative models typically seek to remedy this contradiction by either using a transmitting array model, or redefining the mutual impedance terms to reflect current distributions imparted by incident plain waves. Another common criticism of the open-circuit mutual coupling model is that it

only accounts for direct coupling from each element and fails to account for scattering from paths that include more than one element. While there is a significant body of work built upon mutual coupling models that seek to remedy the short comings of the open-circuit model we examine only two in detail. Each work is a good representation of the division in mutual coupling models, and are excellent works in their own right.

The first alternative mutual model coupling considered herein addresses the mismatched assumption of the open-circuit model by retaining the transmitting mutual impedance terms and reexamining the array in a transmitting mode [66]. This modification can be seen in Figure 4.3, and Equation (4.3) becomes

$$\begin{bmatrix} V_{g1} - Z_L I_1 \\ V_{g2} - Z_L I_2 \\ \vdots \\ V_{gN} - Z_L I_N \end{bmatrix} = \begin{bmatrix} Z_{11} & Z_{12} & \cdots & Z_{1N} \\ Z_{21} & Z_{22} & \cdots & Z_{2N} \\ \vdots & \vdots & \ddots & \vdots \\ Z_{N1} & Z_{N2} & \cdots & Z_{NN} \end{bmatrix} \begin{bmatrix} I_1 \\ I_2 \\ \vdots \\ I_N \end{bmatrix}. \tag{4.8}$$

The general transmitting problem is to use voltage generators V_{gi} to produce a desired voltage V_i at the antenna terminals but mutual coupling will vary the voltage drop across Z_L. By substituting $V_i' = Z_L I_i$ into (4.8) and performing some manipulation one can arrive at

$$\begin{bmatrix} V_{g1} \\ V_{g2} \\ \vdots \\ V_{gN} \end{bmatrix} = \begin{bmatrix} 1 + \frac{Z_{11}}{Z_L} & \frac{Z_{12}}{Z_L} & \cdots & \frac{Z_{1N}}{Z_L} \\ \frac{Z_{21}}{Z_L} & 1 + \frac{Z_{22}}{Z_L} & \cdots & \frac{Z_{2N}}{Z_L} \\ \vdots & \vdots & \ddots & \vdots \\ \frac{Z_{N1}}{Z_L} & \frac{Z_{N2}}{Z_L} & \cdots & 1 + \frac{Z_{NN}}{Z_L} \end{bmatrix} \begin{bmatrix} V_1' \\ V_2' \\ \vdots \\ V_N' \end{bmatrix}, \tag{4.9}$$

which can be used to relate the generator voltages to the antenna terminal voltages. The impedance matrix in (4.9) is identical to the one that appears in (4.6), which is not surprising as both models use identical definitions of mutual impedance. This has the additional advantage that the same impedance transformation matrix can be used to find the relevant voltages in both the transmit and receive cases.

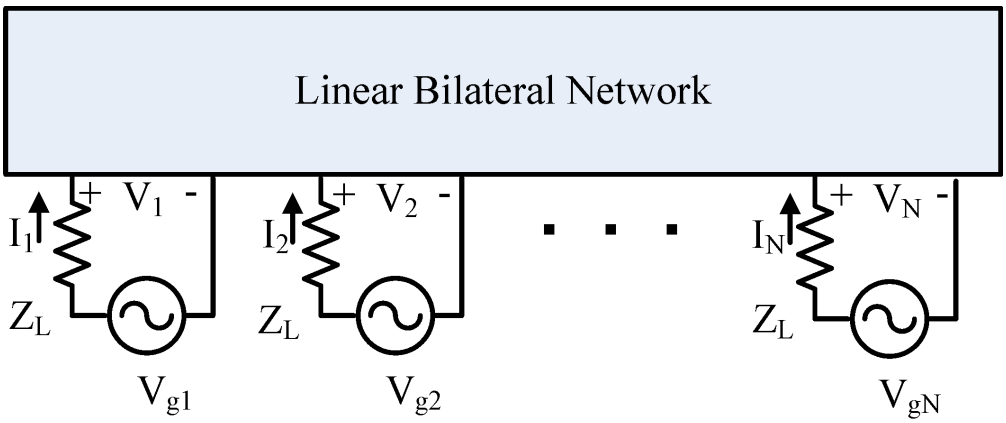

Figure 4.3: Modified open-circuit mutual coupling model

Where Sato deviates from the open-circuit mutual coupling model is by including scattering effects from the other array elements. This starts with the assertion that the current at each antenna element the sum of a radiation current $I_i^{(t)}$ and a re-radiating current $I_i^{(s)}$, such at that

$$I_i = I_i^{(t)} + I_i^{(s)}. \tag{4.10}$$

Substituting (4.10) into (4.8) produces

$$\begin{bmatrix} V_{g1} - Z_L(I_1^{(t)} + I_1^{(s)}) \\ V_{g2} - Z_L(I_2^{(t)} + I_2^{(s)}) \\ \vdots \\ V_{gN} - Z_L(I_N^{(t)} + I_N^{(s)}) \end{bmatrix} = \begin{bmatrix} Z_{11} & Z_{12}^{(t)} & \cdots & Z_{1N}^{(t)} \\ Z_{21}^{(t)} & Z_{22} & \cdots & Z_{2N}^{(t)} \\ \vdots & \vdots & \ddots & \vdots \\ Z_{N1}^{(t)} & Z_{N2}^{(t)} & \cdots & Z_{NN} \end{bmatrix} \begin{bmatrix} I_1^{(t)} \\ I_2^{(t)} \\ \vdots \\ I_N^{(t)} \end{bmatrix} + \begin{bmatrix} Z_{11} & Z_{12}^{(s)} & \cdots & Z_{1N}^{(s)} \\ Z_{21}^{(s)} & Z_{22} & \cdots & Z_{2N}^{(s)} \\ \vdots & \vdots & \ddots & \vdots \\ Z_{N1}^{(s)} & Z_{N2}^{(s)} & \cdots & Z_{NN} \end{bmatrix} \begin{bmatrix} I_1^{(s)} \\ I_2^{(s)} \\ \vdots \\ I_N^{(s)} \end{bmatrix}. \tag{4.11}$$

From this new definition, Sato derives a radiating mutual coupling matrix and a re-radiating mutual coupling matrix. And further asserts that both are needed to describe the transmitting mutual couping while only the re-radiating term is needed to describe receive mutual coupling.

In contrast, works such as [67] seek to improve upon the open-circuit model by using antenna current distributions appropriate for antennas subject to incident plain waves. Hui

also uses a modified definition of the impedance parameter in order to account for secondary scattering between array elements. In contrast to (4.2) where the open-circuit voltage at one antenna terminal is divided by the current supplied by the source antenna, Hui defines mutual coupling using the measured voltages and currents at each terminal induced by the distant source. Using the definitions in Figure 4.2 the mutual impedance is then expressed as

$$Z_{ij} = \frac{V_i}{I_j} \qquad \text{for } i \neq j. \tag{4.12}$$

This new definition of mutual impedance explicitly makes mutual coupling a function of the antenna load as I_j will vary with load impedance. This is in contrast to the open-circuit mutual impedance definition that relates open circuit voltage to supplied source current.

It is evident from these works that modeling mutual coupling is a challenging problem, even from a definition stand point. And one must be careful of the underlying assumptions when applying mutual impedance models to various array geometries.

4.1.3 Array Mutual Coupling Models

With a general understanding of mutual coupling models in place, focus can now turn to selecting a model and applying it to specific array geometries. The work contained herein focuses on applying a open-circuit mutual impedance definition to two different dipole array geometries. The open-circuit mutual impedance model was selected over the alternative definitions for two principal reasons: 1) to leverage some existing bodies of work that make use of the open-circuit assumption and 2) the open-circuit mutual impedance model is sufficiently accurate for the works herein. This work then forgoes using the open-circuit mutual coupling model and instead uses the open-circuit mutual impedance definition to derive a new mutual coupling model. Existing models are derived in terms of total voltages and Thévenin source models which are cumbersome to integrate into a microwave system. The mutual coupling model derived herein will make use of scattering parameters to integrate

the effects of the microwave front-end. Two different dipole arrays are examined in detail. The first is a Uniform Linear Array (ULA) of dipoles and the second is a conformal array of dipoles suspended over a PEC cylinder. The ULA geometry has been extensively studied and the open-circuit mutual coupling model is readily available. The mutual impedances for the conformal array on the other hand will need to be derived. Existing literature will provide several key elements for this derivation. Principally, Herper's work [71, 72] on embedded element patterns can be leveraged to find the dipole active gap impedance and dipole current distribution. These values in turn can be used to model the mutual impedance between array elements.

4.1.3.1 Uniform Linear Array of Dipoles

The derivation of an open-circuit mutual coupling model for dipole antennas in free space is a well studied problem and is available in a number of texts [59, p. 471–473] [60, p. 124–125] [61, 659–661]. Most consider an induced EMF model where

$$Z_{21} = \frac{V_{21}}{I_{1i}} = \frac{-1}{I_{1i}I_{2i}} \int_{-l/2}^{l/2} E_{z21}(z')I_2(z')dz' \tag{4.13}$$

is the mutual impedance between two z directed dipoles of length l, with E-field $E_{z21}(z)$ induced on dipole two by dipole one, the current distribution on dipole two is $I_2(z)$ and I_{1i} and I_{2i} are the input currents on dipole one and two respectively. A closed form solution to (4.13) is obtainable by assuming a sinusoidal current distribution

$$I_z(z) = I_m \sin\left[k\left(\frac{l}{2} - |z|\right)\right] \tag{4.14}$$

and using electric field

$$E_z(z) = -j\frac{\eta_0 I_m}{4\pi}\left[\frac{e^{-jkR_1}}{R_1} + \frac{e^{-jkR_2}}{R_2} - \cos\left(\frac{kl}{2}\right)\frac{e^{-jkr}}{r}\right] \tag{4.15}$$

where R_1, R_2 and r are defined in Figure 4.4, k is the freespace wavenumber, I_m is the maximum current value and η_0 is the freespace impedance. Substituting (4.14) and (4.15) into (4.13) yields

$$Z_{21} = j30\left(\frac{I_{1m}I_{2m}}{I_{1i}I_{2i}}\right)^2 \int_{-l/2}^{l/2} sin\left[k\left(\frac{l}{2}-|z'|\right)\right]\left[\frac{e^{-jkR_1}}{R_1}+\frac{e^{-jkR_2}}{R_2}-\cos\left(\frac{kl}{2}\right)\frac{e^{-jkr}}{r}\right]dz'. \quad (4.16)$$

For side-by-side dipoles separated by distance d a closed form solution exists

$$R_{21} = \frac{\eta}{4\pi}[2\mathrm{C}_i(u_0)-\mathrm{C}_i(u_1)-\mathrm{C}_i(u_2)] \quad (4.17)$$

$$X_{21} = -\frac{\eta}{4\pi}[2\mathrm{S}_i(u_0)-\mathrm{S}_i(u_1)-\mathrm{S}_i(u_2)] \quad (4.18)$$

where R_{21} and X_{21} are the real and imaginary parts of the Z_{21} respectively, and

$$u_0 = kd \quad (4.19)$$

$$u_1 = k\left(\sqrt{d^2+l^2}+l\right) \quad (4.20)$$

$$u_2 = k\left(\sqrt{d^2+l^2}-l\right), \quad (4.21)$$

and $\mathrm{C}_i(x)$ and $\mathrm{S}_i(x)$ are the cosine and sine integrals respectively. This mutual impedance model is suitable for use with either the open-circuit mutual coupling model or the first alternative model considered in Section 4.1.2.2.

4.1.3.2 Cylindrical Conformal Array of Dipoles

Developing an open-circuit mutual coupling model for a conformal array of dipoles above a PEC cylinder is a much more challenging problem. Luckily, some of the key pieces have already been developed and can be leveraged to produce the desired mutual coupling model. Herper developed a theoretical solution for a conformal array of dipoles above a PEC cylinder in [71], and later confirmed his predictions through direct measurement in [72]. Herper was

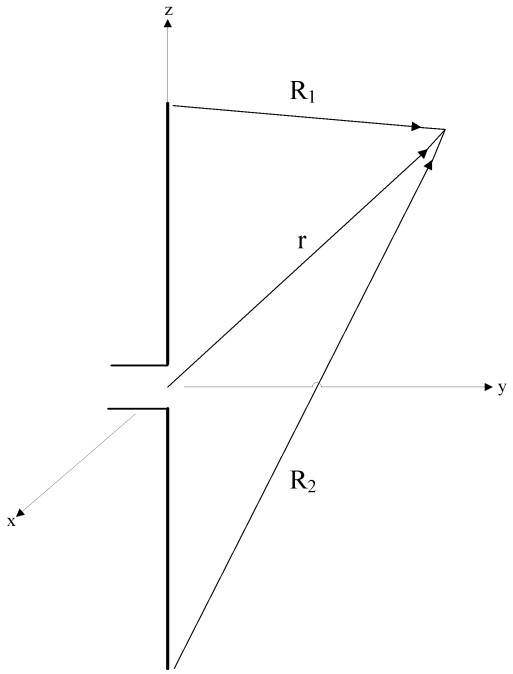

Figure 4.4: Dipole Geometry

principally focused on deriving the embedded element pattern, but in the processes developed the current distribution of each dipole element as well as the active gap impedance. Both of which can be used to help develop a mutual impedance model for the conformal array.

The process Herper follows to derive an embedded element pattern is simple conceptually if rather involved mathematically. It starts by taking the whole array geometry and dividing it into a unit cell containing a section of PEC cylinder and a single dipole element. The appropriate boundary conditions are then applied to the unit cell, including Floquet boundary conditions to account for the periodic nature of the array. A Green's function is then derived for the unit cell based on the geometry and boundary conditions that relates dipole currents to electric field. Herper then assumes a gap voltage is applied to the dipole element that will produce an unknown current distribution on the dipole arms. The Galerkin method is then applied to transform this unknown current distribution into a set of linearly independent equations weighted by a set of unknown coefficients [59, p. 450–458]. This set of equations can be solved using standard linear system theory and the dipole current distribution found. With the dipole current and gap voltage known the dipole active gap impedance

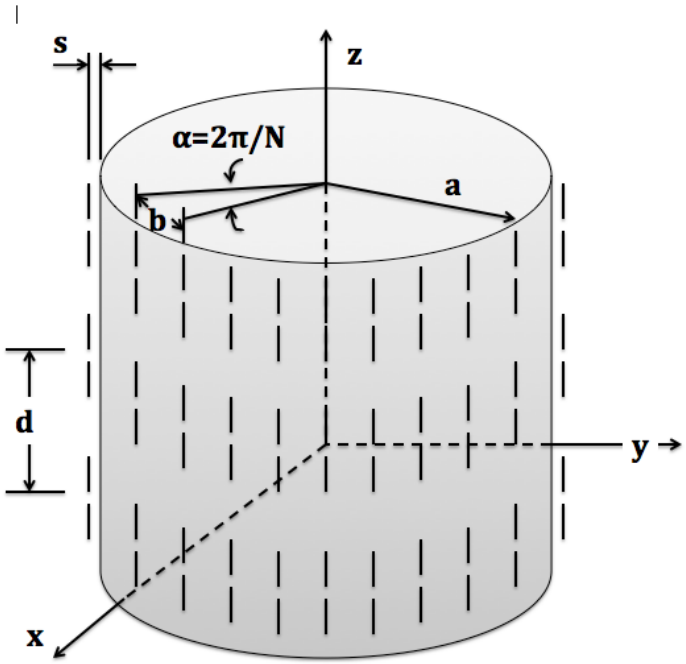

Figure 4.5: Geometry of the cylindrical array

can be found and a matching network designed. The embedded element pattern can then calculated from the dipole current distribution and the Green's function.

Geometry The cylindrical array of dipoles can be seen in Figure 4.5 and the unit cell geometry in Figure 4.6. The array is assumed to be an infinite stack of coaligned circular arrays, each containing N evenly spaced dipoles. Here a is the radius of the PEC cylinder, ρ_0 the radius to the dipole, l and w define the dipole total length and width respectively and h the dipole gap distance. Each unit cell represents a $\alpha = 2\pi/N$ wedge of height d and each dipole is separated by $b \cong \alpha\rho_0$.

Boundary Conditions The unit cell seen in Figure 4.6 has four boundaries to consider. These boundary conditions can be cast in terms of E and H fields or more generally in terms of a Green's function, $G(\mathbf{r},\mathbf{r}')$, where the primed vectors point to the sources and the unprimed to the observation location. On the PEC cylinder tangential E-fields will go to

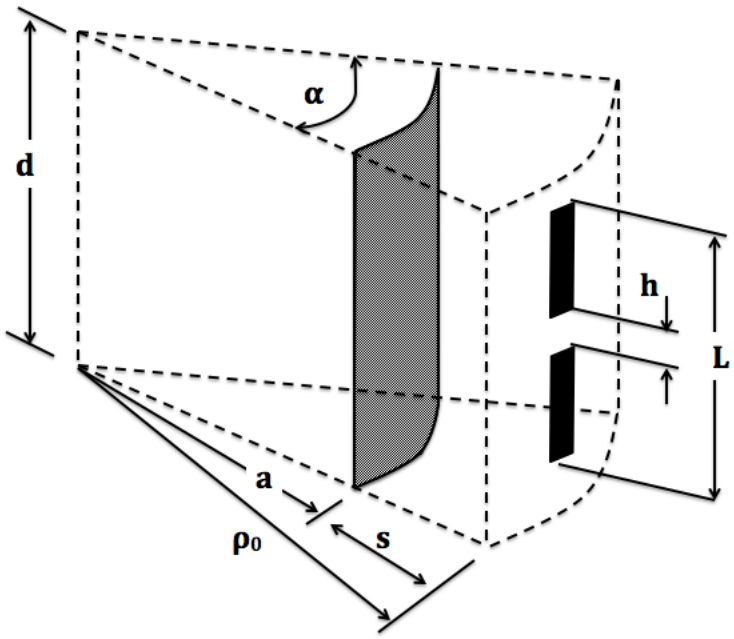

Figure 4.6: Geometry of the unit cell for the cylindrical array

zero [73, p. 343] or in terms of the Green's function

$$G(a,\phi,z;\mathbf{r}')\bullet\mathbf{b}_z = G(a,\phi,z;\mathbf{r}')\bullet\mathbf{b}_\phi = 0 \tag{4.22}$$

In addition, as ρ approaches infinity the Green's function will need to meet the radiation boundary condition. That leaves just the top/bottom and left/right boundary conditions. As the unit cell is placed in an infinite array the Floquet boundary conditions can be applied.

$$G\left(\rho,\frac{\alpha}{2},z\right) = e^{-j\nu\alpha}G\left(\rho,-\frac{\alpha}{2},z\right) \tag{4.23}$$

$$G\left(\rho,\phi,\frac{d}{2}\right) = e^{-jk_{z0}d}G\left(\rho,\phi,-\frac{d}{2}\right) \tag{4.24}$$

Where k_{z0} is the progressive phase delay between neighboring column elements and ν is the νth phase sequence around the circular array. With the boundary conditions defined, the Green's function can now be formulated.

Green's Function In electromagnetics a Green's function is a linear operator that when integrated over a source distribution produces a field quantity. In this case the source is the current distribution over the dipole element and Herper writes the Green's function to produce a auxiliary vector potential **A**. The E and H field quantities can then be found through the differential relationships:

$$\mathbf{H}_A = \frac{1}{\mu} \bigtriangledown \times \mathbf{A} \tag{4.25}$$

and

$$\mathbf{E}_A = -j\omega\mathbf{A} - j\frac{1}{\omega\mu\epsilon} \bigtriangledown \left(\bigtriangledown \bullet \mathbf{A} \right) \tag{4.26}$$

This is a common electromagnetic method that is often employed to solve antenna and radiation problems. Since the dipole length is much greater than its width, $L \gg w$, it can be assumed that the current on the dipole is strictly z-directed and the vector potential can be expressed:

$$\mathbf{A}_z(\mathbf{r};\nu,k_{z0}) = \mu_0 \int_s G(\mathbf{r},\mathbf{r}';\nu,k_{z0})\mathbf{K}(\mathbf{r}')dS' \tag{4.27}$$

Where $\mathbf{K}(\mathbf{r}')$ is the dipole current distribution on surface s.

The form of the Green's function can now be formulated. In addition to the boundary conditions described earlier, the Green's function will also have to satisfy the vector Helmholtz equation:

$$\bigtriangledown^2 G + k^2 G = -\delta(\mathbf{r} - \mathbf{r}') \tag{4.28}$$

It is advantageous to rewrite G in terms of orthogonal functions of ρ, ϕ, and z.

$$G(\mathbf{r},\mathbf{r}') = g(\rho,\rho')\Phi(\phi,z,\phi',z') \tag{4.29}$$

The Floquet boundary conditions in (4.23) and (4.24) can be satisfied solely by Φ

$$\Phi_{mn}(\phi, z) = \frac{1}{\sqrt{\alpha d}} e^{-j(\nu_m \phi + k_{zn} z)} \tag{4.30}$$

where $\nu_m = \nu + mN$, (ν=0, 1, … , N-1; $m = 0, \pm 1, \ldots$) and $k_{zn} = k_{z0} + 2\pi n/d$, ($n = 0, \pm 1, \ldots$). The PEC boundary and radiation boundary conditions can be satisfied by $g(\rho, \rho')$. The Helmholtz equation in (4.28) is first applied to $g_{mn}(\rho, \rho')$ yielding:

$$\frac{1}{\rho}\frac{d}{d\rho}\left(\rho \frac{dg_{mn}}{d\rho}\right) + \left(k_n - \frac{{\nu_m}^2}{\rho}\right) g_{mn} = -\frac{\delta(\rho - \rho')}{\rho} \tag{4.31}$$

where $k_n = \sqrt{k^2 - k_{zn}^2}$. To satisfy the radiation boundary condition g_{mn} will need to take the form of an outward traveling wave. g_{mn} will also need to go to zero at $\rho = a$ to satisfy (4.22). With this and (4.28) in mind, g_{mn} takes the form:

$$g_{mn}(\rho, \rho') = \frac{\pi}{2j} H_{\rho_m}^{(2)}(k_n \rho_>) Z_{z_m}(k_n \rho_<) \tag{4.32}$$

where

$$Z_{\nu_m}(k_n \rho_<) = J_{\nu_m}(k_n \rho_<) - \frac{J_{\nu_m}(k_n a)}{H_{\nu_m}^{(2)}(k_n a)} H_{\nu_m}^{(2)}(k_n \rho_<) \tag{4.33}$$

and $\rho_{>(<)} = \max(\min)(\rho, \rho')$. The Hankel function in (4.32) ensures that the radiation boundary conditions are met while the Z_{ν_m} function does the same for the boundary condition on the PEC cylinder. The complete Green's function can now be written:

$$G(\mathbf{r}, \mathbf{r}'; \nu, k_{z0}) = \sum_{\mathrm{n,m}=-\infty}^{\infty} g_{mn}(\rho, \rho'; \nu, k_{z0}) \Phi_{mn}(\phi, z) \Phi_{mn}^*(\phi', z') \tag{4.34}$$

Galerkin Solution With the Green's function now known, attention can be focused on finding the unknown dipole current distribution. While sinusoidal approximations of half wavelength dipole current distributions are well known [59, p. 460] those distributions are only valid for an isolated dipole current in free-space and is not applicable to a dipole

element within an array suspended over a PEC cylinder. To solve for the unknown current distribution Herper starts by applying a gap voltage, V_g, to the dipole. V_g can be rewritten in terms of an E-field, $V_g = -E_g h$, and since the Green's function in (4.34) can be used to describe the E-field everywhere, including in the dipole gap and on the dipole itself, one can write:

$$\widehat{\mathbf{G}}\mathbf{K} = \int_s \widehat{G}(\mathbf{r},\mathbf{r}')\mathbf{K}(\mathbf{r}')dS' = \begin{cases} 0 & \text{on dipole arms} \\ Eg & \text{in the gap} \end{cases} \tag{4.35}$$

where $\widehat{G}$ is the E-field Green's function found by applying (4.26) to (4.34). Equation (4.35) is still not directly solvable as the integration still involves an unknown distribution $\mathbf{K}$. An approximate solution can be derived by applying Galerkin's method.

Galerkin's method takes the unknown distribution, $\mathbf{K}$, and supposes that it can be written as a series of orthogonal basis functions of unknown weights.

$$\mathbf{K}(\mathbf{r}') = \sum_{q=1}^{Q} c_q \Psi_q(\phi', z') \tag{4.36}$$

Where Q is the number of basis functions used. The orthogonal basis function, Ψ_q, will need to be valid on the dipole. Let $\Psi_q = 0$ for ϕ and z off the dipole, solely a function of z on the dipole, and $\Psi_q(\phi', l/2) = \Psi_q(\phi', -l/2) = 0$. A sine function is a natural choice to meet these conditions.

$$\Psi_q = \sin\frac{q\pi}{l}\left(z + \frac{l}{2}\right) \tag{4.37}$$

It should be noted that as $Q \to \infty$ the Galerkin approximation converges to the true solution. Applying (4.36) to (4.35) yields

$$\sum_{q=1}^{Q} c_q \widehat{\mathbf{G}}\Psi_q(\phi', z') = E_g \mathbf{p_h}\mathbf{p_w} \tag{4.38}$$

where $\mathbf{p_h}\mathbf{p_w}$ are pulse functions with a unity value over the dipole gap. In this form one can see that the Galerkin's method to this point has transformed (4.35) into a form in which the

integration can be evaluated, however it has created Q unknown weights, c_q. Linear system theory dictates that to solve for Q unknowns one needs Q equations. Galerkin's method accomplishes this by taking the inner product of both sides of (4.38) with a set of orthogonal testing functions. In classic Galerkin's method the basis and testing functions are composed of the same orthogonal functions, and the inner products will be non-zero only when the basis and testing functions are equal.

$$\sum_{q=1}^{Q} c_q(\Psi_p, \widehat{\mathbf{G}}\Psi_q) = E_g(\Psi_p, \mathbf{p_h p_w}) \qquad \text{p = 1, 2, ..., P=Q} \tag{4.39}$$

where the inner product $(\mathbf{f}, \mathbf{g})$ is defined over the dipole by

$$(\mathbf{f}, \mathbf{g}) = \int_{-w/2p_0}^{w/2p_0} d\phi \int_{-L/2}^{L/2} f(\phi, z) g(\phi, z) dz \tag{4.40}$$

Galerkin's method has now created Q unknown weights and Q linear equations that can be solved using linear system theory and then used to calculate the dipole currents. Once the currents are known, secondary products such as the active dipole gap impedance can be found. Equation (4.27) can then be used to find the vector potential and Equations (4.25) and (4.26) can be used to find the radiated fields.

Matching Network With the dipole current distribution, $\mathbf{K}$, found and the applied gap voltage, V_g, known, the active dipole gap impedance can be found by evaluating the current distribution over the dipole gap and applying Ohm's law.

$$Z_g = \frac{V_g}{\langle I_g \rangle} = \frac{V_g}{\frac{w}{h}\int_{-h/2}^{h/2} \mathbf{K}(z) dz}. \tag{4.41}$$

Since the active gap impedance is not likely to match the characteristic impedance of the feed transmission line a matching network will be required. A generic 2-port matching network can be seen in Figure 4.7. Network theory can be applied and the gap voltage can

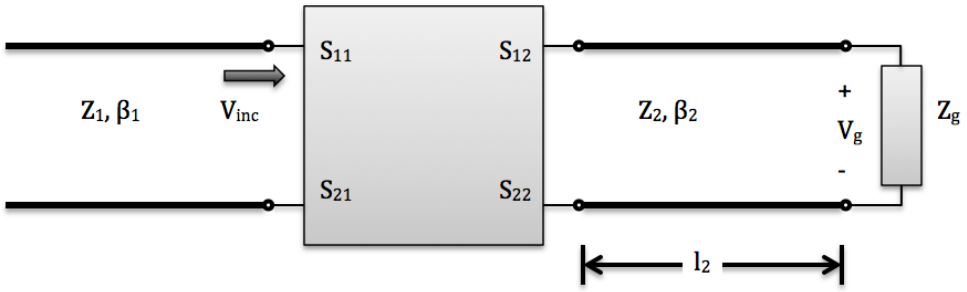

Figure 4.7: Active dipole matching network

be related to the voltage incident on the matching networks input port.

$$V_g(\nu, k_{z0}) = \frac{S_{21}[1+\Gamma_g(\nu, k_{z0})]}{1-S_{22}\Gamma_g(\nu, k_{z0})} e^{-j\beta_2 l_2} V_{inc} \tag{4.42}$$

The active gap impedance from Herper takes into account both the dipole self impedance and the mutual impedance. This can be seen by extending (4.1) to an N element array and solving for the active gap impedance to yield

$$Z_{1d} = \frac{V_1}{I_1} = Z_{11} + Z_{12}\left(\frac{I_2}{I_1}\right) + \cdots + Z_{1N}\left(\frac{I_N}{I_1}\right), \tag{4.43}$$

in which Z_{1d} is the active gap impedance, also commonly called the drive-point impedance. However, before an open-circuit mutual couping model can be developed the self impedance and the $N-1$ mutual impedances in (4.43) need to be known.

The dipole mutual impedance model described as part of the ULA dipole array can be leveraged here, but care must be taken in doing so. The previous dipole model was able to predict the mutual impedance between two dipoles under the assumptions that: 1) the dipoles were suspended in free space and 2) by using an idealized current distribution. In the conformal array the dipoles are not in free space but rather suspended over a PEC cylinder, and their current distribution is not the idealized sinusoidal distribution. The first challenge can be overcome by applying image theory [74, p. 314–323] to replace the PEC cylinder with a set of equivalent sources. The current distributions, derived from Herper's work, can

then be used to replace the idealized dipole currents. Figure 4.8 depicts the canonical image theory example in which a current source is suspended over a flat PEC boundary. Image theory states that an identical field is produced in the upper half-space by the combination of real and image sources without the PEC boundary as the real sources over the PEC boundary. This will add additional array elements, but will remove the PEC boundary and allow the dipole mutual coupling model to be leveraged.

For large cylinders with dipoles placed close to the surface it may be practical to approximate the cylinder as locally flat. However, for the general case the curvature of the cylinder will need to be considered. Figure 4.9 show how image theory can be applied to cylindrical structures [61, p. 48–49]. The most notable change is in the location of the equivalent source. In the flat PEC boundary case the real and equivalent source are placed equal distances from the boundary. In contrast, the equivalent source is places an offset distance from the center of the cylinder based on the size of the cylinder and the distance of the real source. This now allows for the creation of an equivalent model to which the dipole mutual impedance model can be applied.

The self impedance Z_{11} from (4.43) can now be found by considering a single dipole above the PEC cylinder. Image theory generates a second dipole separated by a distance of $d = r - r'$. Equations (4.17)–(4.21) can now be applied to find the mutual impedances and the self impedance can be calculated as the drive point impedance

$$Z_{1d} = \frac{V_1}{I_1} = Z_{11} + Z_{12}\left(\frac{I_2}{I_1}\right), \tag{4.44}$$

with $I_1 = -I_2$.

Calculating the $N-1$ mutual impedance terms in (4.43) is a little more challenging. It starts by considering two dipoles suspended over a PEC cylinder and applying image theory as illustrated in Figure 4.10. This produces a total of four dipoles that must be considered. The mutual impedance between the two real dipoles can be calculated by evaluating (4.13).

As before $I(z')$ is equal to the current distribution on dipole two but $E_z(z')$ is now equal to the sum of E-fields induced by the three other dipoles

$$Z_{21_{PEC}} = \frac{V_{21}}{I_2(0)} = \frac{-1}{I_2(0)[I_1(0) + I_1'(0) + I_2'(0)]} \int_{-l/2}^{l/2} [E_{z21}(z') + E_{z21'}(z') + E_{z22'}(z')] I_2(z') dz'. \tag{4.45}$$

This expression can be evaluated numerically or split into constituent components to reveal

$$Z_{21_{PEC}} = Z_{21} - Z_{21'} - Z_{22'}. \tag{4.46}$$

This indicates that the mutual impedance between two conformal dipoles is equal to the mutual impedance of the dipoles in free space perturbed by the mutual impedances of of the dipole images in the PEC cylinder.

All the required components are now in hand to create an open-circuit mutual coupling model for a conformal array of dipoles suspended over a PEC cylinder. The work of Herper et al. contributes the active gap impedance as well as the current distribution on the array elements. While the careful application of image theory and the dipole mutual impedance model helps derive the mutual impedances between array elements.

4.1.4 Microwave Front-End Design

Many antenna models focus on the current and/or charge distribution on an antenna and the resulting fields dictated by Maxwell's equations, while simplifying the RF hardware connected to the antenna down to a Thévenin equivalent model. This abstraction simplifies the overall problem, but care needs to be taken as this can mask some important underlying issues. Of particular interest is the effective load impedance the microwave front-end places on the antenna in different operating modes. In this section we start with the simple Thevenin model seen in Figure 4.11 and slowly increase the complexity of the microwave front-end model so it more accurately reflects reality. This is accomplished by first adding in the

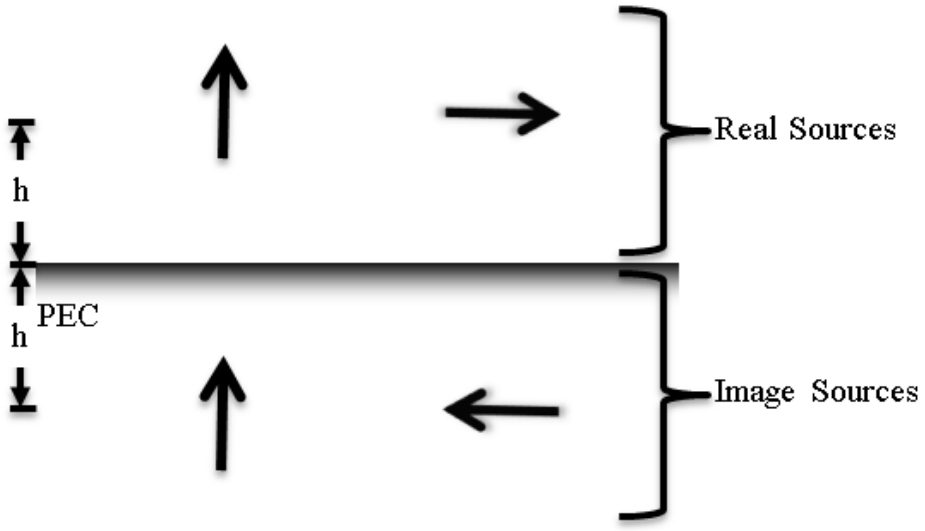

Figure 4.8: Real and equivalent sources for a flat PEC plain

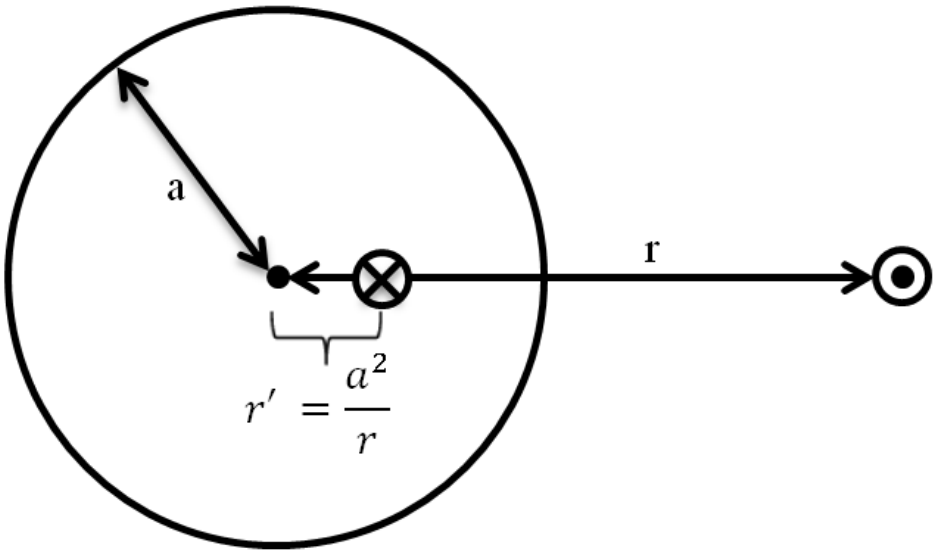

Figure 4.9: Real and equivalent sources for a cylindrical PEC object

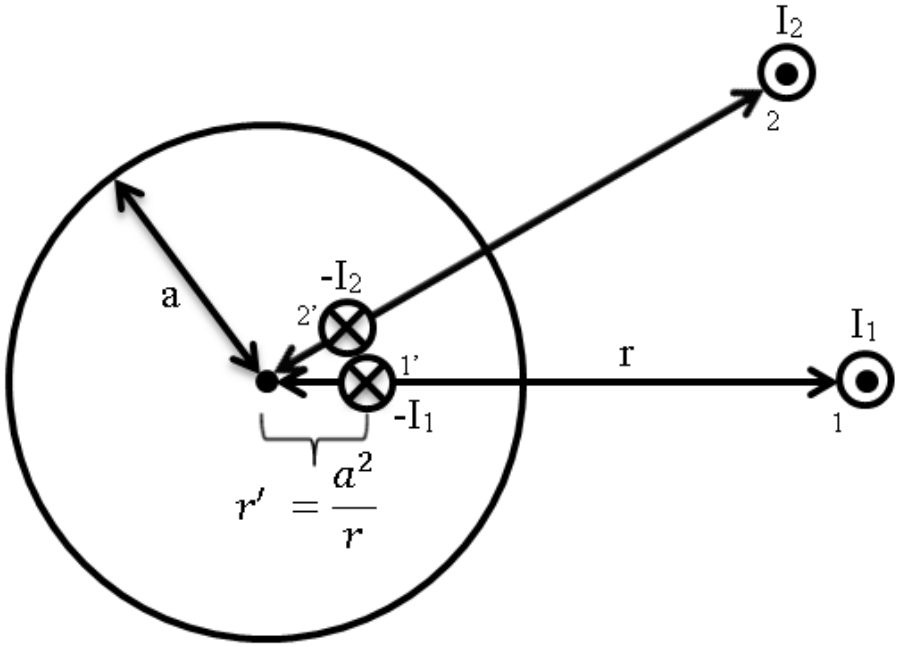

Figure 4.10: Real and equivalent sources for determining the mutual impedances between two conformal elements

antenna feed line and matching structure, then incorporating a transmit/receive (T-R) switch before finally examining the power amplifier and low noise amplifier. It will be shown that these amplifiers place a different load impedance on the antenna depending on the position of the T-R switch, and this in turn changes the mutual coupling between adjacent elements.

4.1.4.1 Antenna Matching and Feeding Network

Without loss of generality we start by considering a two element array which has been arranged in Figure 4.12 to resemble a two port network. In a previous section the mutual coupling between these two dipoles was described using mutual impedances, also known as Z-parameters. However, most microwave systems are described using scattering parameters. The process for transforming between Z-parameters and S-parameters is readily available in many texts and the reader is referred to [62, p. 187] for specifics.

Very few antennas are connected directly to an RF source, so the first modification to

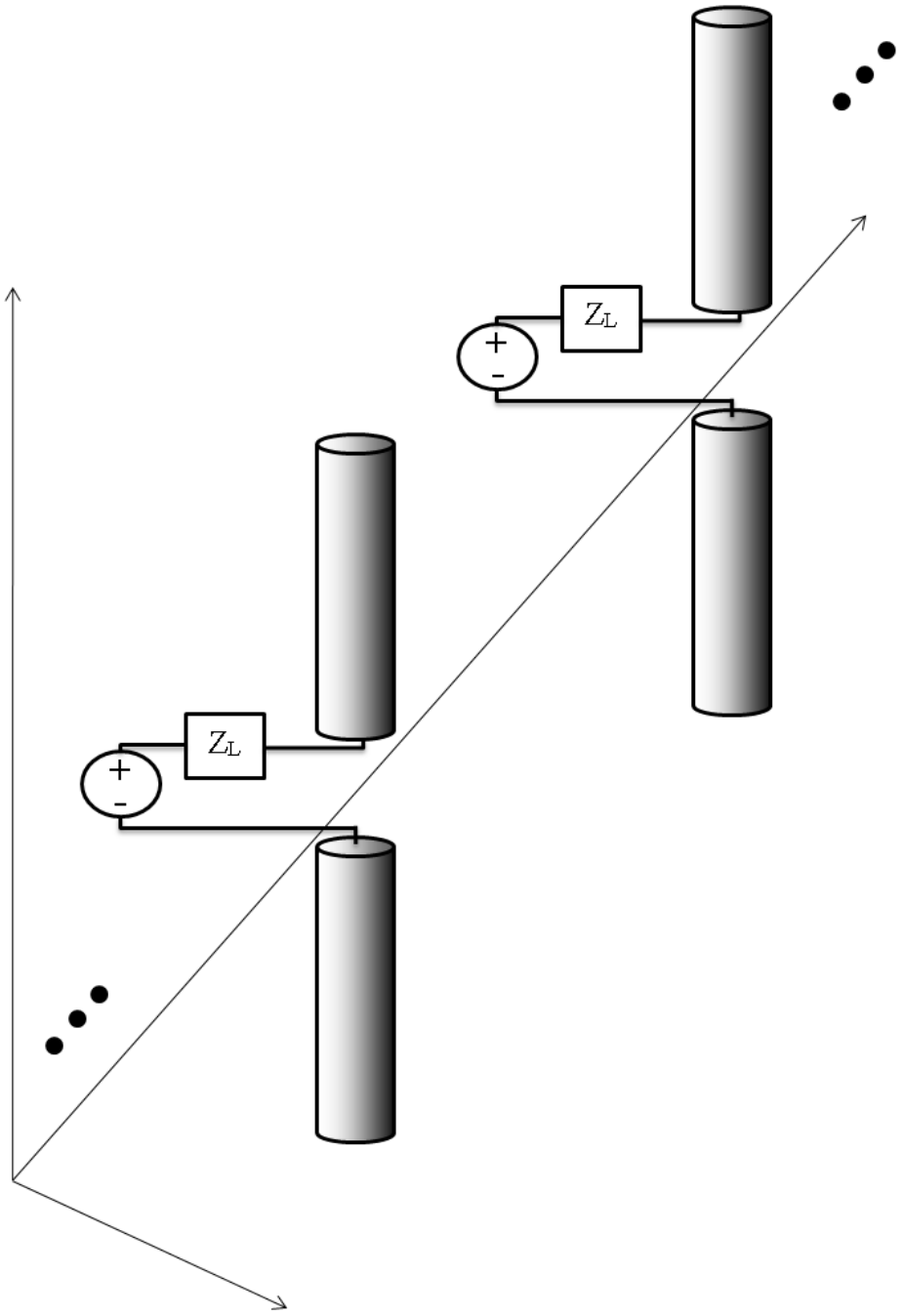

Figure 4.11: Dipole array with element Thevenin model

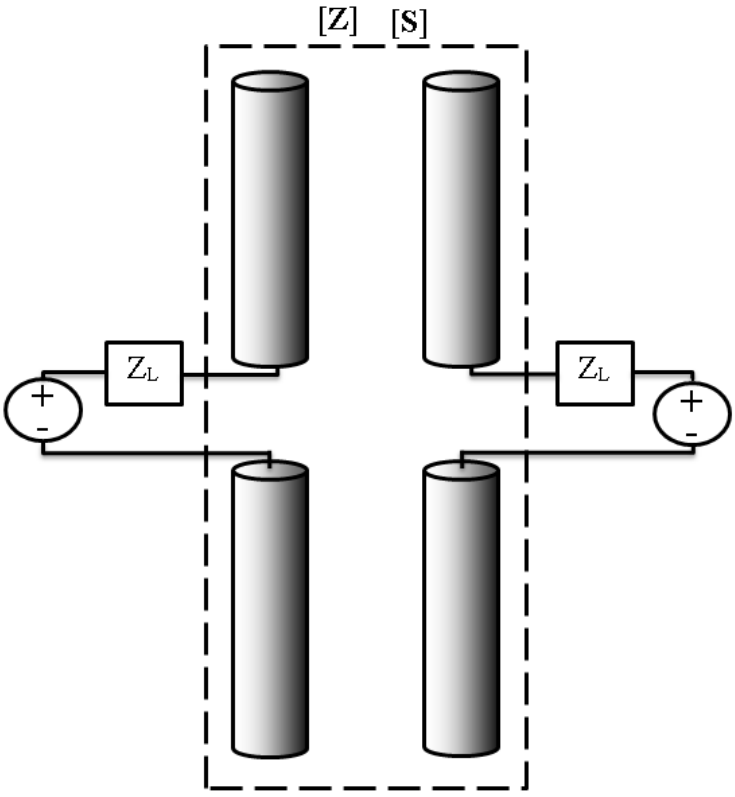

Figure 4.12: Two element dipole array laid out as a two port network

the array model is to add a transmission line with impedance Z_0 and a matching network to minimize reflections between the antenna's drive impedance and Z_0. Figure 4.13 depicts the updated model.

4.1.4.2 Transmit-Receive Switch

As an array is typically used for both transmitting and receiving signals some sort of switching network is used to connect the antenna to either the transmitter or the receiver. This switching network may consist of a T-R switch or a ferrite circulator and in either case it is three port network that connects to a source and a load. Figure 4.14 shows one half of the two port network updated to include the switching network. The T-R switch connects to either a transmitting source, modeled as a Thévenin source with source impedance Z_s or a receive low noise amplifier denoted by load resistor Z_L. In an ideal system both Z_L and Z_s

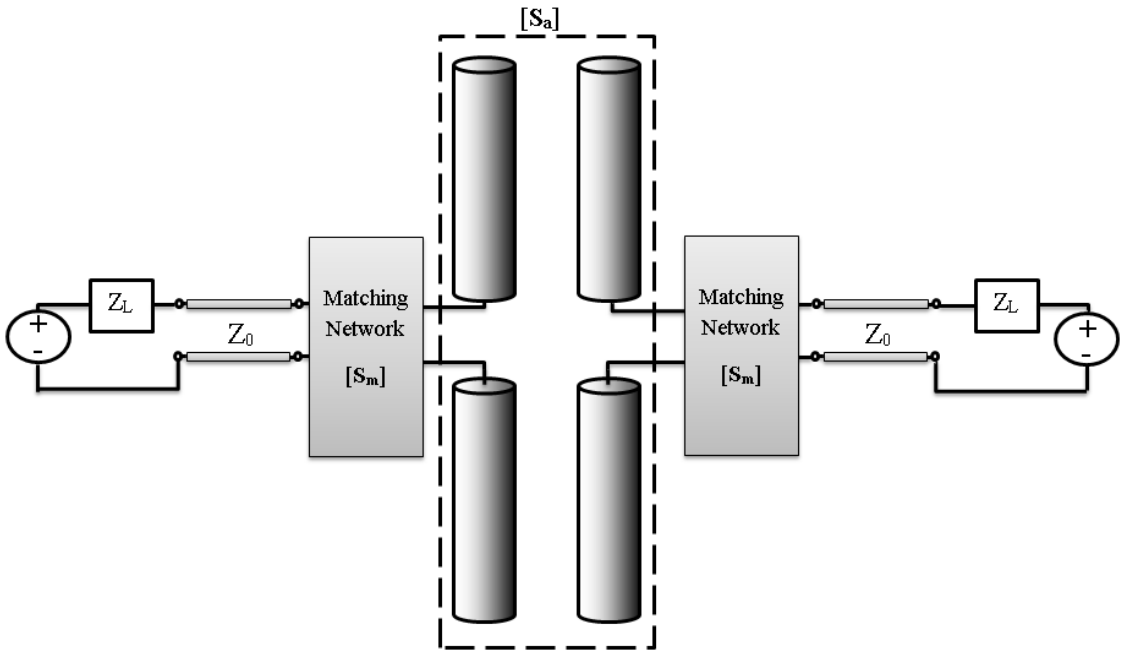

Figure 4.13: Two element dipole array with matching networks

would be matched to Z_0 and the antenna matching network would present a conjugate match to the antenna's drive point impedance maximizing power transfer. In this idealized case the load seen by the antenna is the same whether the array is transmitting or receiving and the modifications made so far have not added anything meaningful to the model. However, once realistic models of transmitting amplifier and receive LNA are developed any perturbation from ideal will propagate through these additions before reaching the antenna.

4.1.4.3 Microwave Amplifiers

Microwave amplifiers play a key role in RF systems, and understanding how these devices are designed is vitally important to understanding how they affect the mutual coupling between array elements. Consider the generic single stage amplifier seen in Figure 4.15, where a transistor with scattering parameters $[\mathbf{S}]$ is matched to source and load impedance Z_0 by an input and output matching network described by $[\mathbf{S}_i]$ and $[\mathbf{S}_o]$ respectively. Pozar tells us that the amplifier will obtain maximum gain when the matching networks provide a

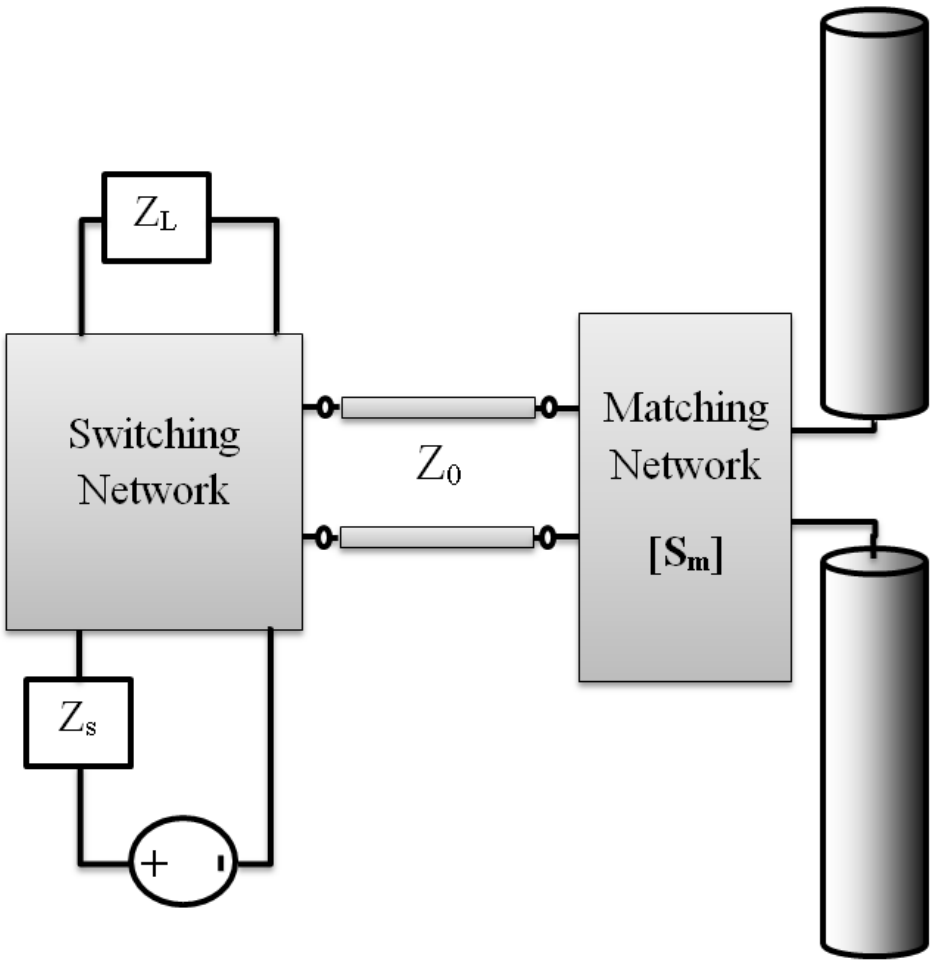

Figure 4.14: Two element dipole array with matching network and switching network

conjugate match to the transistors source and load impedances,

$$\Gamma_{\text{in}} = \Gamma_S^* \tag{4.47}$$

and

$$\Gamma_{\text{out}} = \Gamma_L^*, \tag{4.48}$$

where * denotes conjugation [62, p. 548]. In this conjugate matched case, the matching networks transform Z_0 such that the transistor sees an optimal Z_{in}^* connected to the input and Z_{out}^* connected to the output. Conversely the matching networks transforms the transistor's input and output impedance such that the impedance looking into the amplifier from either direction appears to be Z_0. This conjugately matched amplifier would then imply that both Z_L and Z_s in Figure 4.14 would be equal to Z_0 and the antenna element would be presented with identical loads regardless of the T-R switch position.

Most amplifiers do not use conjugate matching networks. Designing an amplifier with conjugate matching maximizes gain but significantly limits bandwidth. Input and output matching networks can only provide a conjugate match over a relatively narrow bandwidth so the peak obtainable gain is realized only over that small bandwidth and the gain tends to drop off rapidly outside that band. Instead design engineers trade gain for bandwidth and *mismatches are purposely introduced* [in the matching networks] *to reduce the overall gain* [62, p. 553]. Now, the impedance looking into the amplifier is no longer Z_0 but some other impedance value, and the apparent input impedance is almost certainly a different value from the apparent output impedance. This is key, as now Z_L and Z_s in Figure 4.14 are not only not equal to Z_0 but are no longer equal to each other. This difference in impedance value will propagate through the microwave front end and present the antenna with a different load impedance, depending on the state of the T-R switch, and ultimately result in a different induced voltage values at each of the the array elements.

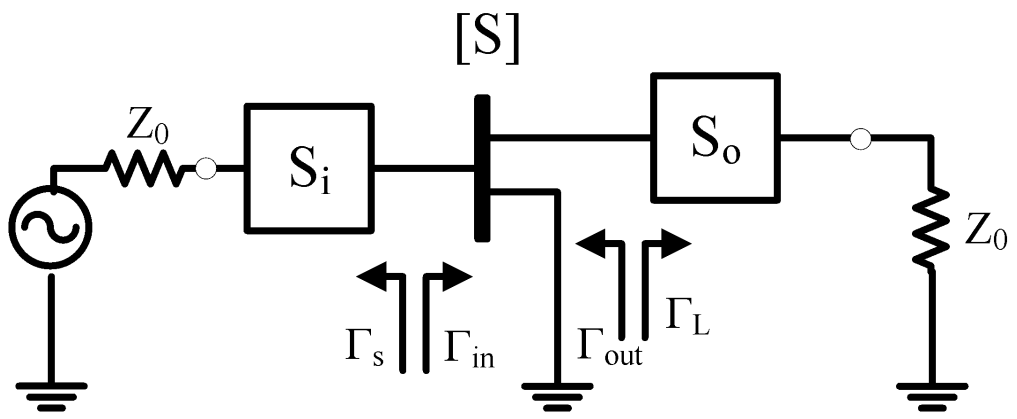

Figure 4.15: Single Stage Amplifier Diagram

4.2 Simulation Setup

Before the impact of substituting a transmit array manifold for a receive manifold can be undertaken the updated array element model seen in Figure 4.14 needs to be incorporated into the mutual coupling model, the array mutual impedance values need to be calculated and the array manifold constructed. Once this is complete a set of simulations can be undertaken to compare the performance of some common array processing algorithms using the correctly matched and mismatched array manifolds.

4.2.1 Integrating Hardware and Mutual Coupling Models

The mutual coupling models thus far considered have been expressed in terms of Z-parameters, in contrast the array element model has been expressed in S-parameters. Rather than continue with the two models expressed in different terms, the mutual coupling model will be recast into scattering parameters. Consider a two element array excited by a distance source, the mutual impedances can be transformed into S-parameters and the array described by the signal flow diagram seen in Figure 4.16a. Since the excitation source is far away we consider only signal paths directly from the distant source and neglect any secondary loops that would form from signals bouncing between the source and the array. We will specifically consider signals flowing from the distant source to element one as seen in Figure 4.16b. Between

4.16b and 4.16c the self-loops created when signals are incident on an array element are partial reflected and re-radiated are collapsed. The final flow diagram can be seen in Figure 4.16d and we can now see the signal at array element one is the sum of the direct path plus a portion of the signal scattered from element two, plus a diminishing set of terms representing repeated scattering between elements one and two. Neglecting these multi-scatter terms we can write the transmission from the the distant source to element one as

$$T_1 = S_{13} + \frac{S_{12}\Gamma_L}{1 - S_{22}\Gamma_L} S_{23}. \tag{4.49}$$

This can be extended to an N element array to produce

$$\mathbf{T} = \begin{bmatrix} T_1 \\ T_2 \\ \vdots \\ T_N \end{bmatrix} = \begin{bmatrix} 1 & \frac{S_{12}\Gamma_L}{1-S_{22}\Gamma_L} & \cdots & \frac{S_{1N}\Gamma_L}{1-S_{NN}\Gamma_L} \\ \frac{S_{21}\Gamma_L}{1-S_{11}\Gamma_L} & 1 & \cdots & \frac{S_{2N}\Gamma_L}{1-S_{NN}\Gamma_L} \\ \vdots & \vdots & \ddots & \vdots \\ \frac{S_{N1}\Gamma_L}{1-S_{11}\Gamma_L} & \frac{S_{N2}\Gamma_L}{1-S_{22}\Gamma_L} & \cdots & 1 \end{bmatrix} \begin{bmatrix} S_{1(N+1)} \\ S_{2(N+1)} \\ \vdots \\ S_{N(N+1)} \end{bmatrix}. \tag{4.50}$$

Or more simply

$$\mathbf{T} = \mathbf{C}\mathbf{S}_\mathbf{s}, \tag{4.51}$$

where $\mathbf{S_s}$ is a vector of S-parameters relating the distant source to each array element, and mutual coupling matrix $\mathbf{C}$ relates incident signal to the forward propagating wave entering the microwave front end. This model can now be integrated into the array signal model very simply. First, the magnitude of each term in vector $\mathbf{S_s}$ is related to the distance between the source and each element. Since the distance between the source and the center of the array is much greater than the distance from one end of the array to the other we can say the magnitude of each term in $\mathbf{S_s}$ is approximately equal to some scalar value α. Since α is a arbitrary scalar value based on the source distance and the array signal model is solely focused on the signal present at the array, and not the propagation from source to array, it can be neglected. This leaves the phase of vector S_s to describe the relative phase value

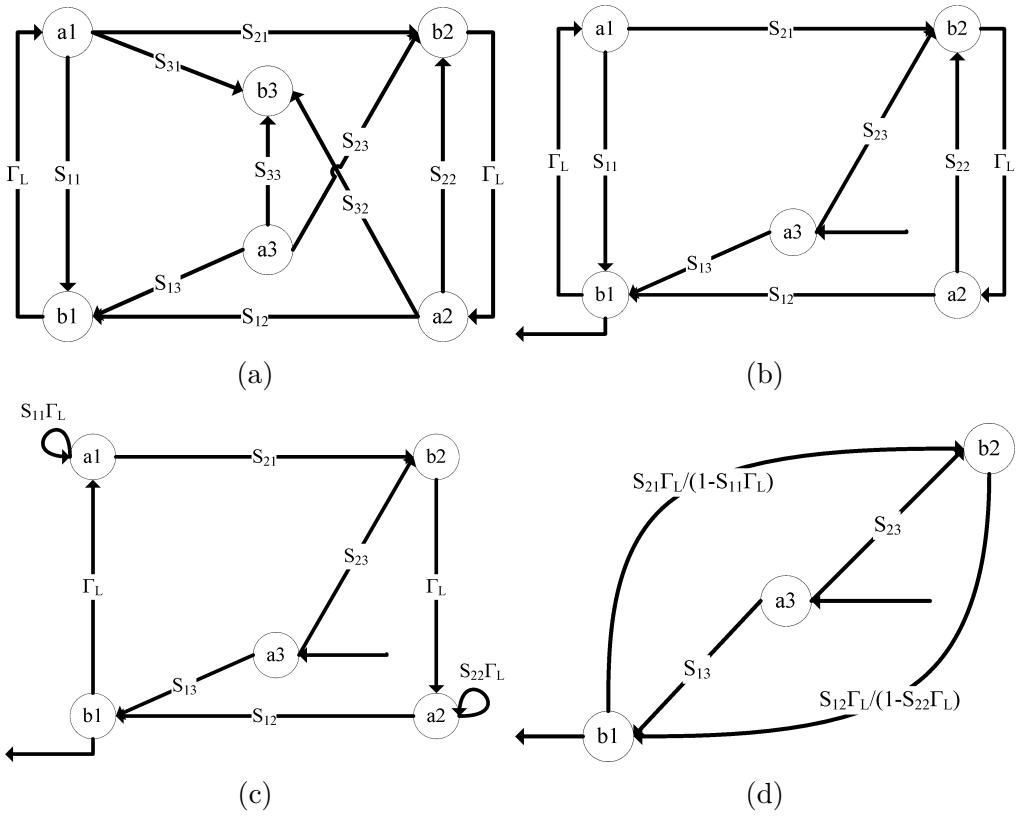

Figure 4.16: S-parameter mutual coupling network flow diagram solution

between each element. In the array signal model this phase information is already captured in the unperturbed array manifold and we can prepend $\mathbf{C}$ to the unperturbed array manifold to model the effects of mutual coupling.

4.2.2 Simulations Setup

With a suitable mutual coupling model integrated with the new model of the microwave front-end, the mutual coupling terms are calculated for a ULA and conformal array of dipoles. The array manifolds are then derived for both the transmitting and receiving configuration. In both cases the matching network seen in Figure 4.14 was designed to match the drive point impedance of the dipole to a 50Ω transmission line. The output return loss of the power amplifier was set to -10 dB with arbitrary phase, while the low noise amplifier had an input return loss of -15 dB again with arbitrary phase. These values are selected after

surveying amplifier specification sheets to find typical return loss values.

Direction of arrival estimators will be used to evaluated the impact of model mismatch with the aid of two metrics. The first metric is the probability of resolving two sources of equal magnitude separated by half the nominal resolution distance. The second metric will look at the RMS error between the predicted DoA and the true DoA. Since the size of the array directly affects the pattern beamwidth, the RMS error will be nominalized with respect to the null-to-null beamwidth of the array. This normalization will allow the RMS error to be compared fairly across arrays of differing lengths.

To calculate these metrics a series of 500 trial Monte Carlo simulations are performed over a suitable SNR range. In each trial the RMS error is calculated and a determination is made as to if the targets have been resolved. At the end of the 500 trials the probability of resolution is calculated and the RMS error is averaged. For both the ULA and the conformal array the continuous array manifold is discretized into M=181 samples, with 2° separating each sample. In each trial L snapshots of data are generated from the array signal model, and results will be presented for L ranging from 5 to 100.

4.3 Results

The impact of transmit-for-receive manifold replacement on DoA estimators was assessed for MUSIC and RISR using two different array geometries. The ESPRIT algorithm was precluded from evaluation as ESPRIT does not require explicit knowledge of the array manifold, and so is not subject to transmit-for-receive manifold mismatch. Results are presented for both a uniform linear array of dipoles, as well as, a conformal array of dipoles suspended over a PEC cylinder. In each case we present the probability of the DoA estimator resolving two non-coherent targets of equal magnitude separated by half the nominal resolution. We also present the RMS error in the DoA estimate for two and four targets. For MUSIC these metrics show a noticeable degradation in performance when the receive array manifold in

place of the arrays true receive manifold. In contrast, RISR shows almost no performance degradation, which is likely due to RISR's robustness to model mismatch in general.

4.3.1 Uniform Linear Array Results

A uniform linear array of antenna elements is a very common geometry and we examine the impact of transmit-receive model mismatch using two DoA estimators. The array is composed of ten $\lambda/2$ dipoles in a side-by-side configuration separated by a distance of $\lambda/2$. The MUSIC algorithms is considered first in Section 4.3.1.1 followed by the RISR algorithm in Section 4.3.1.2

4.3.1.1 MUSIC

The MUSIC algorithm requires knowledge of the number of incident signals, and the results presented in this section MUSIC is supplied with clairvoyant knowledge of the number of sources. Figures 4.17 and 4.18 plot the probability of separating two non-coherent, equal magnitude targets for a range of sample support verse the array SNR (ASNR). ASNR is defined as

$$\text{ASNR} = N\frac{\sigma_s^2}{\sigma_n^2}, \tag{4.52}$$

where σ_s and σ_n are the signal and noise powers respectively. From these two plots the curves for L=10, 25, and 100 were superimposed in Figure 4.19 so the impact in model mismatch can be easily interpreted.

The RMS error in the direction of arrival estimation was also calculated and for the same two closely spaced sources it can be seen Figure 4.20 for the matched array manifold and Figure 4.21 for the mismatch case. The difference in RMS error is plotted for L=10, 25, and 100 is plotted in Figure 4.22. The RMS error for four sources, two closely spaced and two separated by more then the nominal resolution, can be seen in Figures 4.23 and 4.24 with the difference between estimates plotted in Figure 4.25.

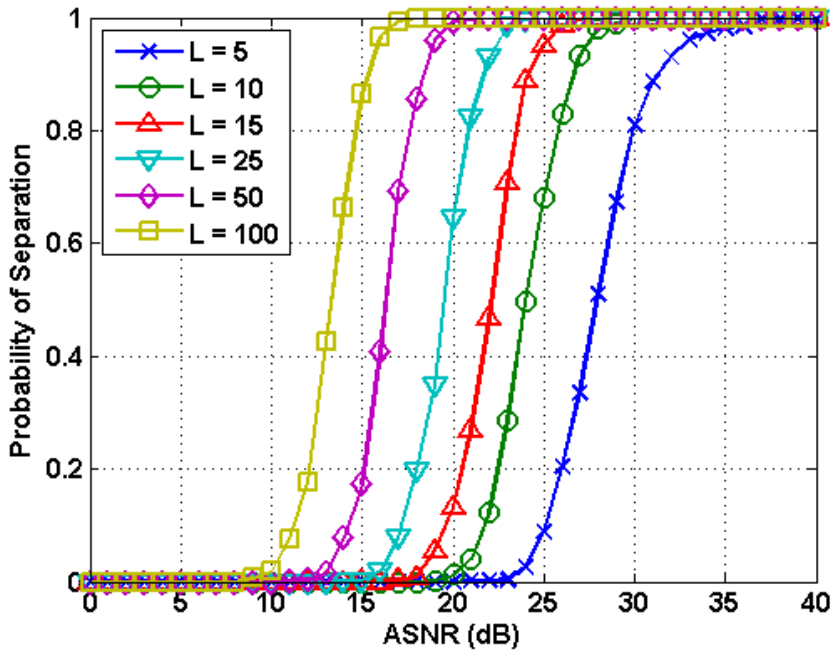

Figure 4.17: Probability of MUSIC separating two targets separated by half the nominal resolution using the correct manifold. $\times$: L=5, $\circ$: L=10, $\triangle$: L=15, $\triangledown$: L=25, $\diamond$: L=50, $\square$: L=100

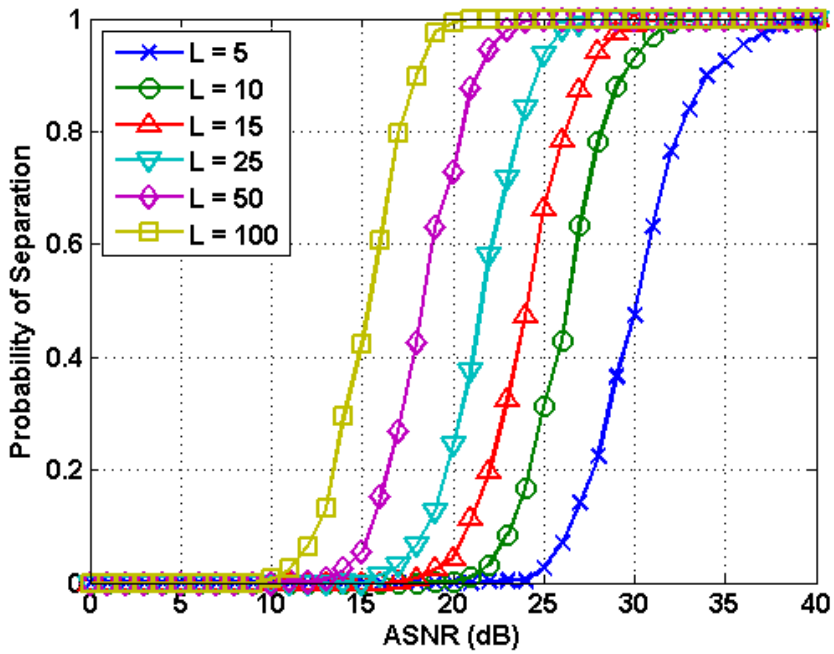

Figure 4.18: Probability of MUSIC separating two targets separated by half the nominal resolution using the mismatched manifold. $\times$: L=5, $\circ$: L=10, $\triangle$: L=15, $\triangledown$: L=25, $\diamond$: L=50, $\square$: L=100

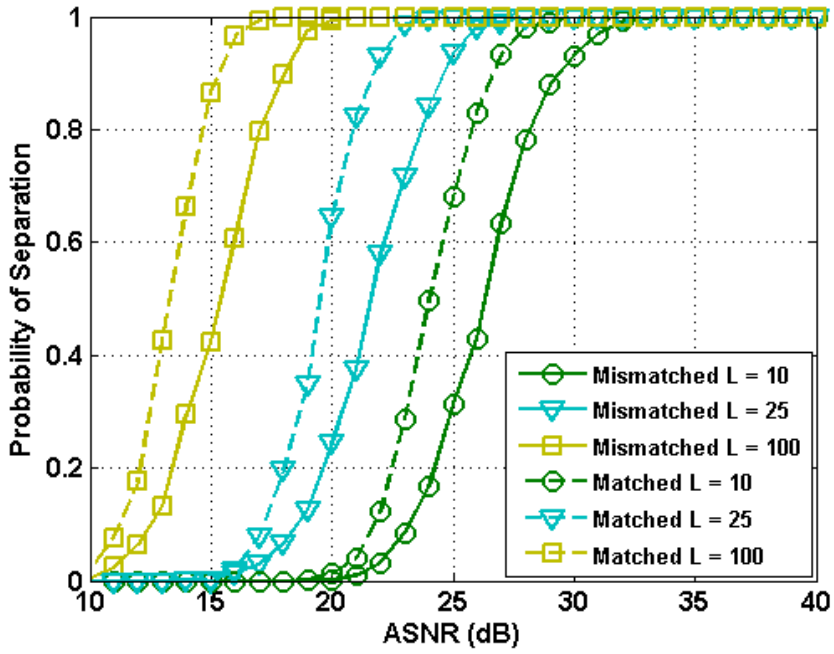

Figure 4.19: Comparison of the probability of MUSIC separating two targets separated by half the nominal resolution using the correct and mismatched array manifold. Dashed lines : correct manifold, Solid lines : mismatched manifolds. $\circ$: L=10, $\triangledown$: L=25, $\square$: L=100

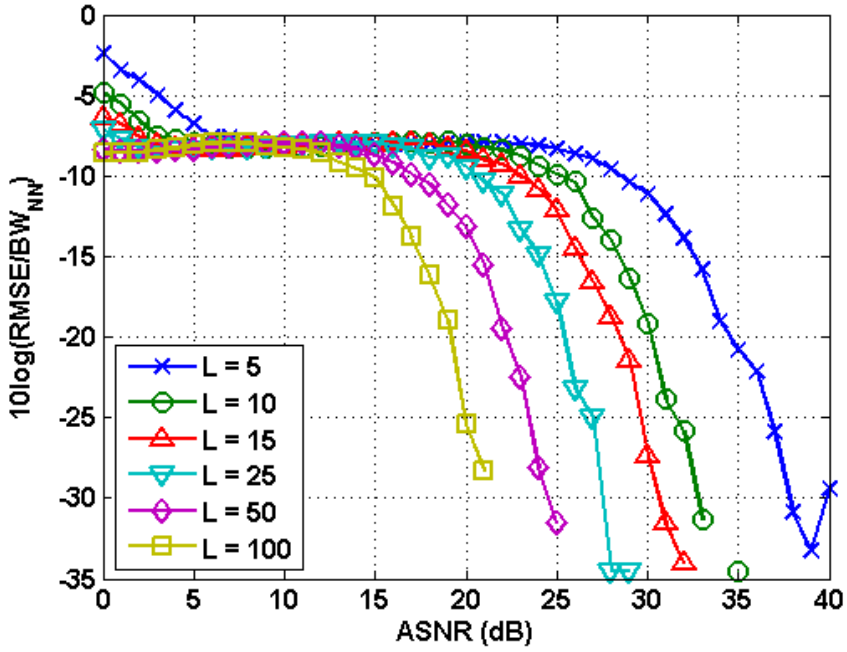

Figure 4.20: RMS error in MUSIC DoA estimates for two targets using the correct manifold. $\times$: L=5, $\circ$: L=10, $\triangle$: L=15, $\triangledown$: L=25, $\diamond$: L=50, $\square$: L=100

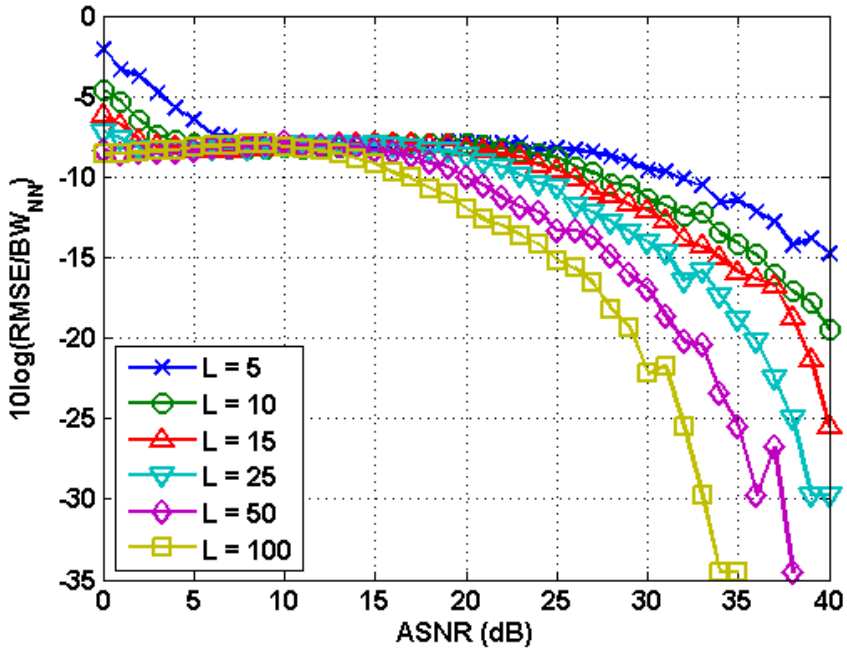

Figure 4.21: RMS error in MUSIC DoA estimates for two targets using the mismatched manifold. $\times$: L=5, $\circ$: L=10, $\triangle$: L=15, $\triangledown$: L=25, $\diamond$: L=50, $\square$: L=100

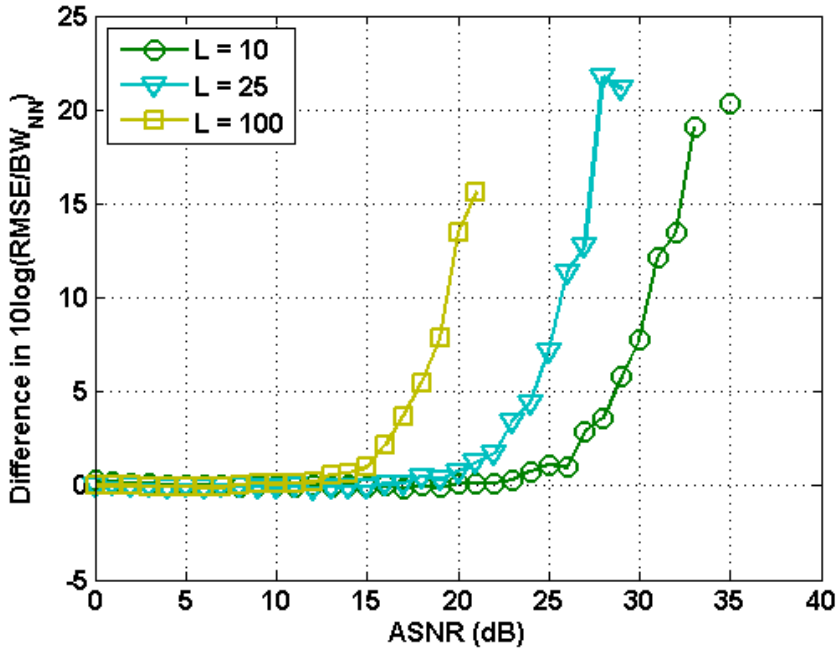

Figure 4.22: Difference in the RMS error of MUSIC DoA estimates for two targets using the correct and mismatched array manifold. $\circ$: L=10, $\triangledown$: L=25, $\square$: L=100

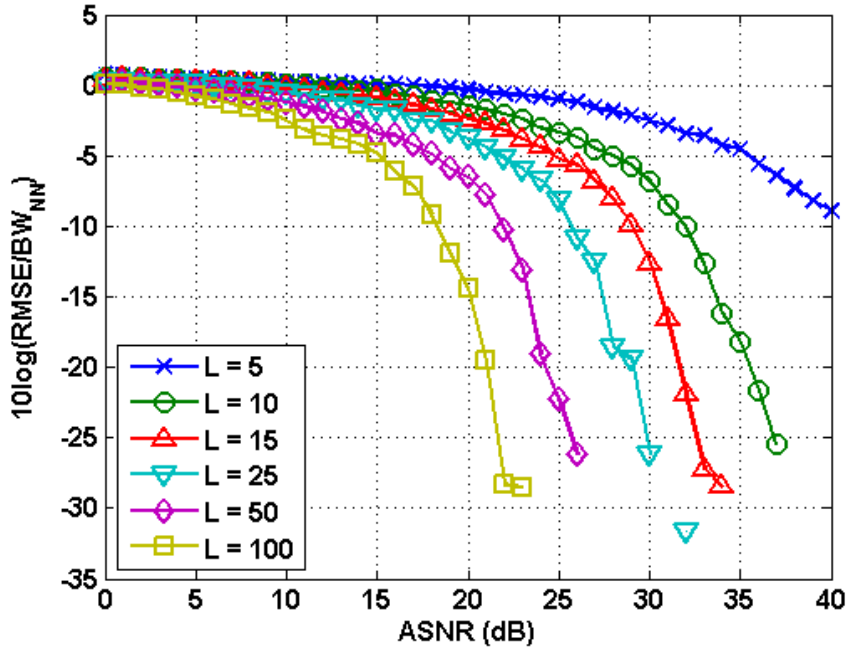

Figure 4.23: RMS error in MUSIC DoA estimates for four targets using the correct manifold. $\times$: L=5, $\circ$: L=10, $\triangle$: L=15, $\triangledown$: L=25, $\diamond$: L=50, $\square$: L=100

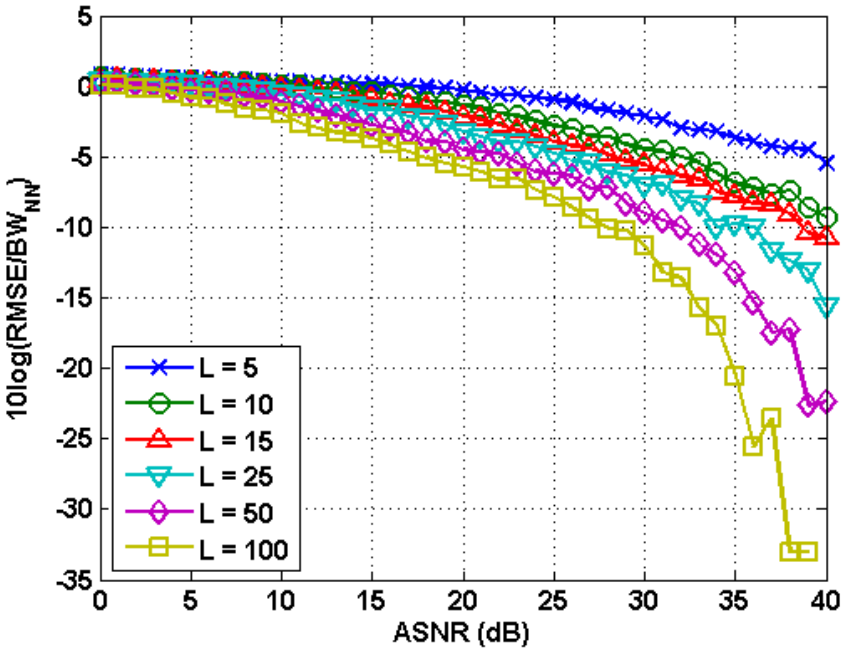

Figure 4.24: RMS error in MUSIC DoA estimates for four targets using the mismatched manifold. × : L=5, ∘ : L=10, △ : L=15, ▽ : L=25, ◇ : L=50, □ : L=100

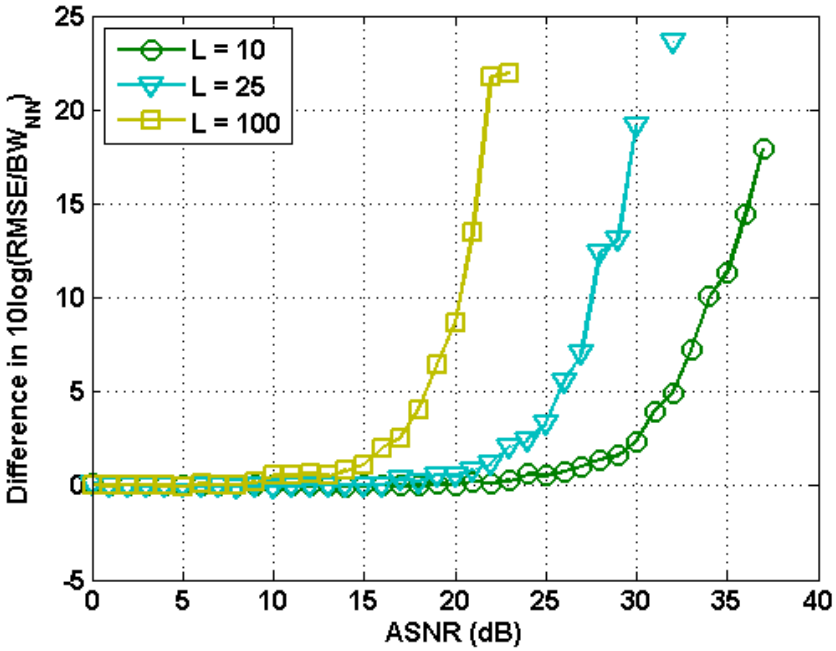

Figure 4.25: Difference in the RMS error of MUSIC DoA estimates for four targets using the correct and mismatched array manifold. ∘ : L=10, ▽ : L=25, □ : L=100

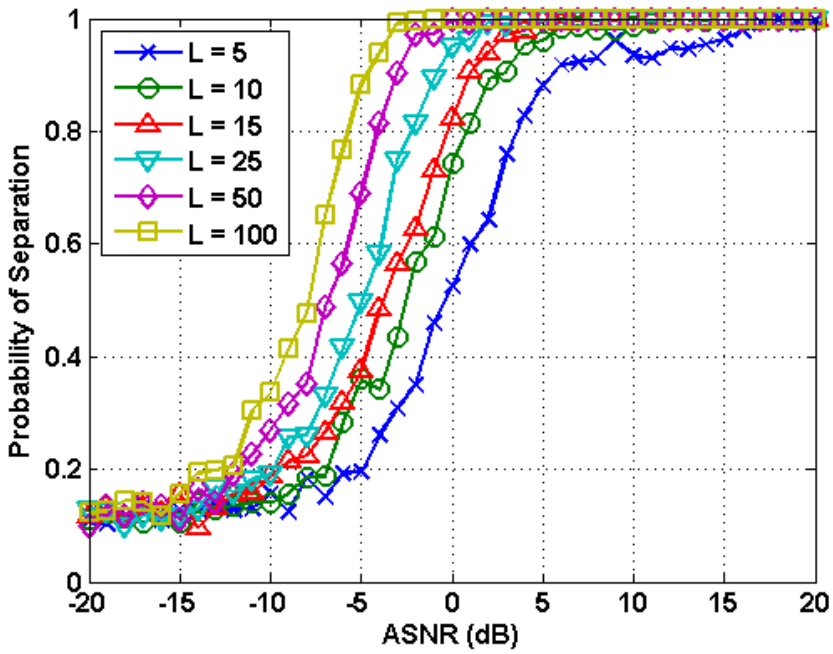

Figure 4.26: Probability of RISR separating two targets separated by half the nominal resolution using the correct manifold. $\times$: L=5, $\circ$: L=10, $\triangle$: L=15, $\triangledown$: L=25, $\diamond$: L=50, $\square$: L=100

4.3.1.2 RISR

The RISR algorithm was configured for 10 iterations, with a noise loading factor of $\alpha = 1/8$. Both the noise variance and model variance terms were assumed to be known rather than estimated as part of the algorithm. Figures 4.26 and 4.27 plot the probability of separating two closely spaced sources for the matched and mismatched array manifold respectively. There is very little difference between the two and this is apparent in Figure 4.28 as the matched and mismatched manifold traces lay on top of each other.

The RMS error in the RISR DoA estimation for two closely spaced sources can be seen in Figures 4.29 and 4.30. As with the probability of separation plots there is very little difference between these plots, and Figure 4.31 plots this small difference. This trend continues for the four source test case as seen in Figures 4.32–4.34.

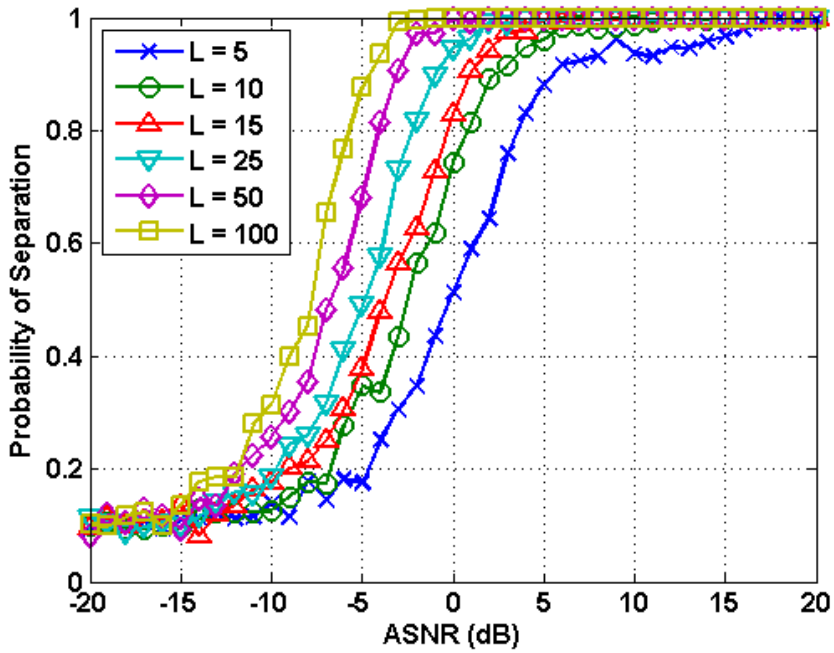

Figure 4.27: Probability of RISR separating two targets separated by half the nominal resolution using the mismatched manifold. $\times$: L=5, $\circ$: L=10, $\triangle$: L=15, $\triangledown$: L=25, $\diamond$: L=50, $\square$: L=100

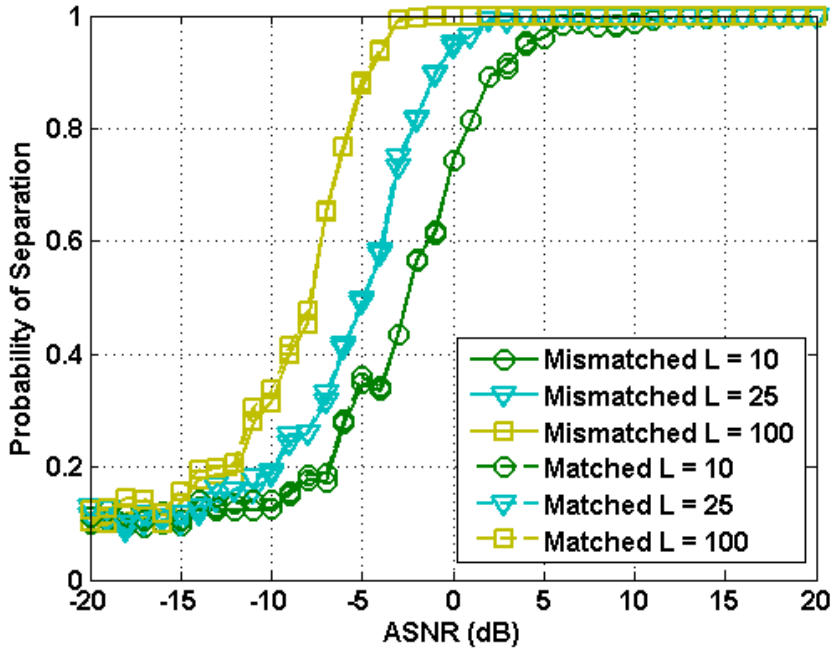

Figure 4.28: Comparison of the probability of RISR separating two targets separated by half the nominal resolution using the correct and mismatched array manifold. Dashed lines : correct manifold, Solid lines : mismatched manifolds. $\circ$: L=10, $\triangledown$: L=25, $\square$: L=100

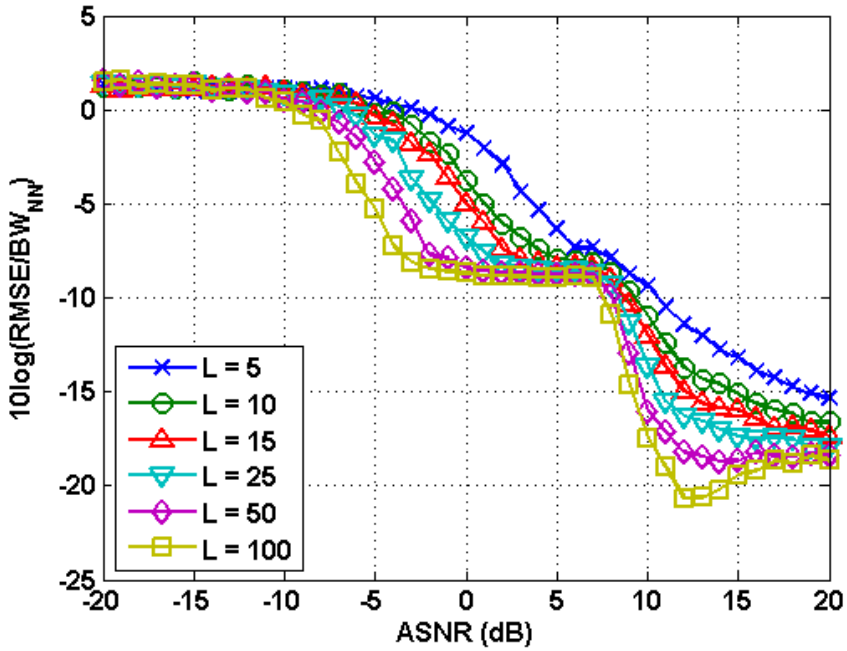

Figure 4.29: RMS error in RISR DoA estimates for two targets using the correct manifold. × : L=5, ∘ : L=10, △ : L=15, ▽ : L=25, ◇ : L=50, □ : L=100

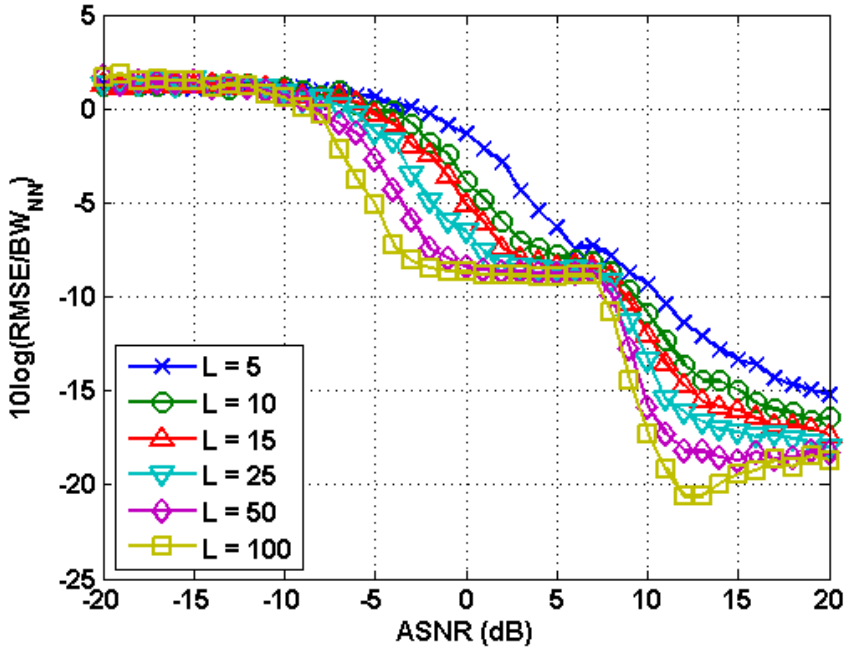

Figure 4.30: RMS error in RISR DoA estimates for two targets using the mismatched manifold. × : L=5, ∘ : L=10, △ : L=15, ▽ : L=25, ◇ : L=50, □ : L=100

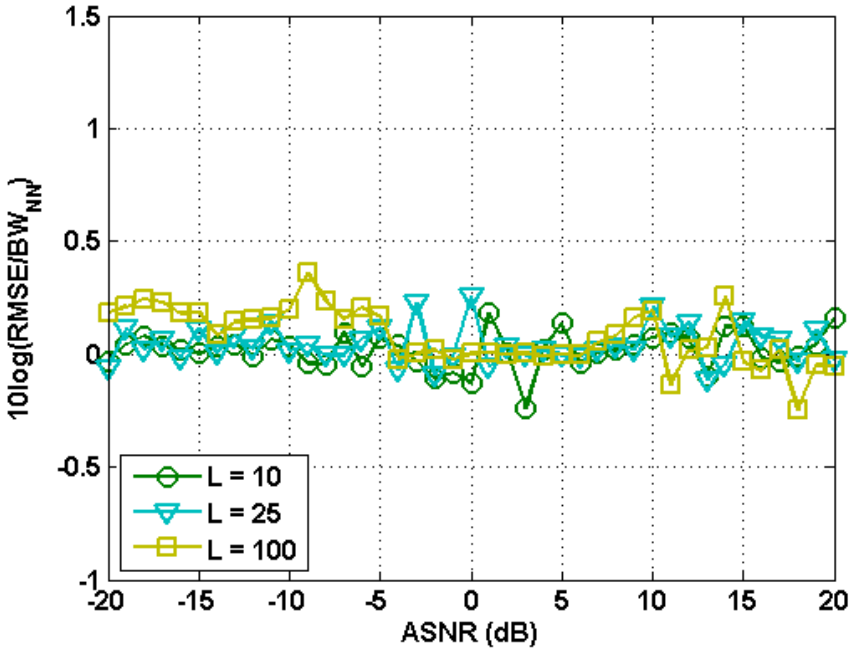

Figure 4.31: Difference in the RMS error of RISR DoA estimates for two targets using the correct and mismatched array manifold. ∘ : L=10, ▽ : L=25, □ : L=100

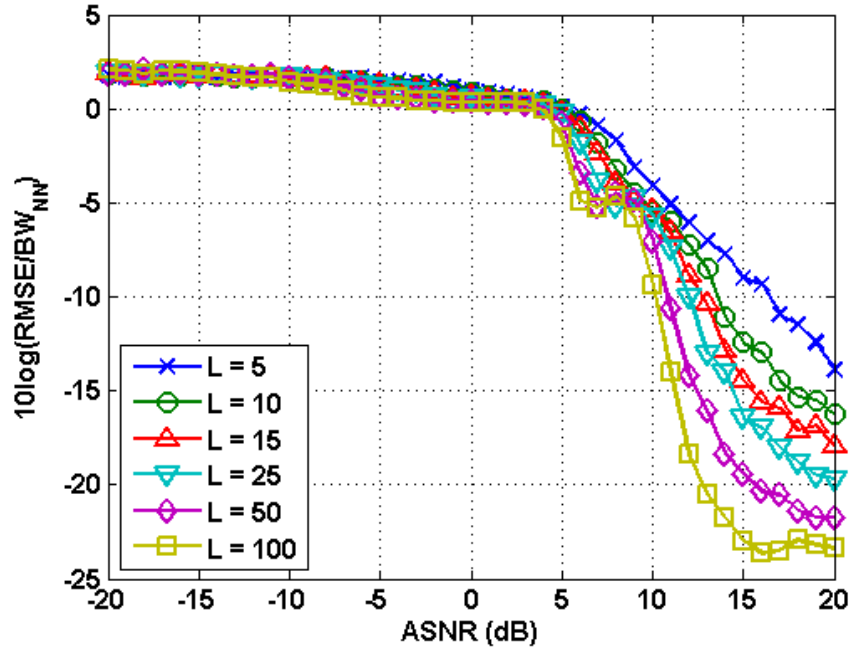

Figure 4.32: RMS error in RISR DoA estimates for four targets using the correct manifold. × : L=5, ∘ : L=10, △ : L=15, ▽ : L=25, ◇ : L=50, □ : L=100

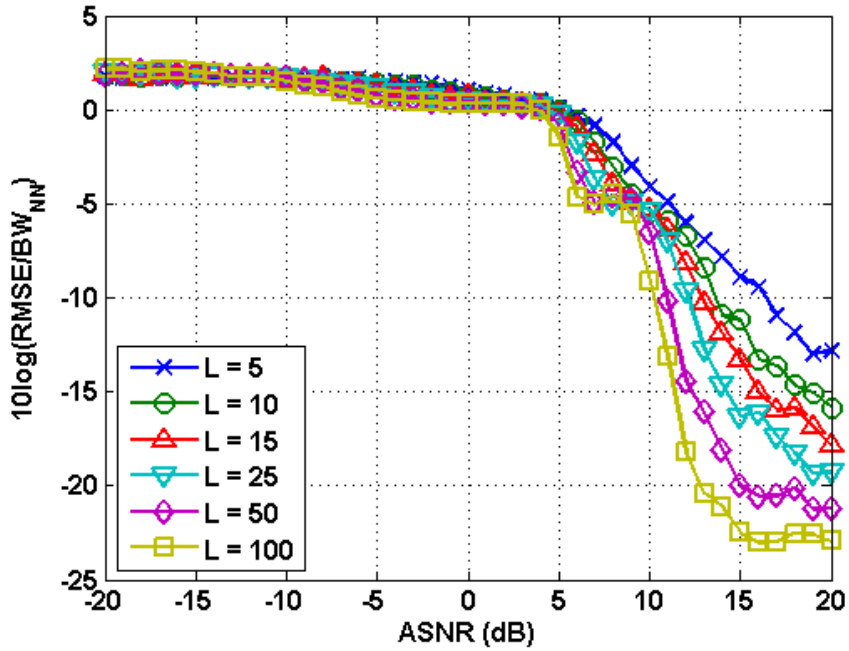

Figure 4.33: RMS error in RISR DoA estimates for four targets using the mismatched manifold. × : L=5, ∘ : L=10, △ : L=15, ▽ : L=25, ◇ : L=50, □ : L=100

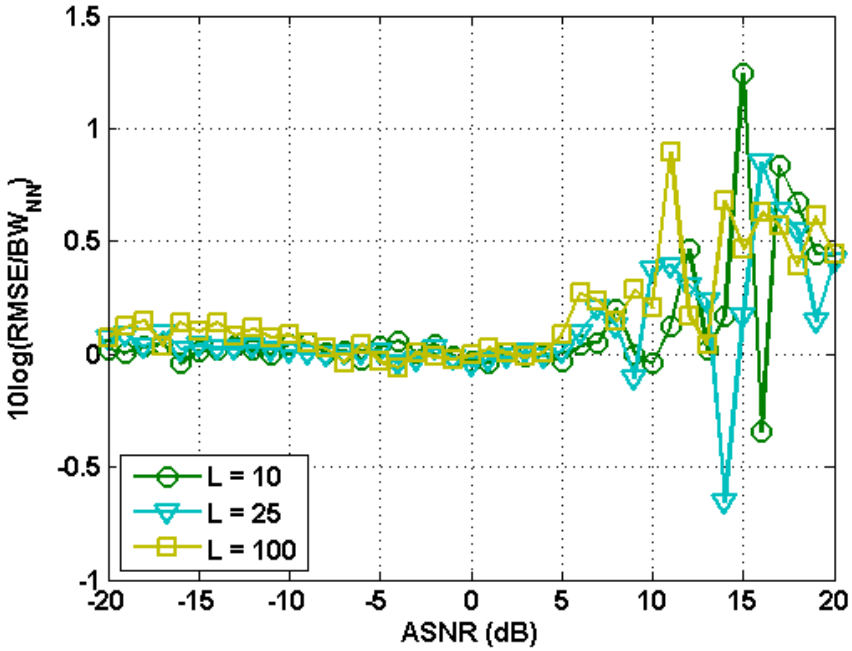

Figure 4.34: Difference in the RMS error of RISR DoA estimates for four targets using the correct and mismatched array manifold. ∘ : L=10, ▽ : L=25, □ : L=100

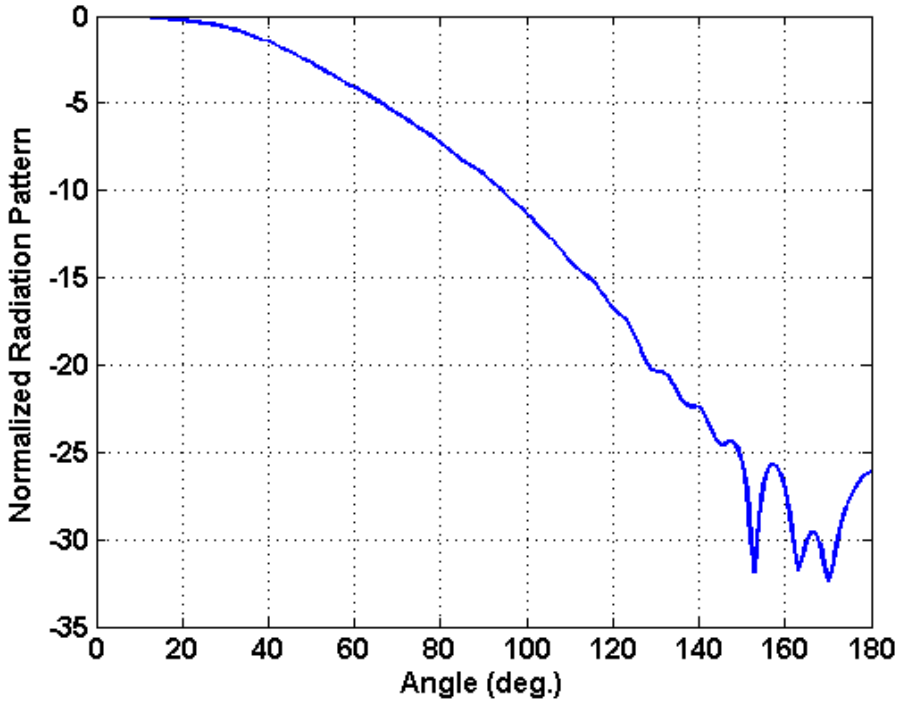

Figure 4.35: Embedded element pattern for 54 element conformal array

4.3.2 Conformal Array Results

The conformal array is less common then the ULA considered earlier but is never the less interesting. One interesting aspect of the conformal array considered herein is that the elements are outward facing and that the embedded element pattern is known from the works of Herper and is plotted in Figure 4.35. Often times circular arrays and cylindrical arrays are considered in analogy to circular apertures and constrained to beam patterns broadside to the entire array, such that all elements can contribute simultaneously. In contrast, here only a small subset of the array elements contribute to the transmission and reception of signals for a given angle.

4.3.2.1 MUSIC

For the conformal array, MUSIC is again supplied with clairvoyant knowledge of the number of sources and we consider both probability of separating two closely spaced targets as well

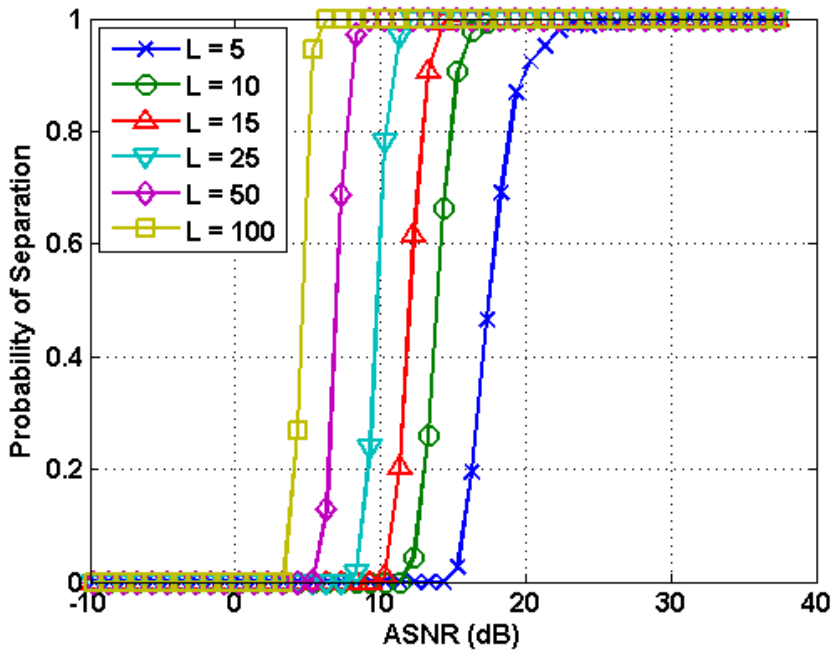

Figure 4.36: Probability of MUSIC separating two targets separated by half the nominal resolution using the correct manifold, conformal array. $\times$: L=5, $\circ$: L=10, $\triangle$: L=15, $\triangledown$: L=25, $\diamond$: L=50, $\square$: L=100

as the RMS error in DoA estimates for two and four targets. The probability of separating targets using the correct matched array manifold can be seen in Figure 4.36, while the mismatched case is plotted in Figure 4.37. As before the difference between the probabilities is plotted in Figure 4.38 for a selection of time sample support.

The RMS error in the DoA estimates for two closely spaced targets when MUSIC is assuming the correct and mismatched array manifolds can be seen in Figures 4.39 and 4.40 respectively. The difference in error between the two models is plotted in Figure 4.41.

Similarly, the RMS error in DoA estimates for 4 targets, two of which are closely spaced, can be seen in Figures 4.42 and 4.43, with the difference between them plotted in Figure 4.44.

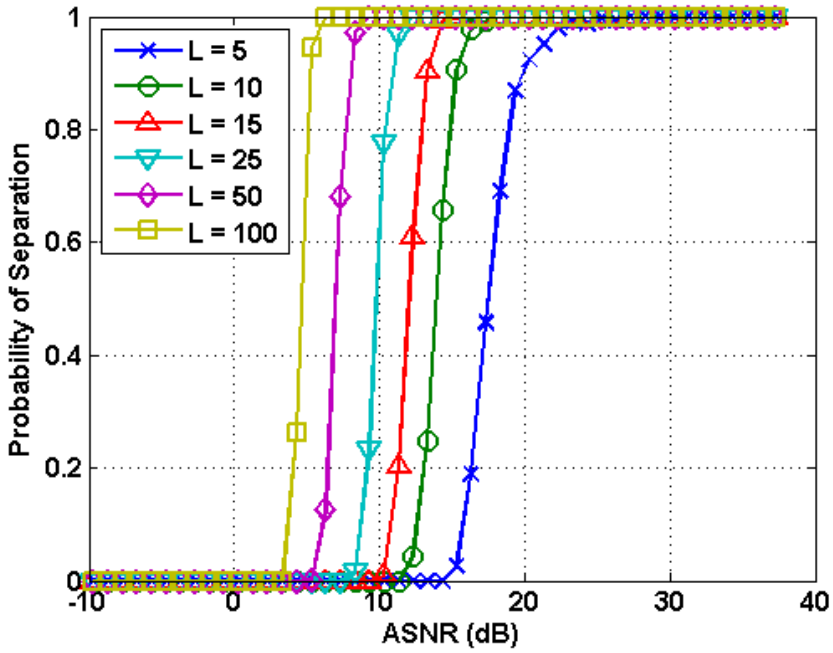

Figure 4.37: Probability of MUSIC separating two targets separated by half the nominal resolution using the mismatched manifold, conformal array. $\times$: L=5, $\circ$: L=10, $\triangle$: L=15, $\triangledown$: L=25, $\diamond$: L=50, $\square$: L=100

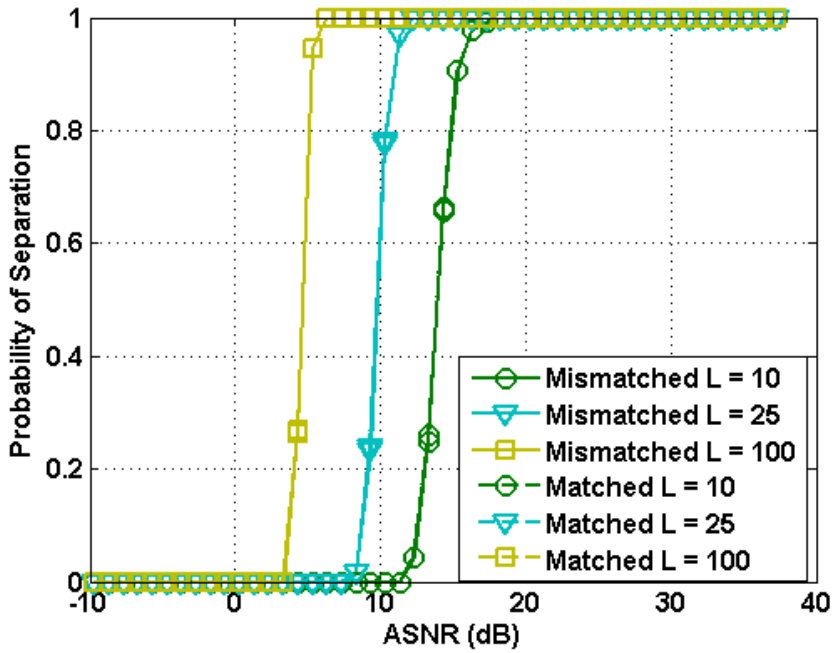

Figure 4.38: Comparison of the probability of MUSIC separating two targets separated by half the nominal resolution using the correct and mismatched array manifold, conformal array. Dashed lines : correct manifold, Solid lines : mismatched manifolds. $\circ$: L=10, $\triangledown$: L=25, $\square$: L=100

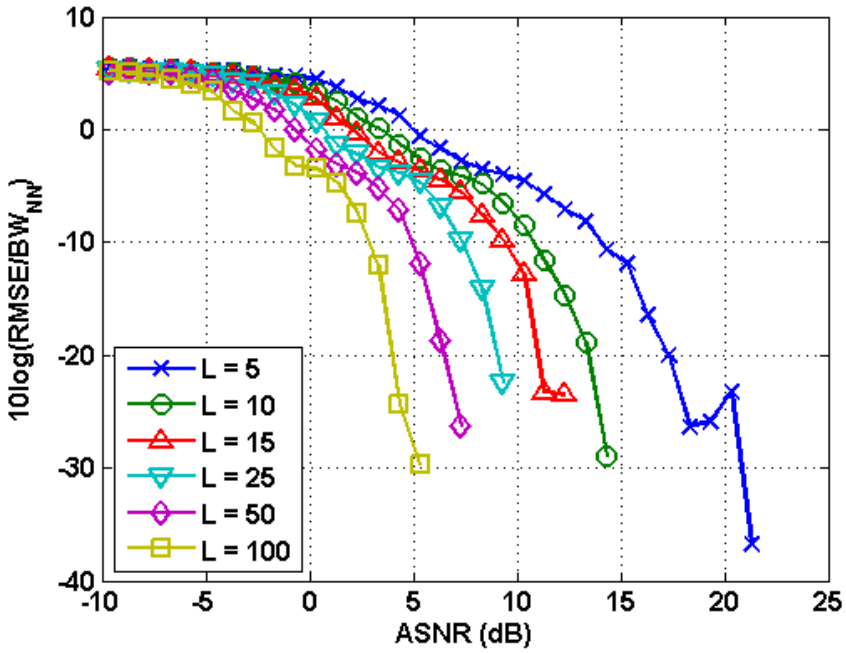

Figure 4.39: RMS error in MUSIC DoA estimates for two targets using the correct manifold, conformal array. $\times$: L=5, $\circ$: L=10, $\triangle$: L=15, $\triangledown$: L=25, $\diamond$: L=50, $\square$: L=100

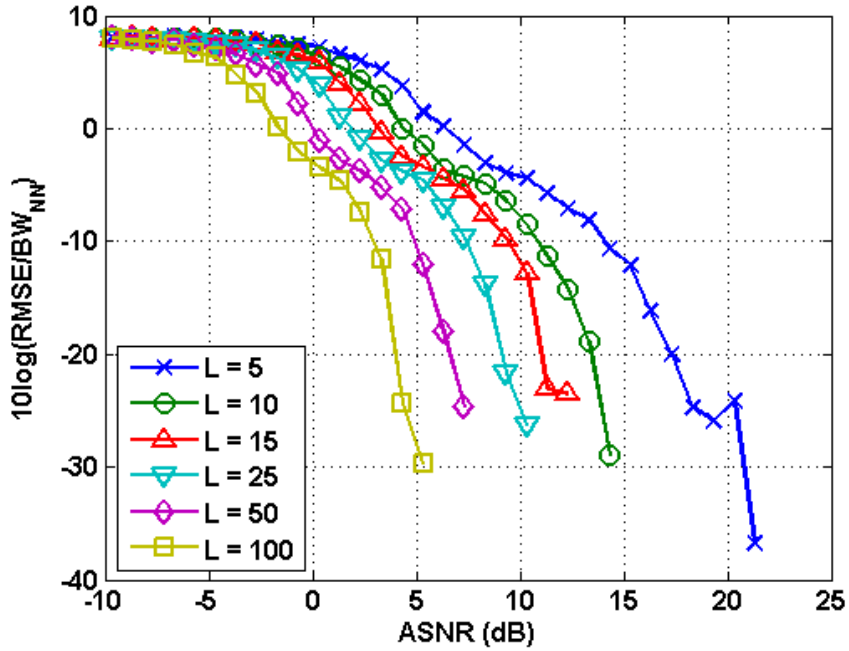

Figure 4.40: RMS error in MUSIC DoA estimates for two targets using the mismatched manifold, conformal array. $\times$: L=5, $\circ$: L=10, $\triangle$: L=15, $\triangledown$: L=25, $\diamond$: L=50, $\square$: L=100

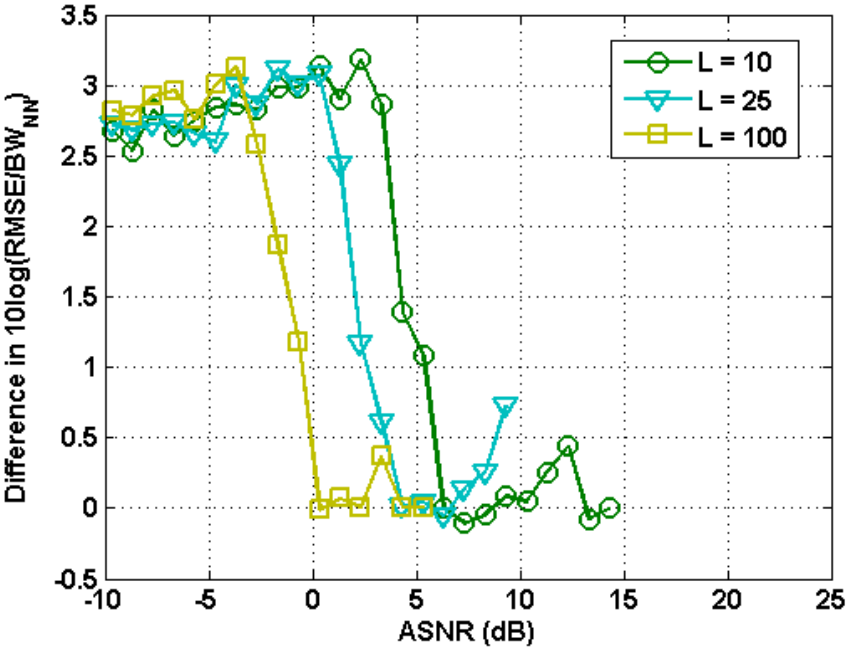

Figure 4.41: Difference in the RMS error of MUSIC DoA estimates for two targets using the correct and mismatched array manifold, conformal array. $\circ$: L=10, $\triangledown$: L=25, $\square$: L=100

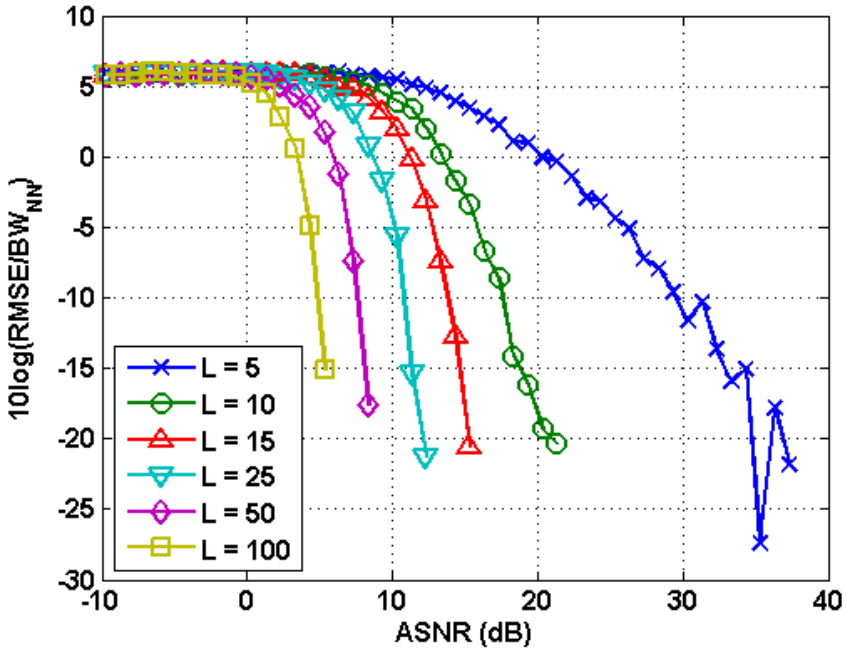

Figure 4.42: RMS error in MUSIC DoA estimates for four targets using the correct manifold, conformal array. × : L=5, ∘ : L=10, △ : L=15, ▽ : L=25, ⋄ : L=50, □ : L=100

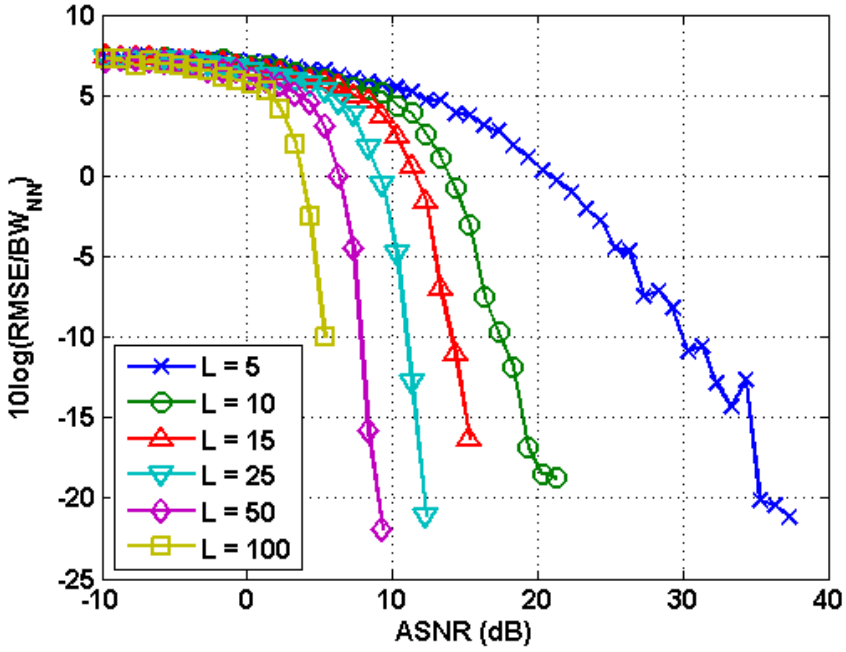

Figure 4.43: RMS error in MUSIC DoA estimates for four targets using the mismatched manifold, conformal array. × : L=5, ∘ : L=10, △ : L=15, ▽ : L=25, ⋄ : L=50, □ : L=100

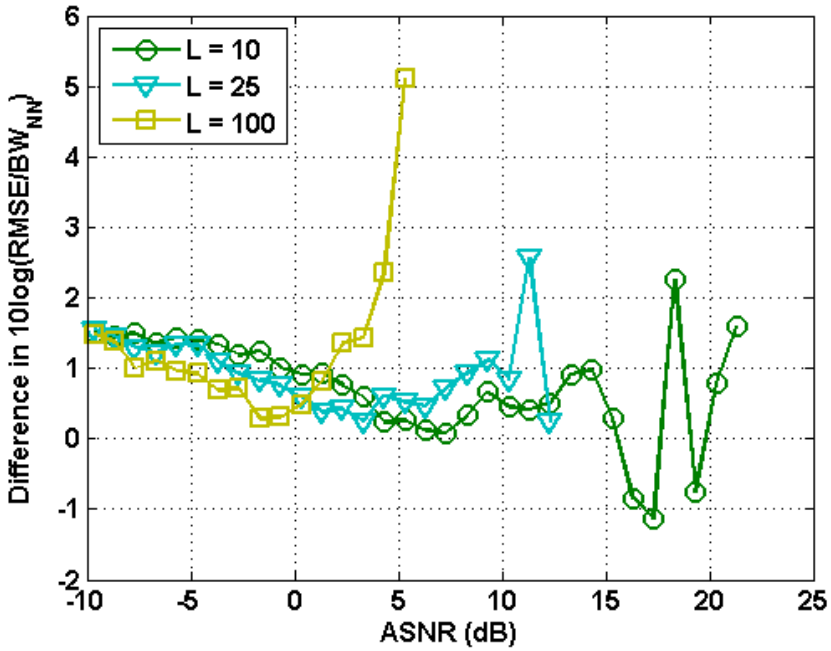

Figure 4.44: Difference in the RMS error of MUSIC DoA estimates for four targets using the correct and mismatched array manifold, conformal array. $\circ$: L=10, $\triangledown$: L=25, $\square$: L=100

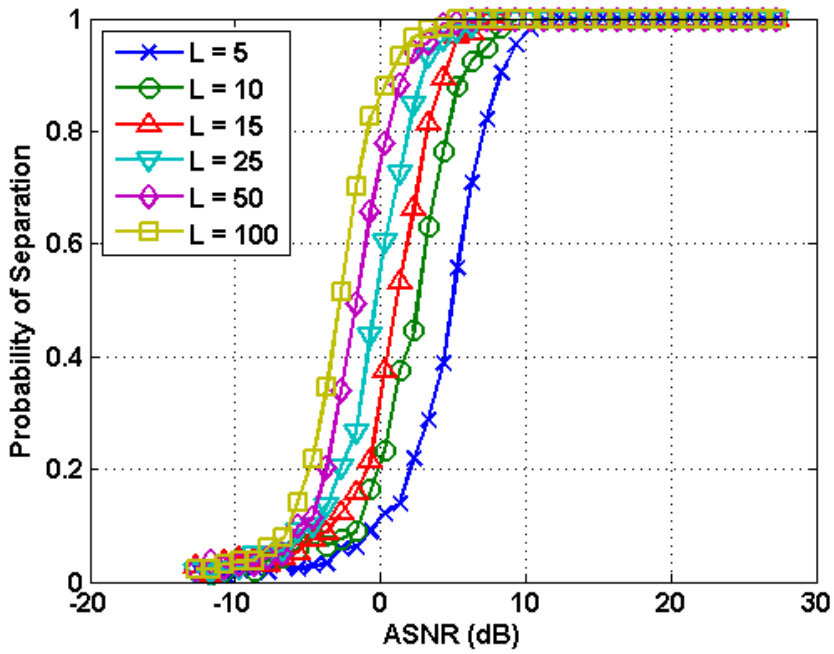

Figure 4.45: Probability of RISR separating two targets separated by half the nominal resolution using the correct manifold, conformal array. $\times$: L=5, $\circ$: L=10, $\triangle$: L=15, $\triangledown$: L=25, $\diamond$: L=50, $\square$: L=100

4.3.2.2 RISR

The RISR algorithm was again configured for 10 iterations, with a noise loading factor of $\alpha = 1/8$. The probability of separating targets is plotted in Figures 4.45 and 4.46 for the matched manifold and mismatched array manifold cases respectively. Similar to the ULA geometry the difference between the two models is very small for RISR and some representative cases are plotted in Figure 4.47.

Figures 4.48 and 4.49 plot the RMS error in RISR's DoA estimates for two closely spaced targets using the matched and mismatched array manifolds, while Figure 4.50 plots the difference in error for the two manifolds.

Finally, Figures 4.51 and 4.52 depict the RISR RMS error for four targets. The difference in RMS error between the matched and mismatched manifold cases can be seen in Figure 4.53.

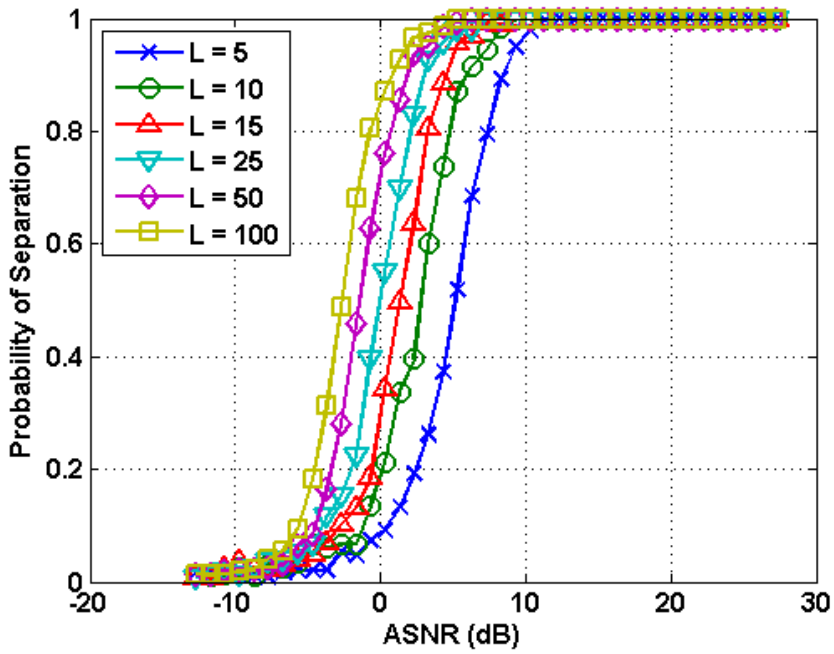

Figure 4.46: Probability of RISR separating two targets separated by half the nominal resolution using the mismatched manifold, conformal array. $\times$: L=5, $\circ$: L=10, $\triangle$: L=15, $\triangledown$: L=25, $\diamond$: L=50, $\square$: L=100

4.4 Discussion

The impact of substituting the transmit array manifold for the receive manifold on direction of arrival estimation algorithms is highly dependent upon the algorithm itself, and the manner in which the algorithm uses the array manifold. In examining the performance impact on MUSIC and RISR it was found that MUSIC suffers a loss of performance while RISR does not. This is attributable to the RISRs use of a model mismatch loading term. In the following discussion we will examine in detail the performance impact of transmit-for-receive manifold mismatch.

4.4.1 MUSIC

The MUSIC algorithm explicitly depends on the accuracy of the assumed array manifold and it is not surprising that performance suffers if the assumed array manifold does not match

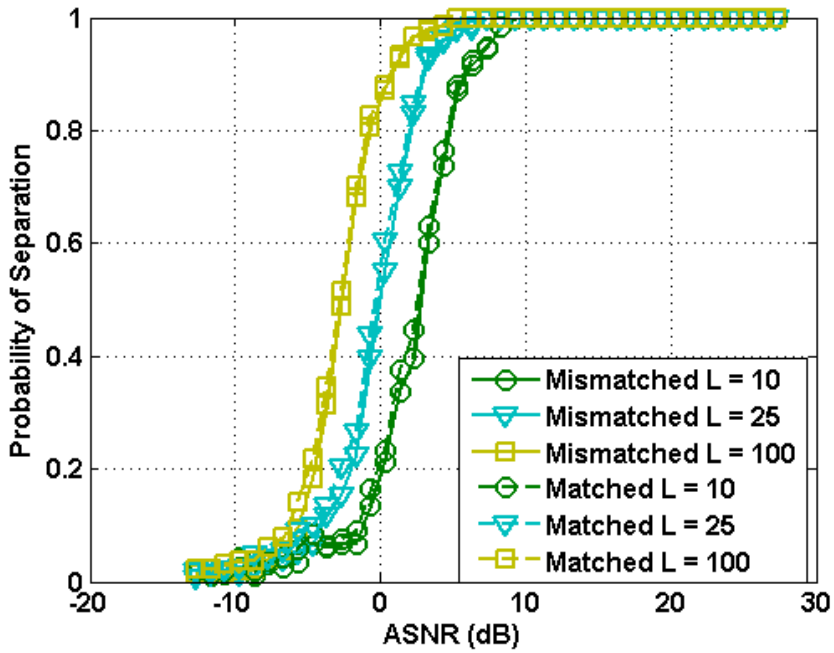

Figure 4.47: Comparison of the probability of RISR separating two targets separated by half the nominal resolution using the correct and mismatched array manifold, conformal array. Dashed lines : correct manifold, Solid lines : mismatched manifolds. $\circ$: L=10, $\triangledown$: L=25, $\square$: L=100

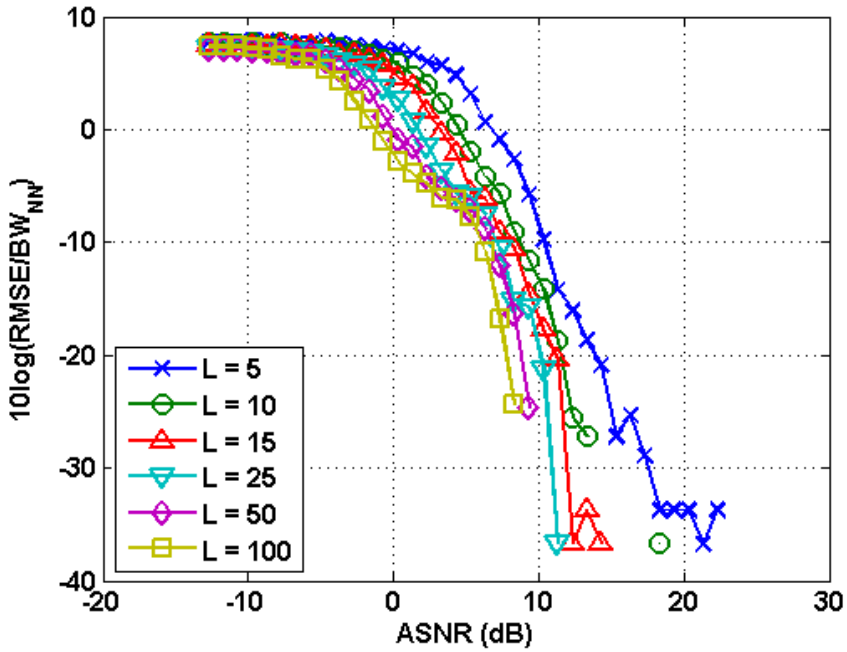

Figure 4.48: RMS error in RISR DoA estimates for two targets using the correct manifold, conformal array. $\times$: L=5, $\circ$: L=10, $\triangle$: L=15, $\triangledown$: L=25, $\diamond$: L=50, $\square$: L=100

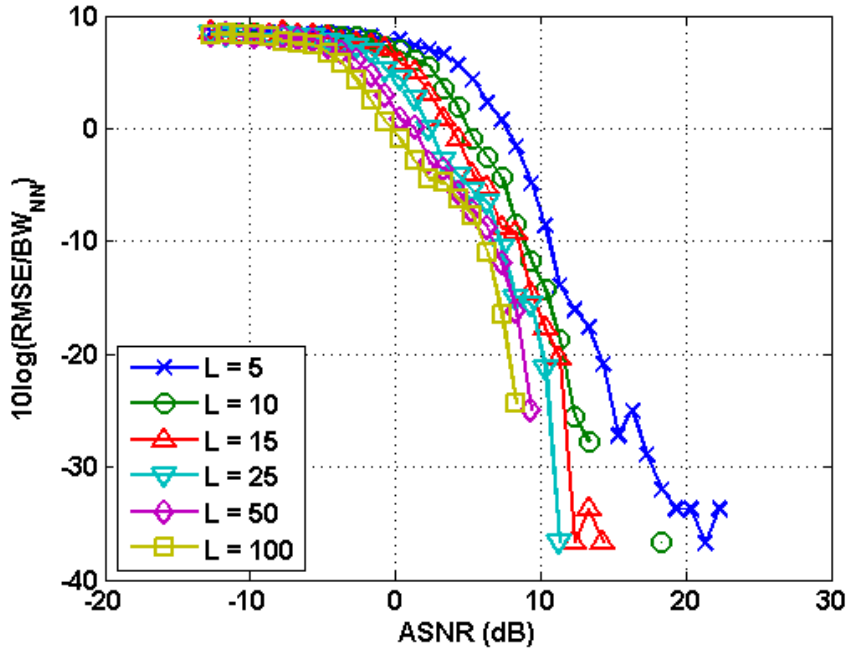

Figure 4.49: RMS error in RISR DoA estimates for two targets using the mismatched manifold, conformal array. × : L=5, ∘ : L=10, △ : L=15, ▽ : L=25, ⋄ : L=50, □ : L=100

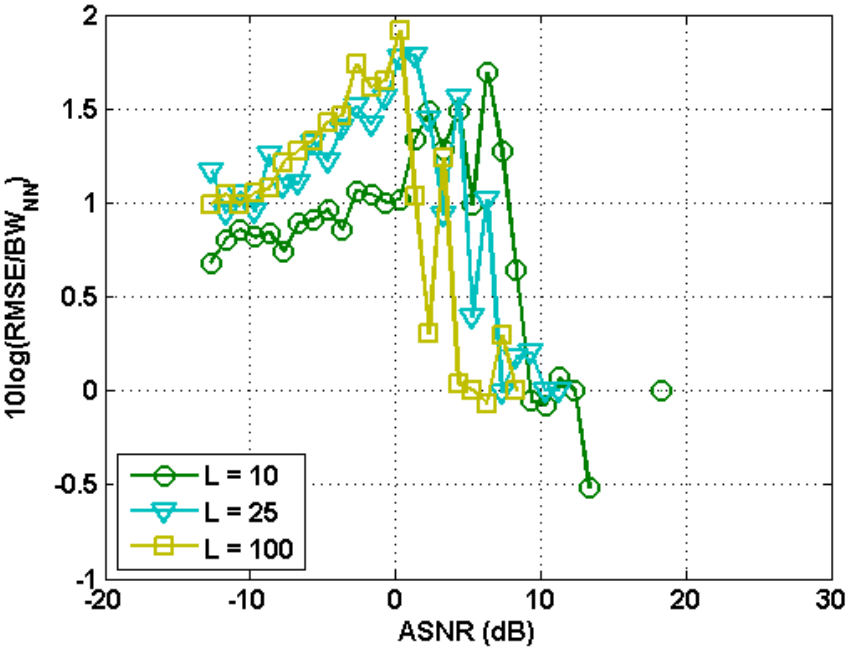

Figure 4.50: Difference in the RMS error of RISR DoA estimates for two targets using the correct and mismatched array manifold, conformal array. ∘ : L=10, ▽ : L=25, □ : L=100

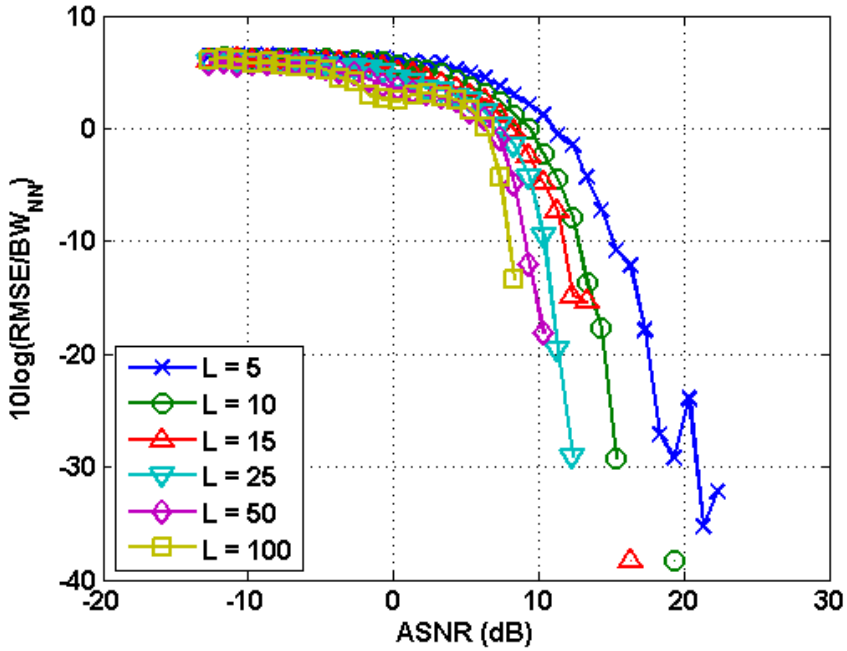

Figure 4.51: RMS error in RISR DoA estimates for four targets using the correct manifold, conformal array. $\times$: L=5, $\circ$: L=10, $\triangle$: L=15, $\triangledown$: L=25, $\diamond$: L=50, $\square$: L=100

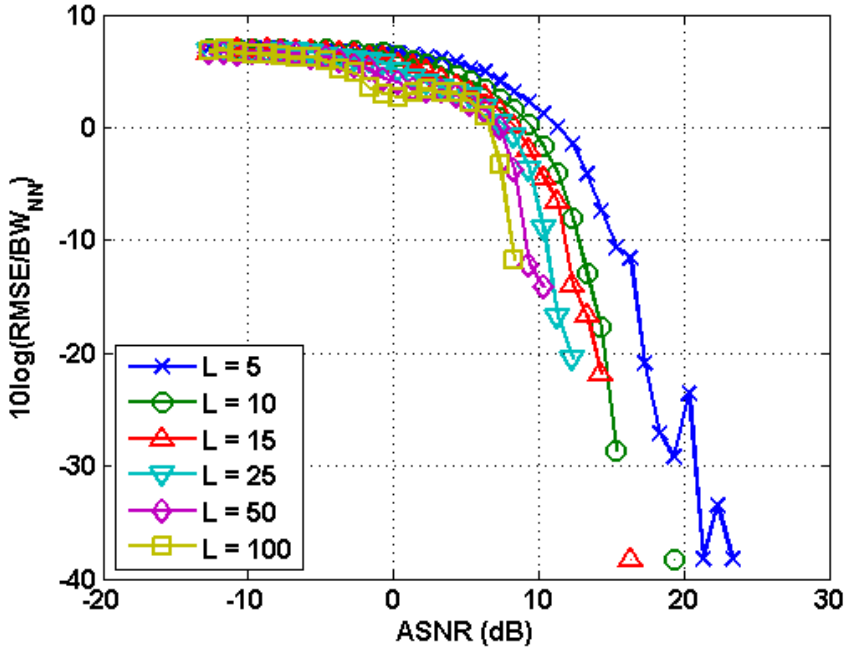

Figure 4.52: RMS error in RISR DoA estimates for four targets using the mismatched manifold, conformal array. $\times$: L=5, $\circ$: L=10, $\triangle$: L=15, $\triangledown$: L=25, $\diamond$: L=50, $\square$: L=100

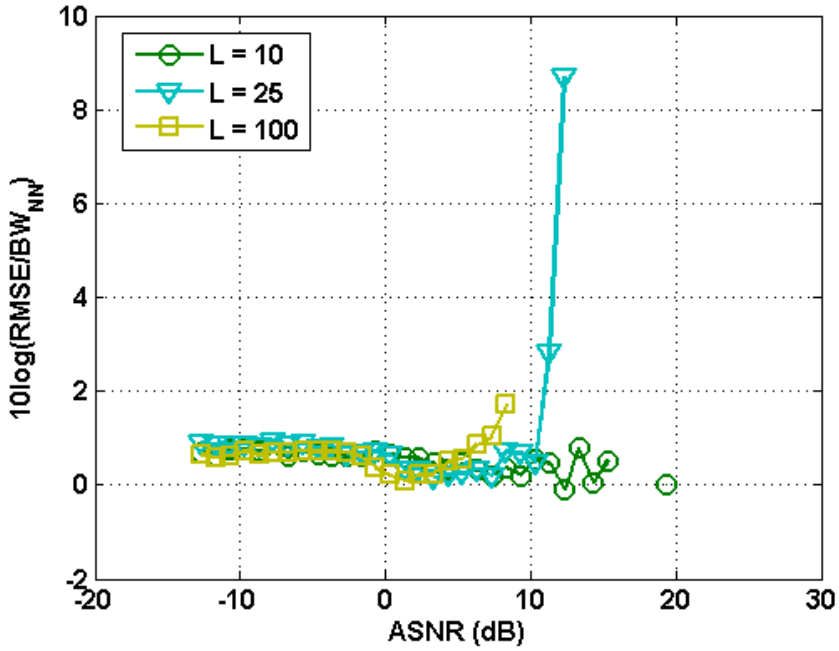

Figure 4.53: Difference in the RMS error of RISR DoA estimates for four targets using the correct and mismatched array manifold, conformal array. $\circ$: L=10, $\triangledown$: L=25, $\square$: L=100

the true array manifold. The impact of this model mismatch can be seen in both of the metrics. Figures 4.19 shows the probability of separation for MUSIC on the ULA for both the matched manifold and mismatched manifold, with time support $L = 10, 25$ and 100. In all three sample support curves there is a 3–4 dB performance penalty for substituting the transmit manifold for the receive manifold. Interestingly, this same penalty is not present in the conformal array geometry. This is likely due to the reduced mutual impedance between elements as the PEC tends to suppress mutual coupling. MUSIC's performance is also degraded in terms of the RMS error of the DoA estimation it produces. Both Figures 4.22 and 4.25 show a dramatic difference between the RMS error when using the correct receive manifold then when the mismatched transmit manifold is used. This difference is most dramatic at high ASNR, implying that extra signal power is needed to overcome the so called model noise. The difference is RMS error for the conformal array likewise shows a penalty for manifold substitution. In contrast the ULA geometry, Figures 4.41 and 4.44 show that the error in DoA estimates is principally located at lower ASNRs for the conformal

geometry. The difference is also smaller in keeping with the lower mutual coupling. Both metrics show MUSIC is susceptible to performance degradation if the transmit manifold is mistakingly substituted for the receive manifold.

4.4.2 RISR

RISR has built in model mismatch tolerance and this tolerance is readily apparent from the simulation results. In contrast to MUSIC which showed a performance penalty of 3–4 dB in the probability of separating two closely spaced targets, Figures 4.28 and 4.47 show virtually no difference between the mismatched and correct manifold. This difference in performance between MUSIC and RISR can be appreciated by examining the example spectrums in Figures 4.54 and 4.55. Both spectrums are taken from the transition region when each algorithm is resolving two closely spaced signals for roughly half the trials. In the MUSIC pseudo-spectrum there is a marked difference between the matched and mismatched manifolds, with the correct receive manifold showing a greater potential to separate the two targets. In comparison the RISR spectrum is nearly identical for both the manifolds implying that RISR will give similar performance in the face of some model mismatch.

RISR model mismatch tolerance can also be seen by examining the difference in DoA RMS error when using either the correct receive manifold or the mismatched transmit manifold. For the ULA geometry, Figures 4.31 and 4.34 show very little difference between the two models. Figures 4.50 and 4.53 tell as similar story for the conformal array with less then 1 dB difference for all but a small handful of data points.

4.5 Summary

In this chapter, we have seen how the imperfections in the matching networks of RF power and low noise amplifiers can propagate through the microwave front-end to load an antenna element. Moreover, it was noted that the non-reciprocal nature of a transmit-receive switch

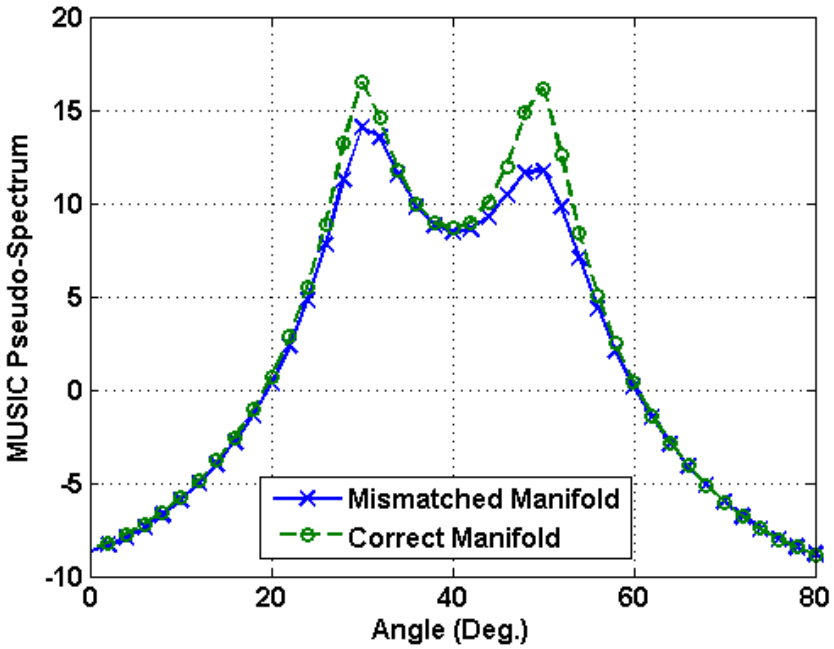

Figure 4.54: Example MUSIC pseudo-spectrum showing differences in estimates between the correct and mismatched manifold. Solid line with × markers : mismatched manifold, dashed line with ∘ markers : matched manifold

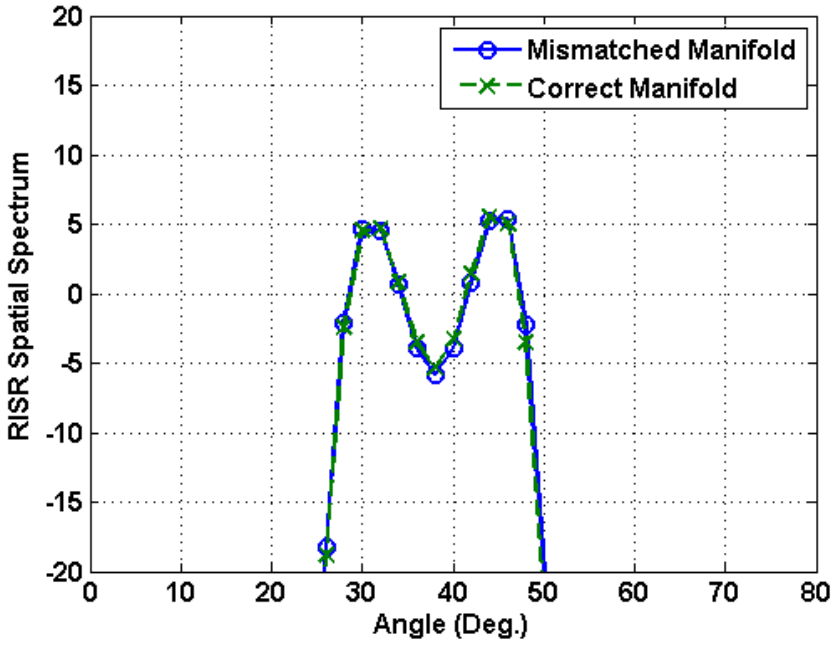

Figure 4.55: Example RISR spectrum showing virtually no difference in estimates between the correct and mismatched manifold. Solid line with × markers : mismatched manifold, dashed line with ∘ markers : matched manifold

will cause the load placed on the antenna to be dependent upon the switch state. This mode dependent load was then integrated into a mutual coupling model for an antenna array, and it was shown that the mutual coupling between array elements would change depending on the mode of the system. As the array manifold is influenced by the mutual coupling, this difference in the mutual coupling between elements will result in a different array manifold on transmit then on receive. It was then shown that substituting the transmit manifold for the receive manifold led to performance degradation for the MUSIC algorithm, but little to no performance degradation in RISR. It was surmised that RISR's model mismatch loading term gives the algorithm enough robustness to model mismatch that the transmit-for-receive manifold substitution did not affect the DoA estimates.

Chapter 5

Closure

5.1 Summary & Conclusions

Inaccuracies in the underlying array model can degrade the performance of modern array processing algorithms, but recognizing this mismatch provides an opportunity to recapture some of that lost performance. If we can have the introspection to appreciate the limits of our knowledge and the limits of the models we work with we can develop techniques to regain some of the performance lost to model mismatch. This work attempted to do just that, first by developing RACE, a blind calibration routine to help improve the array model used in the RISR DoA algorithm. RACE uniquely extend RISR's existing model mismatch capabilities while retaining RISR's SCM'less structure, making it relevant to low sample support environments. This work then examined a case of model mismatch perpetuated by applying an oversimplified model of microwave hardware. This oversimplification, masked the mode dependent antenna loading that can perturb the array's performance and the performance of many array processing algorithms. These cases of model mismatch cost performance but if we are willing to deal with the added complexity we can recapture much of that lost performance.

The RISR Array Calibration Enhancement (RACE) algorithm was developed as a blind

calibration routine that when paired with RISR can simultaneously estimate the channel gain/phase variations, mutual coupling and DoA of incident signals. While the RISR algorithm was designed with model mismatch in mind, the calibration enhancement presented herein takes the next logical step by using a more robust model of common array perturbations. By estimating these perturbations it is possible to recapture some of the accuracy lost to using a idealized array signal model. In Chapter 3 we developed the RACE algorithm by leveraging a more robust array signal model and perturbation estimation techniques developed in [20] and applied them to the RISR algorithm. We then showed the efficacy of the algorithm and explored its convergence region. It was found that RACE can improve the performance of RISR in the face of model mismatch. In addition, RACE is robust to a wide range of channel gain variation and to a somewhat smaller range of channel phase variation. It was also found that the effectiveness of RACE was dependent on both the number of sources and the SNR environment, with additional SNR required as the number of signals increased. A method to extend the convergence region of RACE by integrating prior calibration data was also developed. Subsequent testing showed the manifold replacement method could significantly extend the convergence region of the RACE algorithm. RACE is suitable for any array where RISR is used and can improve DoA accuracy by reducing model mismatch associated with channel gain/phase and mutual coupling. Since RISR is not dependent on a sample covariance matrix both RISR and RACE are prime choices when either sample support is low, or coherent sources are present.

Model mismatch can also occur when engineers incorrectly apply a transmitting array model to an array operating in a receive mode. This type of model mismatch was explored in Chapter 4 by showing that the front-end hardware can place a mode dependent load on the array elements. This load in turn affects the mutual coupling and the array manifold. This approach is unique in its consideration of RF hardware as convention simplifies this same hardware down to a Thévenin model which masks the underlying mode dependency. This type of model mismatch is also often overlooked in the face of the traditional antenna reci-

procity mantra. It was shown this transmit-for-receive array model substitution degraded the performance of the MUSIC algorithm, while RISR was more robust to the model mismatch. Conversely, this performance loss can be recaptured by addressing the model mismatch and using the correct manifold.

5.2 Future Work

The work contained herein is only the first step of developing the RACE algorithm and much is left to the future work of myself and others. There is considerable work left to be done on RACE's noise loading limits and profiles. The results presented in Chapter 3 counterintuitively showed two constant value loading profiles out-performing all three model noise loading profiles that gradually reduced over the calibration cycle. It was surmised that the limits on β contributed to the under performance of these loading profiles. Future work should include defining upper and lower bounds on β for optimal performance, as well as reexamining model noise loading profiles. Thus far RACE has been constrained to theoretical simulations and implementing RACE on actual hardware will provide rich opportunities for future work. The calibration estimations in RACE were implemented using a least squares framework, but in other frameworks may prove interesting, particularly recursive methods that may be able to run in parallel to RISR. Future work should also include exploring integrating prior calibration data via $\mathbf{\Gamma}$ and $\mathbf{C}$ seeding. This work proposed two methods to integrate prior calibration data, $\mathbf{\Gamma}$ and $\mathbf{C}$ seeding and manifold replacement, but only the performance of manifold replacement was explored. Future work into prior calibration should also extend to tracking calibration over a system's lifetime. One of the defining benefits to blind calibration is frequency periodic recalibration and it may prove interesting to see how the two methods adapt to an evolving array.

References

[1] H. L. V. Trees, *Optimum Array Processing*. New York: Wiley, 2002.

[2] Z. Huang, C. Balanis, and C. Birtcher, "Mutual coupling in beamforming with circular array," in *Antennas and Propagation Society International Symposium 2006, IEEE*, Albuquerque, NM, July 2006, pp. 4785–4788.

[3] C. Zhang, J. Ni, Y. Han, and G. Du, "Performance analysis of antenna array calibration and its impact on beamforming: A survey," in *Communications and Networking in China (CHINACOM), 2010 5th International ICST Conference on*, Beijing, China, Aug 2010, pp. 1–5.

[4] M. Ozdemir, H. Arslan, and E. Arvas, "A mutual coupling model for MIMO systems," in *Wireless Communication Technology, 2003. IEEE Topical Conference on*, Oct 2003, pp. 306–307.

[5] C. Schmid, S. Schuster, R. Feger, and A. Stelzer, "On the effects of calibration errors and mutual coupling on the beam pattern of an antenna array," *IEEE Trans. Antennas Propag.*, vol. 61, no. 8, pp. 4063–4072, Aug 2013.

[6] K. Lo and T. Vu, "Minimisation of mutual coupling effect on null steering by using guard elements," *Electronics Letters*, vol. 23, no. 16, pp. 854–855, July 1987.

[7] S. Henault and Y. Antar, "Comparison of various mutual coupling compensation methods in receiving antenna arrays," in *Antennas and Propagation Society International Symposium, 2009. APSURSI '09. IEEE*, Charleston, SC, June 2009, pp. 1–4.

[8] Y. Du, X. Xi, W. Xi, and L. Zhou, "The correction of mutual coupling and the amplitude and phase error based on digital beamforming receiving antenna," in *Antennas, Propagation EM Theory (ISAPE), 2012 10th International Symposium on*, Xian, China, Oct 2012, pp. 231–233.

[9] B. Liao and S.-C. Chan, "Adaptive beamforming for uniform linear arrays with unknown mutual coupling," *IEEE Microw. Wireless Compon. Lett.*, vol. 11, pp. 464–467, 2012.

[10] Z. Ye and C. Liu, "Non-sensitive adaptive beamforming against mutual coupling," *Signal Processing, IET*, vol. 3, no. 1, pp. 1–6, January 2009.

[11] P. Demarcke, H. Rogier, R. Goossens, and P. De Jaeger, "Beamforming in the presence of mutual coupling based on constrained particle swarm optimization," *IEEE Trans. Antennas Propag.*, vol. 57, no. 6, pp. 1655–1666, June 2009.

[12] S. Blunt, T. Chan, and K. Gerlach, "A new framework for direction-of-arrival estimation," in *Sensor Array and Multichannel Signal Processing Workshop, 2008. SAM 2008. 5th IEEE*, Darmstadt, Germany, July 2008, pp. 81–85.

[13] S. Blunt, T. Chan, and K. Gerlach, "Robust DOA estimation: The reiterative superresolution (RISR) algorithm," *IEEE Trans. Aerosp. Electron. Syst.*, vol. 47, no. 1, pp. 332–346, 2011.

[14] C. Seligson, "Comments on "high-resolution frequency-wavenumber spectrum analysis"," *Proceedings of the IEEE*, vol. 58, no. 6, pp. 947–949, June 1970.

[15] P. Stoica, Z. Wang, and J. Li, "Robust capon beamforming," *IEEE Signal Process. Lett.*, vol. 10, no. 6, pp. 172 –175, Jun. 2003.

[16] J. Li, P. Stoica, and Z. Wang, "On robust capon beamforming and diagonal loading," *IEEE Trans. Signal Process.*, vol. 51, no. 7, pp. 1702 – 1715, Jul. 2003.

[17] J. Li, P. Stoica, and Z. Wang, "Doubly constrained robust capon beamformer," *IEEE Trans. Signal Process.*, vol. 52, no. 9, pp. 2407 – 2423, Sep. 2004.

[18] Z. Liu, Z. Huang, and Y. Zhou, "Bias analysis of MUSIC in the presence of mutual coupling," *Signal Processing, IET*, vol. 3, no. 1, pp. 74–84, January 2009.

[19] Z. Ye and C. Liu, "On the resiliency of MUSIC direction finding against antenna sensor coupling," *IEEE Trans. Antennas Propag.*, vol. 56, no. 2, pp. 371–380, Feb 2008.

[20] B. Friedlander and A. Weiss, "Direction finding in the presence of mutual coupling," *IEEE Trans. Antennas Propag.*, vol. 39, no. 3, pp. 273–284, 1991.

[21] Y. Yu, H.-S. Lui, C. H. Niow, and H. T. Hui, "Improved DOA estimations using the receiving mutual impedances for mutual coupling compensation: An experimental study," *IEEE Trans. Wireless Commun.*, vol. 10, no. 7, pp. 2228–2233, July 2011.

[22] S. Lundgren, "A study of mutual coupling effects on the direction finding performance of ESPRIT with a linear microstrip patch array using the method of moments," in *Antennas and Propagation Society International Symposium, 1996. AP-S. Digest*, vol. 2, Baltimore, MD, July 1996, pp. 1372–1375 vol.2.

[23] T. Zhang and H. Hui, "Direction of arrival estimation using ESPRIT with mutual coupling compensation," *Science, Measurement and Technology, IEE Proceedings* -, vol. 151, no. 6, pp. 476–478, Nov 2004.

[24] T. T. Zhang, H. T. Hui, and Y. Lu, "Compensation for the mutual coupling effect in the ESPRIT direction finding algorithm by using a more effective method," *IEEE Trans. Antennas Propag.*, vol. 53, no. 4, pp. 1552–1555, April 2005.

[25] R. Monzingo, T. Miller, and R. L. Haupt, *Introduction to Adaptive Arrays*, 2nd ed. Scitech, 2011.

[26] K. Van't Klooster, "Radiation characteristics of a SAR antenna panel of ERS-1 determined from planar near-field measurements," in *Microwave Conference, 1987. 17th European*, Rome, Italy, Sept 1987, pp. 503–508.

[27] C. Bowman, A. Bogorad, G. Brucker, S. Seehra, and T. Lloyd, "ITO-coated RE transparent materials for antenna sunshields-space environment effects," *IEEE Trans. Nucl. Sci.*, vol. 37, no. 6, pp. 2134–2137, Dec 1990.

[28] B. Ng, M. H. Er, and C. Kot, "Array gain/phase calibration techniques for adaptive beamforming and direction finding," *Radar, Sonar and Navigation, IEE Proceedings*, vol. 141, no. 1, pp. 25–29, Feb 1994.

[29] M. Viberg and A. Swindlehurst, "A bayesian approach to auto-calibration for parametric array signal processing," *IEEE Trans. Signal Process.*, vol. 42, no. 12, pp. 3495–3507, Dec 1994.

[30] F. Sellone and A. Serra, "A novel online mutual coupling compensation algorithm for uniform and linear arrays," *IEEE Trans. Signal Process.*, vol. 55, no. 2, pp. 560 –573, Feb. 2007.

[31] I. Solomon, D. Gray, Y. Abramovich, and S. Anderson, "Estimation of array mutual coupling and sensor positions for over-the-horizon radar," in *Proc. of IEEE TENCON. Digital Signal Processing Applications*, vol. 2, Perth, WA, Nov. 1996, pp. 846 –851.

[32] B. P. Ng, J. P. Lie, M.-H. Er, and A. Feng, "A practical simple geometry and gain/phase calibration technique for antenna array processing," *IEEE Trans. Antennas Propag.*, vol. 57, no. 7, pp. 1963–1972, July 2009.

[33] A. Jaffer, "Sparse mutual coupling matrix and sensor gain/phase estimation for array auto-calibration," in *Radar Conference, 2002. Proceedings of the IEEE*, Long Beach, CA, 2002, pp. 294–297.

[34] H. Mir, J. Sahr, G. Hatke, and C. Keller, "Self-calibration of an airborne array," in *Signals, Systems and Computers, 2004. Conference Record of the Thirty-Eighth Asilomar Conference on*, vol. 2, Nov 2004, pp. 2340–2344 Vol.2.

[35] J. Capon, "High-resolution frequency-wavenumber spectrum analysis," *Proceedings of the IEEE*, vol. 57, no. 8, pp. 1408–1418, Aug 1969.

[36] R. Sanudin, N. Noordin, A. El-Rayis, N. Haridas, A. Erdogan, and T. Arslan, "Capon-like DOA estimation algorithm for directional antenna arrays," in *Antennas and Propagation Conference (LAPC), 2011 Loughborough*, Loughborough, UK, Nov 2011, pp. 1–4.

[37] M. Hirakawa, H. Tsuji, and A. Sano, "Computationally efficient DOA estimation based on linear prediction with capon method," in *Acoustics, Speech, and Signal Processing, 2001. Proceedings. (ICASSP '01). 2001 IEEE International Conference on*, vol. 5, Salt Lake City, UT, 2001, pp. 3009–3012 vol.5.

[38] S. Schmidt, "Multiple emitter location and signal parameter estimation," Ph.D. dissertation, Stanford University, Stanford, California, 1979.

[39] R. Roy, "ESPRIT: Estimation of signal parameters via rotational invariance techniques," Ph.D. dissertation, Stanford University, Stanford, California, 1987.

[40] R. Weber and Y. Huang, "Analysis for capon and MUSIC DOA estimation algorithms," in *Antennas and Propagation Society International Symposium, 2009. APSURSI '09. IEEE*, Charleston, SC, June 2009, pp. 1–4.

[41] T. Dhope and D. Simunic, "On the performance of AoA estimation algorithms in cognitive radio networks," in *Communication, Information Computing Technology (ICCICT), 2012 International Conference on*, Mumbai, India, Oct 2012, pp. 1–5.

[42] R. Chen and T. Higgins, "Golay waveforms and adaptive estimation," in *Waveform Diversity and Design Conference (WDD), 2010 International*, Niagara Falls, ON, Aug 2010, pp. 257–261.

[43] T. Takahashi, H. Miyashita, Y. Konishi, and S. Makino, "Theoretical study on measurement accuracy of rotating element electric field vector (REV) method," *Electronics and Communications in Japan (Part I: Communications)*, vol. 89, no. 1, p. 22–33, 2006.

[44] R. Sorace, "Phased array calibration," *IEEE Trans. Antennas Propag.*, vol. 49, no. 4, pp. 517 –525, Apr. 2001.

[45] K. Lee, R. Chu, and S. Liu, "A built-in performance monitoring/fault isolation and correction (PM/FIC) system for active phased array antennas," in *Antennas and Propagation Society International Symposium, 1993. AP-S. Digest*, Jul. 1993, pp. 206 –209.

[46] W. Keizer, "Fast and accurate array calibration using a synthetic array approach," *IEEE Trans. Antennas Propag.*, vol. 59, no. 11, pp. 4115–4122, Nov. 2011.

[47] T. Takahashi, Y. Konishi, S. Makino, H. Ohmine, and H. Nakaguro, "Fast measurement technique for phased array calibration," *IEEE Trans. Antennas Propag.*, vol. 56, no. 7, pp. 1888 –1899, Jul. 2008.

[48] G. Hampson and A. Smolders, "A fast and accurate scheme for calibration of active phased-array antennas," in *Proc. of IEEE Antennas and Propagation Society International Symposium*, vol. 2, Orlando, FL, Jul. 1999, pp. 1040 –1043.

[49] C. Dorny, "A self-survey technique for self-cohering of antenna systems," *IEEE Trans. Antennas Propag.*, vol. 26, no. 6, pp. 877 – 881, Nov. 1978.

[50] G. Efstathopoulos and A. Manikas, "A blind array calibration algorithm using a moving source," in *Proc. of IEEE Sensor Array and Multichannel Signal Processing Workshop*, Darmstadt, Germany, Jul. 2008, pp. 455 –458.

[51] C. See, "Method for array calibration in high-resolution sensor array processing," *Radar, Sonar and Navigation, IEE Proceedings*, vol. 142, no. 3, pp. 90 –96, Jun. 1995.

[52] Y. Rockah and P. Schultheiss, "Array shape calibration using sources in unknown locations – Part II: near-field sources and estimator implementation," *IEEE Trans. Acoust., Speech, Signal Process.*, vol. 35, no. 6, pp. 724 – 735, Jun. 1987.

[53] H. Van Trees and K. Bell, "Array shape calibration using sources in unknown locations – Part I: Far-field sources," *IEEE Trans. Acoust., Speech, Signal Process.*, vol. 35, no. 3, pp. 286 – 299, Mar. 1987.

[54] F. Belfiori, S. Monni, W. Van Rossum, and P. Hoogeboom, "Mutual coupling compensation applied to a uniform circular array," in *Proc. of International Radar Symposium (IRS)*, Vilnius, Lithuania, Jun. 2010, pp. 100 –104.

[55] M. C. Dogan and J. M. Mendel, "Joint array calibration and direction-finding with virtual-ESPRIT algorithm," in *, IEEE Signal Processing Workshop on Higher-Order Statistics, 1993*, 1993, pp. 146 –150.

[56] H.-B. Li, Y.-D. Guo, J. Gong, and J. Jiang, "Mutual coupling self-calibration algorithm for uniform linear array based on ESPRIT," in *2012 2nd International Conference on Consumer Electronics, Communications and Networks (CECNet)*, Apr. 2012, pp. 3323 –3326.

[57] A. Lundgren, M. Lanne, and M. Viberg, "Two-step ESPRIT with compensation for modelling errors using a sparse calibration grid," in *IEEE International Conference on Acoustics, Speech and Signal Processing, 2007. ICASSP 2007*, vol. 2, Apr. 2007, pp. 1045 – 1048.

[58] S. Blunt, T. Chan, and K. Gerlach, "Robust DOA estimation: The reiterative superresolution (RISR) algorithm," *IEEE Trans. Aerosp. Electron. Syst.*, vol. 47, no. 1, pp. 332–346, 2011.

[59] C. Balanis, *Antenna Theory: Analysis and Design*, 3rd ed. Wiley, 2005.

[60] W. Stutzman and G. Thiele, *Antenna Theory and Design*, 2nd ed., ser. Antenna Theory and Design. Wiley, 1998.

[61] S. Ramo, J. Whinnery, and T. Van Duzer, *Fields and Waves in Communication Electronics*, 3rd ed. Wiley, 1994.

[62] D. Pozar, *Microwave engineering*, 3rd ed. Wiley, 2005.

[63] A. Mirkamali, J. Nateghi, and L. Asl, "Evaluation of mutual coupling models for calibrating the antenna arrays for DoA estimation," in *Antennas and Propagation, 2009. EuCAP 2009. 3rd European Conference on*, Berlin, Germany, March 2009, pp. 1033–1036.

[64] I. Gupta and A. Ksienski, "Effect of mutual coupling on the performance of adaptive arrays," *IEEE Trans. Antennas Propag.*, vol. 31, no. 5, pp. 785–791, Sept. 1983.

[65] K.-C. Lee and T.-H. Chu, "A circuit model for mutual coupling analysis of a finite antenna array," *IEEE Trans. Electromagn. Compat.*, vol. 38, no. 3, pp. 483–489, Aug 1996.

[66] T. Sato and R. Kohno, "New calibration matrix calculation method for removing the effect of mutual coupling for uniform linear arrays," in *Vehicular Technology Conference, 2006. VTC 2006-Spring. IEEE 63rd*, vol. 6, May 2006, pp. 2686–2690.

[67] H. Hui, "Improved compensation for the mutual coupling effect in a dipole array for direction finding," *IEEE Trans. Antennas Propag.*, vol. 51, no. 9, pp. 2498–2503, Sept. 2003.

[68] T. Svantesson, "Modeling and estimation of mutual coupling in a uniform linear array of dipoles," in *Acoustics, Speech, and Signal Processing, 1999. Proceedings., 1999 IEEE International Conference on*, vol. 5, Phoenix, AZ, 1999, pp. 2961–2964 vol.5.

[69] F. Sellone and A. Serra, "A novel online mutual coupling compensation algorithm for uniform and linear arrays," *IEEE Trans. Signal Process.*, vol. 55, no. 2, pp. 560–573, Feb 2007.

[70] W. Bu-hong, W. Yong-liang, and C. Hui, "A robust DoA estimation algorithm for uniform linear array in the presence of mutual coupling," in *Antennas and Propagation Society International Symposium, 2003. IEEE*, vol. 3, June 2003, pp. 924–927 vol.3.

[71] J. Herper, A. Hessel, and B. Tomasic, "Element pattern of an axial dipole in a cylindrical phased array, part I: theory," *IEEE Trans. Antennas Propag.*, vol. 33, no. 3, pp. 259 – 272, Mar. 1985.

[72] J. Herper, A. Hessel, and B. Tomasic, "Element pattern of an axial dipole in a cylindrical phased array, part II: element design and experiments," *IEEE Trans. Antennas Propag.*, vol. 33, no. 3, pp. 273 – 278, Mar. 1985.

[73] K. Demarest, *Engineering Electromagnetics*. Prentice Hall Books, 1998.

[74] C. Balanis, *Advanced Engineering Electromagnetics*. Wiley, 1989.

Appendix A

Notaion

A.1 Acronyms

ASNR	Array Signal-to-Noise Ratio
dB	Decibel
DoA	Direction of Arrival
EMF	Electromotive Force
ESPRIT	Estimation of Signal Parameter Via Rotational Invariance Techniques
MUSIC	Multiple Signal Classification
MVDR	Minimum Variance Distortionless Response
PEC	Perfect Electric Conductor
RACE	RISR Array Calibration Enhancement
RF	Radio Frequency
RISR	Reiterative Super Resolution
RMS	Root Mean Squared
SCM	Sample Covariance Matrix
SNR	Signal-to-Noise Ratio
T-R Switch	Transmit-Receive Switch

A.2 Conventions

x	Scalar
$\mathbf{x}$	Vector
$\mathbf{X}$	Matrix
$\hat{x}$	Estimation of x
$E\{x\}$	Expectation of x
$\|x\|$	Magnitude of x
$\measuredangle x$	Angle of x
$\mathbf{x}^H$, $\mathbf{X}^H$	Conjugate transpose
$\mathbf{x}^T$, $\mathbf{X}^T$	Transpose
$\mathbf{x}^*$	conjugate of $\mathbf{x}$
$[\mathbf{X}]_{ij}$	ij element of $\mathbf{X}$
$\mathbf{I_{x \times x}}$	$x \times x$ Identity matrix
$\mathbf{0_{i \times j}}$	$i \times j$ Zero matrix
$\odot$	Hadamard product
$\bigtriangledown x$	Gradient
$\bigtriangledown \cdot \mathbf{x}$	Divergence
$\bigtriangledown \times \mathbf{x}$	Curl
$\bigtriangledown^2 x$	Laplacian

A.3 Symbols

$\mathbf{A}$	i) Ideal array manifold (2)
	ii) Auxiliary vector potential (4.1.3.2)
$\mathbf{a}(\psi)$	Ideal array steering vector
a	PEC cylinder radius
α	i) RISR noise loading factor (2.1.3)
	ii) Unit cell angular size (4.1.3.2)
α_n	nth channel gain value
$\mathbf{B_1}$	First mutual coupling transformation matrix
$\mathbf{B_2}$	Second mutual coupling transformation matrix
$\mathbf{B_3}$	Third mutual coupling transformation matrix
$\mathbf{B_4}$	Fourth mutual coupling transformation matrix
$\mathbf{b}$	Unit vector
b	Horizontal dipole separation
β	RISR model loading factor
$\mathbf{C}$	Mutual coupling matrix
$\mathbf{c}$	Mutual coupling terms vector
c	Speed of light in a vacuum
c_q	qth unknown coefficient
Ci	Cosine integral
$\mathbf{D}$	Calibration matrix
d	i) Array element separation (2.1.2)
	ii) Vertical dipole separation distance (4.1.3.2)
$\mathbf{\Delta}$	Sensor position uncertainty matrix
ϵ	Permittivity
ϵ_0	Permittivity of freespace

η_0	Freespace impedance
$\mathbf{E}_A$	E-field derived from auxiliary vector potential
E_g	Dipole gap E-field
$G(\cdot)$	Green's function
$g_{mn}(\rho)$	Radial component of the Green's function
$\mathbf{\Gamma}$	Channel gain/phase matrix
Γ_g	Generator voltage reflection coefficient
Γ_{in}	Input voltage reflection coefficient
Γ_{out}	Output voltage reflection coefficient
Γ_s	Source voltage reflection coefficient
Γ_L	Load voltage reflection coefficient
$\boldsymbol{\gamma}$	Channel gain/phase term vector
$\mathbf{H}_A$	H-filed derived from auxiliary vector potential
$H^{(1)}$	Hankel function of the first kind
$H^{(2)}$	Hankel function of the first kind
h	Dipole gap height
I_n	Total current at the terminals of the nth array element
I_s	Total current at the terminals of the source antenna
I_{1i}, I_{2i}	Input currents to ports 1 and 2
I_m	Maximum current
J_n	nth order Bessel function of the first kind
J_{MUSIC}	MUSIC cost function
J_{RISR}	RISR cost function
$\mathbf{J}_{s1}$, $\mathbf{J}_{s2}$	ESPRIT selection matrices
$\mathbf{k}$	Wavenumber vector
k_{z0}	Progressive phase delay between neighboring column elements
k_{zn}	Phase of the nth vertical element

$\mathbf{K}$	Dipole current distribution
L	Number of time snapshots
l	Dipole length
λ	Wavelength
λ_i	Signal subspace eigenvalue
M	Number of samples in the array manifold
μ	Permeability
μ_0	Permeability of freespace
N	Number of elements in an array
N_s	Number of elements in a subarray
ν	Angular phase progression between cylindrical elements
ν_m	Phase of the mth angular element
$\mathbf{P}$	RISR spectral power distribution matrix
$\mathbf{p}_n$	Position vector for sensor element n
$\mathbf{p_h p_w}$	Pulse functions with a unity value over dipole gap
ρ_0	Radius of dipole array
ψ	Signal angle of incidence
$\mathbf{\Psi}$	Phase relationship matrix between subarray signal subspace eigenvectors
Ψ_q	qth orthogonal basis function
$\mathbf{\Phi}$	Phase relationship matrix between subarray manifolds
$\Phi_{mn}(\phi, z)$	ϕ and z components of the Green's function
Q	i) Number of incident signals (2)
	ii) Number of Galerkin basis functions (4.1.3.2)
$Q_1[\mathbf{z}]$	Gain/phase transformation function
$Q_2[\mathbf{z}]$	ULA mutual coupling transformation function
$Q_3[\mathbf{z}]$	UCA mutual coupling transformation function
$\mathbf{R}$	Covariance matrix

R	Radius of uniform circular array
R_1	Distance from top of dipole to target
R_2	Distance from bottom of dipole to target
r	Distance from center of dipole to target
R_{21}	Real part of the mutual impedance
$\mathbf{R_x}$	$\mathbf{x}$ covariance matrix
$\mathbf{R_v}$	$\mathbf{v}$ covariance matrix
$\mathbf{R_y}$	$\mathbf{y}$ covariance matrix
$\mathbf{R}_z$	RISR model noise covariance matrix
$\mathbf{S}$	True array manifold
$\mathbf{S}_{s1}$	First subarray manifold
$\mathbf{S}_{s2}$	Second subarray manifold
$\mathbf{s}(\psi)$	True array steering vector
s	Hight of dipole above PEC cylinder
Si	Sine integral
S_{11}, S_{22}	S-parameter reflection coefficients
S_{21}, S_{12}	S-parameter transmission coefficients
η_0	Freespace impedance
σ_s^2	Signal variance
σ_n^2	Noise variance
σ_i^2	Noise subspace eigenvalue
τ_{nk}	Time delay between source k and sensor n
τ_n	Time delay between origin and sensor n
$\mathbf{u}_i$	Eigenvector
$\mathbf{U}_s$	Set of signal subspace eigenvectors
$\mathbf{U}_{s1}$	First subarray eigenvectors
$\mathbf{U}_{s2}$	Second subarray eigenvectors

$\mathbf{U}_n$	Set of noise subspace eigenvectors
u_0	Dipole mutual impedance argument
u_1	Dipole mutual impedance argument
u_2	Dipole mutual impedance argument
$\mathbf{v}$	Noise vector
V_n	Total voltage at the terminals of the nth array element
V_{gn}	Voltage of the nth generator
V_g	Dipole gap voltage
V_{inc}	Incident voltage
ω	Radial frequency
w	Dipole width
$\mathbf{W}$	RISR adaptive filter bank
$\mathbf{X}$	Signal spatial distribution matrix
$\mathbf{x}$	Signal spatial distribution vector
X_{21}	Imaginary part of the mutual impedance
$\mathbf{Y}$	Array signal matrix
$\mathbf{y}$	Array signal vector
Z_{11}, Z_{22}	Self-Impedance
Z_{21}, Z_{12}	Mutual-Impedance
Z_L	Load impedance
Z_s	Source impedance
Z_0	Transmission line characteristic impedance
Z_{1d}	Drive point impedance
Z_{in}	Input impedance
Z_{out}	Output impedance
ζ_n	nth channel phase